Progress in Materials Science Vol. 28, pp. 1 to 96, 1983

0079-6425/83 $0.00 + .50

53

DYNAMIC FRACTURE (SPALLING) OF METALS

Marc André Meyers and Catherine Taylor Aimone

Center for Explosives Technology Research,
New Mexico Institute of Mining and Technology,
Socorro, New Mexico 87801, U.S.A.

(*Received 19 April 1983*)

SUMMARY

The fundamental mechanical aspects of dynamic fracture in metals are presented, with emphasis on spalling produced by the interactions of shock and reflected tensile waves. The major research efforts conducted in this area are reviewed; the process has been successfully described as a sequence of nucleation—growth—coalescence of voids or cracks. Quantitative models predicting the extent of damage have been successfully compared with experimental observations, by incorporating them into computer codes.

A number of metallurgical aspects of importance are discussed: failure initiation sites, crack propagation paths, strain-rate-dependent ductile to brittle transition, grain size effect, intergranular versus transgranular spalling. Of particular importance in iron and steels is the change in spall morphology when the 13 GPa stress is exceeded. This change is documented and interpreted in terms of the α(BCC) $\rightarrow$ ϵ(HCP) phase transformation undergone at that pressure. Micromechanical models describing the growth of voids in terms of dislocation motion are discussed.

Areas requiring additional research effort are identified.

CONTENTS

LIST OF SYMBOLS

A	Area per fragment
a	Crack length
B	Damping constant
b	Burgers vector
C	Velocity of sound
C_0	Velocity of sound at zero pressure
C_1	Longitudinal wave velocity
C_2	Shear wave velocity
C_R	Maximum crack velocity
D	Damage parameter
d	Fragment diameter
E	Energy
E_d	Plastic deformation energy
E_e	Elastic energy
E_s	Surface energy
E_T	Thermal energy
G_1	Crack energy release rate at wave velocity C_1
G_1^*	Crack energy release rate at rest
K	Stress intensity factor
K_B	Critical stress intensity factor for branching
K_C	Fracture toughness
K_{eff}	Effective stress intensity factor
K_{IC}	Plane strain fracture toughness
L	Length of dislocation segment
l	Void edge length
$\dot{l}$	Rate of cube side change in length
$\dot{N}$	Nucleation rate; rate of nucleation annihilation
$\dot{N}_0$	Threshold nucleation rate
$N(R)$	Number of voids per unit volume of radius R
P	Pressure
q	Artificial viscosity
R	Radius of crack or void
$\dot{R}$	Rate of radius increase
R_0	Smallest visible void radius
r_c	Critical crack radius
r_y	Plastic zone radius
S_1, S_2	Parameters relating shock and particle velocity
T	Temperature
t	Time
t_0	Void nucleation time
Δt	Incremental time
U_s	Shock velocity
u_p	Particle velocity
V	Volume
$\dot{V}$	Rate of void volume change
V_v	Relative void volume
V_0	Void volume at nucleation
v_L	Longitudinal wave velocity
v_R	Radial velocity
v_r	Outward ring velocity
v_s	Shear wave velocity
x_1	Distance

Δx	Incremental distance
γ	Surface energy
δ	Spall thickness
$\dot{\epsilon}$	Strain rate
$\dot{\epsilon}_{\theta\theta}$	Hoop strain rate
ϵ_i^p	Plastic strain tensor
$\dot{\epsilon}_i^p$	Plastic strain rate
η	Viscosity
λ	Lamé constant
μ	Shear modulus (Lamé constant)
ρ	Density
ρ_0	Initial density
$\dot{\rho}$	Rate of change of density
σ	Tensile stress
σ_c	Critical tensile stress required to produce spall
σ_{go}	Threshold stress for growth
σ_m	Hydrostatic stress
$\dot{\sigma}_m$	Mean stress rate
σ_{no}	Tensile threshold stress
σ_0	Peak tensile stress
σ_y	Normal tensile stress
σ_{ys}	Yield stress
σ_1	Stress sensitivity for nucleation
τ	Shear stress
τ_0	Frictional stress
ν	Poissons ratio

1. Introduction

Spalling is a material failure produced by the action of tensile stresses developed in the interior of a body when two decompression waves collide.[1]

The effects associated with the impact of a projectile against a target, detonation of a high explosive in direct contact with it, or sudden deposition of intense pulses of energy on the target can be systematically studied as a logical sequence of events. Figure 1 shows the four principal phenomena involved in the impact of a spherical projectile against a target. This is a good example of a dynamic deformation system. At the impact surface, one has dynamic deformation of the material, with the formation of a crater. The flow stress of many metals is strongly dependent on the strain rate, and this has a bearing on the development of the deformation region. As the strain rate increases, the ability of the heat generated to be transferred to the surroundings is decreased; this leads to temperature increases in the regions with attendant flow stress decreases. These, in turn, lead to a localization of the deformation (of shear character). Intense shear localization regions may be formed (with strains of up to 100[2] across the bands); these bands are commonly known as adiabatic shear bands.[3] Figure 1 shows an optical micrograph of such a band. They are classified into transformation bands and deformation bands.[3] They play a very important role in the fracturing process, in steels. The fractures tend to follow these bands (when they are of the transformation type) and their frequency determines, as a result, the sizes of the fragments formed. The origin of the transformation bands is not very well understood yet. Different investigators report different structures, and it is not known whether melting or just the $(\alpha \rightarrow \gamma)$ phase transformation is required for their formation in steels. The third phenomenon of importance is the propagation of the shock wave induced by the impact of the projectile through the target. The shock-wave amplitude, which depends upon the projectile velocity, produces significant substructural changes in the target. These substructural changes have

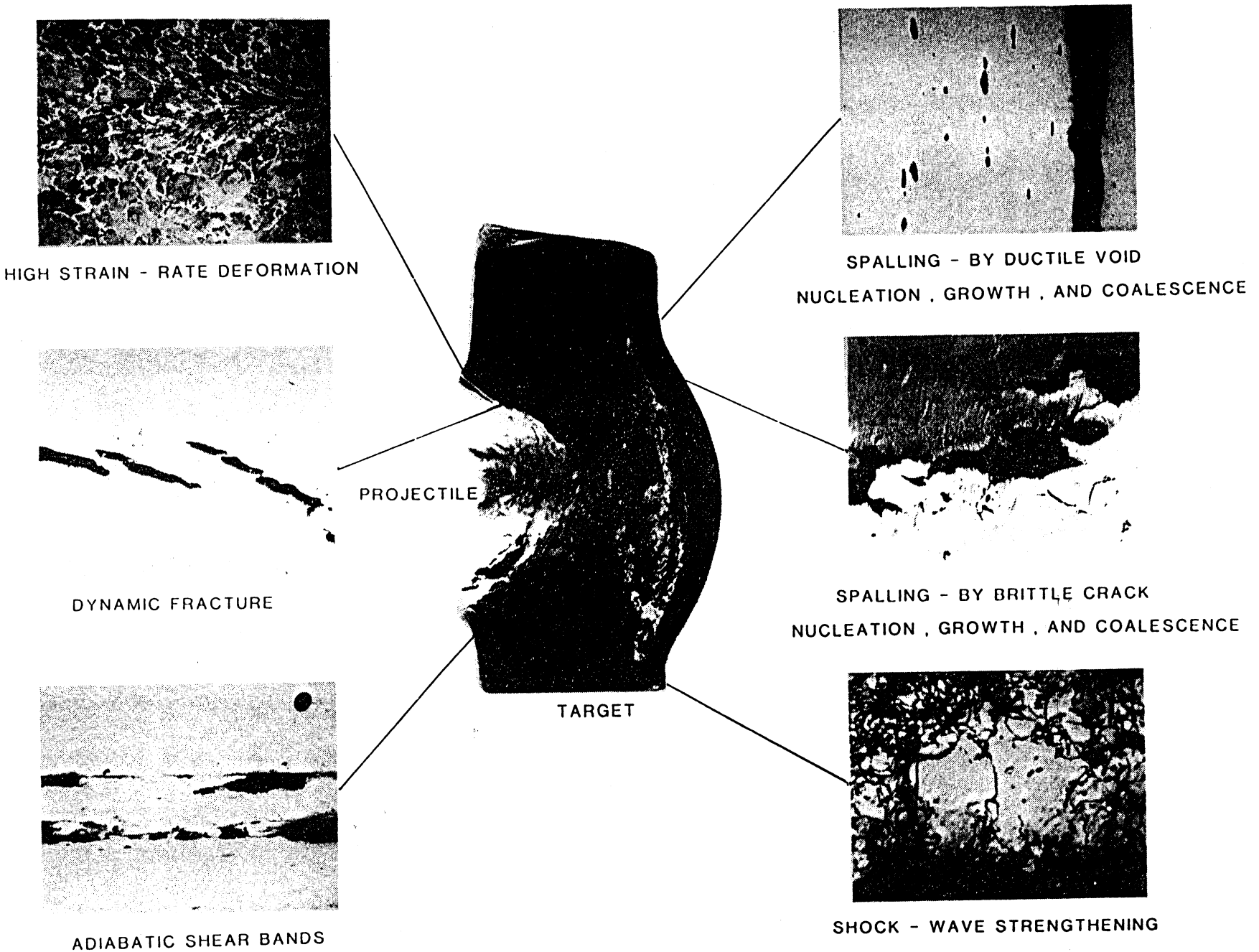

FIG. 1. Dynamic deformation system.

been investigated in the past thirty years and numerous papers describe the effects for a variety of metals and experimental conditions. They affect the mechanical properties; in general, one observes an increase in the flow stress with a corresponding decrease in ductility. These effects are described in Ref.,[4] among other sources. The fourth phenomenon, spalling, is clearly evidenced in the side of the target opposing the impact surface. The material is 'pulled out' of the back and complete separation occurs when the stress pulse amplitude and duration are sufficient. The description of dynamic fracture, which constitutes the main objective of this article, will be carried out in four sections. Section 2 will present a description of the fundamental requirements for spalling. The models developed with the objective of attaining a quantitative predictive capability and experiments conducted on a number of alloys to determine the dynamic strength are presented in Section 3. Section 4 concentrates on the metallurgical aspects of spalling, with some attempts at developing micromechanical deformation equations.

2. FUNDAMENTALS

Figure 2 shows four idealized situations under which dynamic fracture is obtained. Flat projectiles and targets are shown in order to render the explanation simpler. Figure 2(a) shows a projectile of thickness δ_1 impacting a target. Under dynamic conditions (wave-propagation regime) a plastic shock wave will propagate through the target, if the impact velocity is sufficient and the condition of uniaxial strain (ensured by lateral dimensions at least eight times the thickness of the target) is obeyed. This compressive shock wave reflects itself at the back surface of the target and cancels the incoming wave. This is explained in greater detail later in this section. When the cancellation is completed (bottom of Fig. 2a), a net tensile pulse results. If this pulse has sufficient amplitude it will cause separation of the material and "spalling". The configuration of Fig. 2(b) is slightly different. Here, the detonation of a high explosive in direct contact with the target generates a shock pulse in the latter. The expansion of the gases creates the pressure at the explosive–target interface which is responsible for the generation of the shock pulse. Shock pulses generated by direct-contact detonation are characteristically of a triangular shape; on the other hand, plate impact experiments produce pulses that have (initially) a square shape. The reflection and interaction of a triangular pulse is, by virtue of its shape, different from a square one. The distance from the back surface, at which the tensile reflected pulse is high enough to produce spalling, is marked by δ_2 in Fig. 2(b). It will be seen later that this configuration can induce multiple spalling.

The type of dynamic fracture occurring in the explosion of bombs and shells is best represented and studied by the expanding ring technique. Figure 2(c) depicts schematically this configuration. A ring of radius R is expanding under an internal pressure. If one does not consider the radial wave propagation caused by the initial explosion (and this is a reasonable assumption) and considers the mean outward velocity of the ring to be v_r, the uniform hoop strain rate is $\dot{\epsilon}_{\theta\theta} = v_r/R$. The points where the material exhibits some weakness will fail first, and there will be corresponding unloading waves starting at these points. Figure 2(c) shows three flaws f_1, f_2 and f_3 (f_3 being the weakest as the ring broke first at this position). The manner in which these unloading waves propagate will determine the size of the fragments; whether or not a flaw grows depends on its relative strength, as well as on its position with respect to the neighboring flaws. This type of dynamic fracture will not be treated in this monograph; the reader will find additional information in Grady.[5] A fourth type of dynamic fracture is shown in Fig. 2(d); the impact of projectiles (ideally, cylindrical

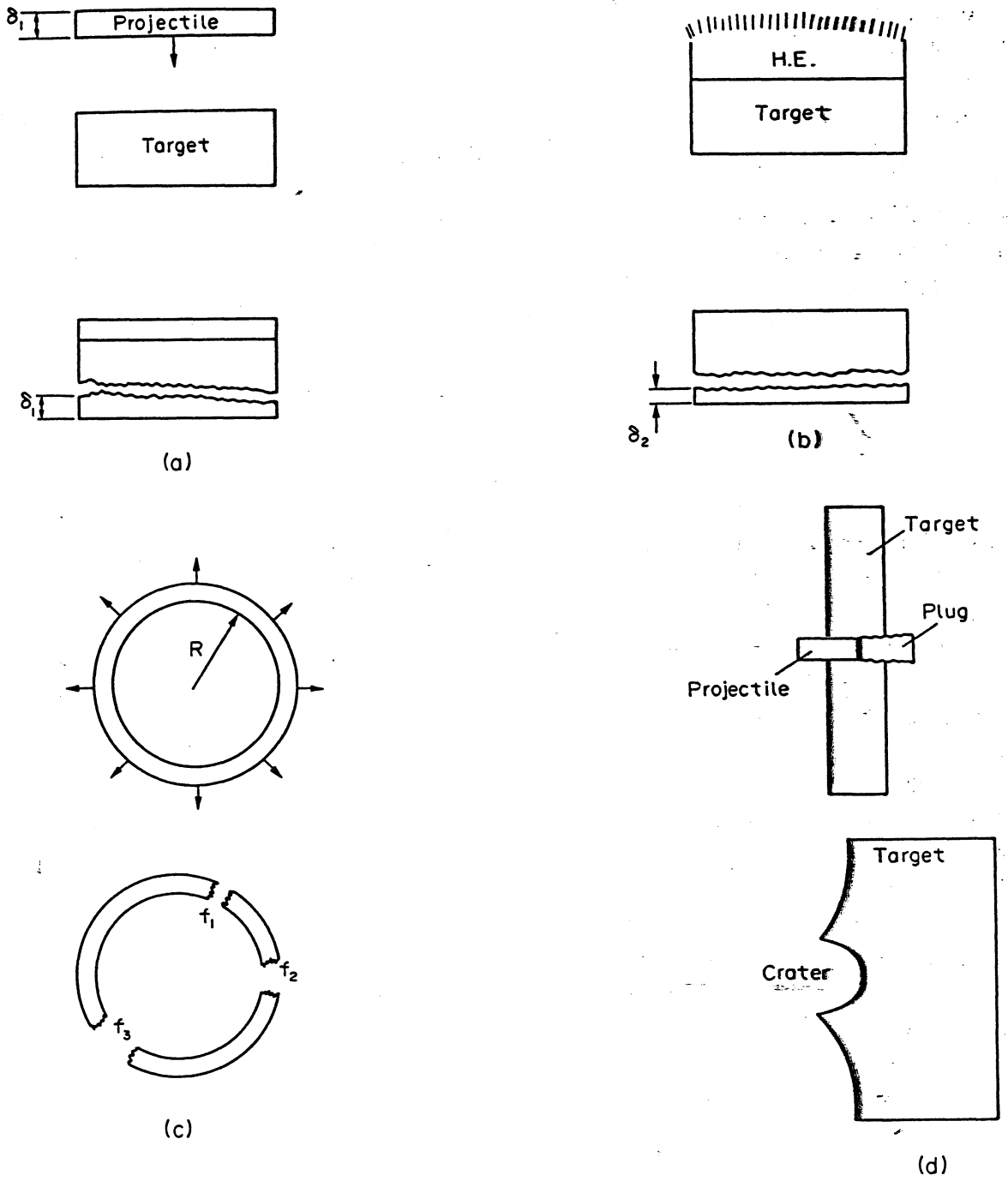

FIG. 2. Four configurations leading to dynamic failure. (a) Plate impact; (b) direct explosive detonation; (c) ring expansion; (d) projectile impact with plugging or cratering.

and spherical) produce plugging and cratering, respectively. In both cases, adiabatic shear bands are involved in the fracture generation and propagation process. In the case of plugging, the deformation is highly localized and quite different from the extensive target bulging that would be observed if the projectile were replaced by a low-velocity rod (quasi-static deformation). In a similar way, cratering produced by the impact of a spherical projectile is reminiscent of craters produced by the impact of meteorites. In both cases, a complex interplay of plastic waves, elastic waves, shock waves, shear localizations, and fracture nucleation and growth is responsible for the terminal damage. This type of fracture will not be addressed in this monograph; the focus will be primarily on the plate-impact configuration shown in Fig. 2(a). Both the pressure and the duration of the

shock pulse can be adjusted by means of the projectile velocity and thickness respectively, and the absence of plastic waves renders this configuration ideal for fundamental studies. For the direct-contact detonation configuration of Fig. 2(b), the peak pressure and rate of release of the wave (back side of saw-tooth pulse) are determined by the explosive and cannot be adjusted. Hence, a more detailed description of this configuration is presented below.

Elastic and plastic shock waves have been thoroughly investigated in the past. The velocity of elastic waves is determined by the elastic constants of the material. For the isotropic case:

$$v_L = \left(\frac{\lambda + 2\mu}{\rho}\right)^{1/2} \tag{1}$$

$$v_S = \left(\frac{\mu}{\rho}\right)^{1/2} \tag{2}$$

For the plane parallel impact we do not have to be concerned with shear waves. Shear waves (elastic and plastic) can be generated by parallel oblique impact between the projectile and the target; they have been investigated by Abou-Sayed and Clifton,[6] among others. Once the elastic limit of the material, under uniaxial strain conditions (called Hugoniot Elastic Limit, or HEL) is exceeded, one has the propagation of shock waves. At sufficiently high pressures one can consider the material essentially as a strength-free fluid and the equations of hydrodynamics determine the characteristics of the shock waves. In the intermediate range between the HEL and high pressures, strength and viscoplastic effects are important and affect the wave behavior. For more information, see Refs.[7,8] The Hugoniot–Rankine equations which provide relationships between the state variables are the equations that express the conservation of mass, momentum, and energy. Additional details can be found in Meyers and Murr,[4] among other sources. The five state variables (P: pressure; u_p: particle velocity; U_s: shock velocity; T: temperature; ρ: density) require one additional relationship in order to specify all four of them, once one is known; this is provided by an experimentally-established "equation-of-state" (of the form $U_s = C_0 + S_1 u_p$). The shock-wave velocity is related to the pressure by the following relationship:

$$P = \rho_0 u_p U_s = \frac{\rho_0 U_s}{S_1}(U_s - C_0) \tag{3}$$

where C_0 is the sound velocity at zero pressure and S_1 is an empirical parameter from the relationship between shock and particle velocities.

The shock-wave velocity is usually lower than the elastic precursor velocity at low pressures. Above a certain threshold called "overdrive stress", the shock-wave velocity exceeds that of the elastic wave, and no elastic precursor exists. This overdrive stress can be obtained from tabulations.

The plot typified by Fig. 3 is most helpful in understanding spalling. The left-hand side represents the projectile, while the right-hand side represents the target. At time $t = 0$, the projectile impacts the target. Elastic waves are emitted into the projectile and target; they are followed by plastic waves. In Fig. 3, the inverse of the slope of the diagonal lines gives the velocities of the waves; it can be readily seen that the elastic precursor has a higher velocity than the shock wave. As the elastic and plastic waves encounter the free surfaces of target and projectile, they reflect back. The $x - t$ regions corresponding to tension and

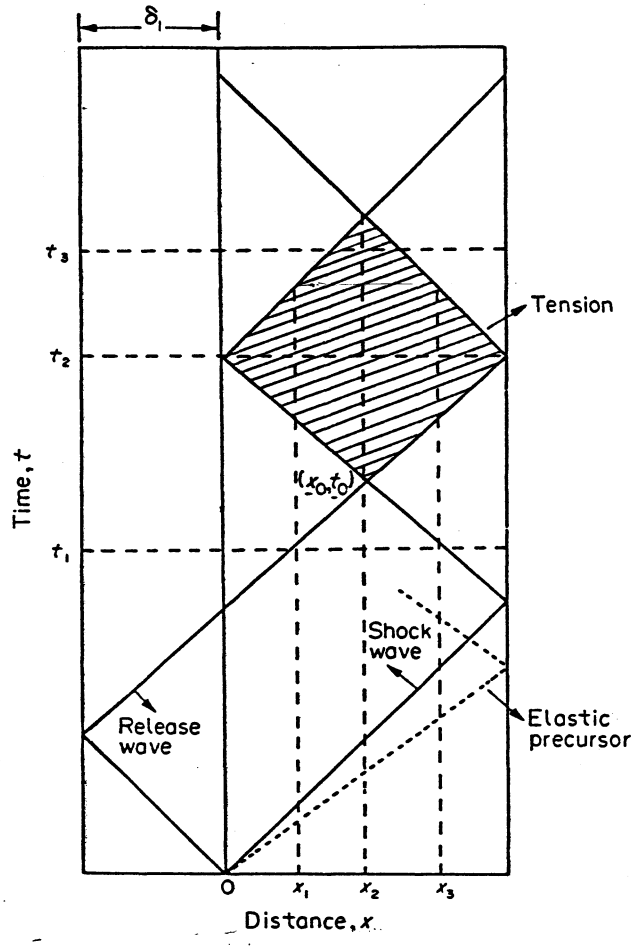

FIG. 3. Distance–time plot showing propagation of waves in target and projectile after impact.

compression are shown in Fig. 3. The elastic precursor is assumed, in this figure, to be small with respect to the total pulse amplitude. Figure 4 shows the stress pulses at three different times, whereas Fig. 5 shows the stress histories at three different positions. These cross-plots show how the wave configuration changes. Figure 4(a) shows a compressive pulse, at t_1; at t_2 one has a purely tensile pulse, and the same occurs at t_3. The stress histories at different positions x_1, x_2 and x_3 show the sequence of pulses. At x_1, a compressive pulse is followed by a tensile pulse, after a period of no pulse. At x_2, the tensile pulse follows the compressive pulse immediately. At x_3, the compressive and tensile pulses, which have a reduced duration, are again separated. Of importance is the fact that the first region to feel the tensile pulse is the one marked (x_0, t_0) in Fig. 3. It is presently known that spalling is dependent both on the amplitude and on the duration of the reflected tensile pulse. If this pulse is of sufficient magnitude to produce spalling it should occur at x_0; the plots of Figs 4 and 5 do not depict realistically the spalling process. Spalling will produce release waves at the newly created internal surfaces (spall surfaces) which alter the subsequent configuration of the pulses. This will be treated in greater detail in Section 3, where more realistic pulse shapes are presented. If the projectile and target are of the same material, the distance of the spall from the free surface should be roughly equal to the thickness of the projectile. This can be seen by observing the interaction of the waves. In Figure 3, the thickness of the flyer plate is indicated by δ_1. The travel time of the wave in the flyer plate (the compressive wave and the tensile reflected wave) determines the duration of the compressive wave in the target; this

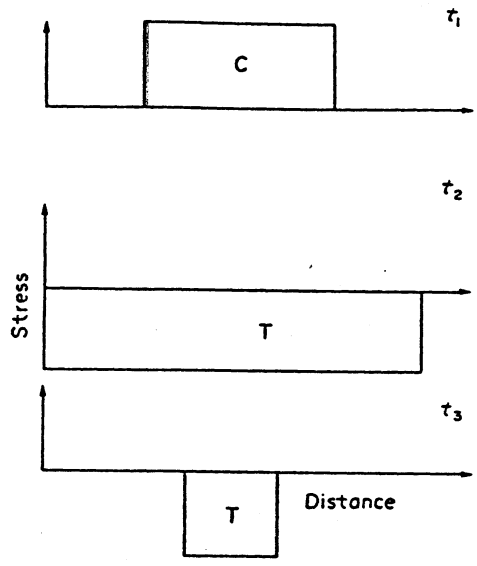

FIG. 4. Stress profiles at t_1, t_2, t_3.

latter one, in its turn, establishes the thickness of the spalled layer. Changes in the shape of the wave as it travels through the target as well as the elastic precursor and other factors complicate the picture in many cases; Section 3 will describe some of the models developed to incorporate these effects.

3. MECHANICS OF SPALLING

3.1. *Early Work*

In this section, a review will be conducted of the studies developed for spalling. The early period, up to the late 50's, is constituted of observations, exploratory investigations, and simple models. The 60's saw the advent of concentrated research of a more quantitative

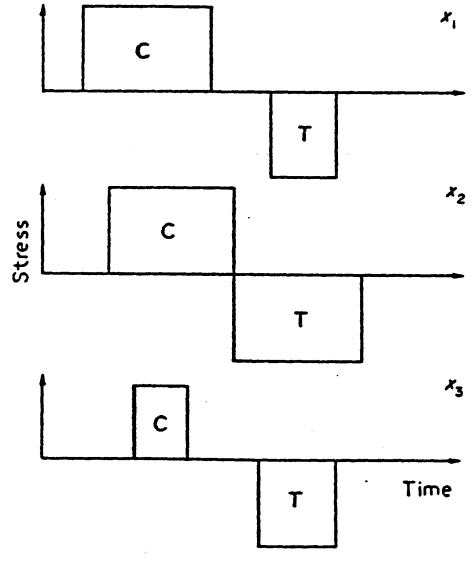

FIG. 5. Stress histories at three different positions.

nature, leading to theories taking into account the complexities of material behavior and lending themselves to utilization in computers and verification by actual experiments. To a large extent, this work was conducted by three groups: Stanford Research Institute, Los Alamos National Laboratory, and Sandia National Laboratories. A state-of-the-art appraisal of dynamic fracture and spalling is presented in the report by the National Academy of Sciences;[9] this report, prepared by a committee of experts and headed by W. Herrmann, devoted a great deal of effort to the identification of areas that require additional work. In this section, the work conducted by the various groups will be reviewed and some of the areas requiring further work will be highlighted.

It seems that Hopkinson[10,11] was the first to investigate spalling, in the beginning of the century. The two excerpts below show that he correctly identified a spall:

> "...iron or steel may become brittle under sufficiently great forces applied for very short times. No ordinary hammer blows will do, but the blow delivered by a high explosive is quick enough. If a slab of wet gun-cotton be detonated in contact with a mild steel plate, a piece will be blown out and the edges will show a sharp crystalline fracture with hardly any contraction of area.... Yet this same plate could be bent double in a hydraulic press".
> "The fact that a blow involving only pressure may, by the effects of wave action and reflection, give rise to tension equal to or greater than the pressure applied, often produces curious effects. [As an illustration]... If such a cylinder of gun-cotton weighing one or two ounces be placed in contact with a mild steel plate, the effect, if the plate be half an inch thick or less, will be simply to punch out a hole of approximately the same diameter as the gun-cotton... But if the plate be three-quarters of an inch thick, the curious result... is obtained. Instead of a complete hole being made, a depression is formed on the gun-cotton side of the plate, while on the other side a scab of metal of corresponding diameter is torn off, and projected with a velocity sufficient to enable it to penetrate a thick wooden plank... The velocity in fact corresponds to a large fraction of the whole momentum of the blow... The separation of the metal implies, of course, a very large tension, which can only result from some kind of reflection of the original applied pressure, but the high velocity shows that this tension must have been preceded by pressure over the same surface, acting for a time sufficient to give its momentum to the scab..."
> "I caused then a two-ounce cylinder of gun-cotton to be detonated in contact with a somewhat thicker plate. In this case no separation of metal was visible; the only apparent effects being a dint on one side and a corresponding bulge on the other. On sawing the plate in half, however, I was gratified to find an internal crack, obviously the beginning of that separation which in the thinner plate was completed".

He also indicated the increased brittleness of steel under dynamic conditions; he described the brittle appearance (which he called "crystalline fracture") of the fractures produced dynamically and the very small amount of plastic deformation associated with them.

During World War II a renewed interest in dynamic fracture and fragmentation was noticed, and some work of a fundamental nature was conducted. Mott[12] studied the fragmentation of metal rings and cylinders loaded internally by explosives and theoretically determined distributions of fragment sizes. Figure 2(c) shows the stress configuration that is obtained. Mott introduced the concept of the statistical activation of fracture coupled with the propagation of elastic and plastic relief waves at the newly created surfaces. This is shown in Fig. 6; relief waves propagate circumferentially, starting from the fracture sites. They reduce the stress to zero in these regions, inhibiting further fragmentation. Additional time-dependent fracture can only occur in the regions not relieved from the tensile stress.

Little additional attention was given to spalling[14,15] until, in the early 50's, Rinehart[16,17] reported the results of systematic experiments on steel, brass, copper and an aluminum alloy using a modification of Hopkinson's[10,11] technique. He found that there was a critical value of the normal tensile stress (σ_y) required to produce spalling, and that this value was a characteristic of the material. He also observed and correctly explained the phenomenon of multiple spalling produced when a triangularly-shaped pulse is reflected

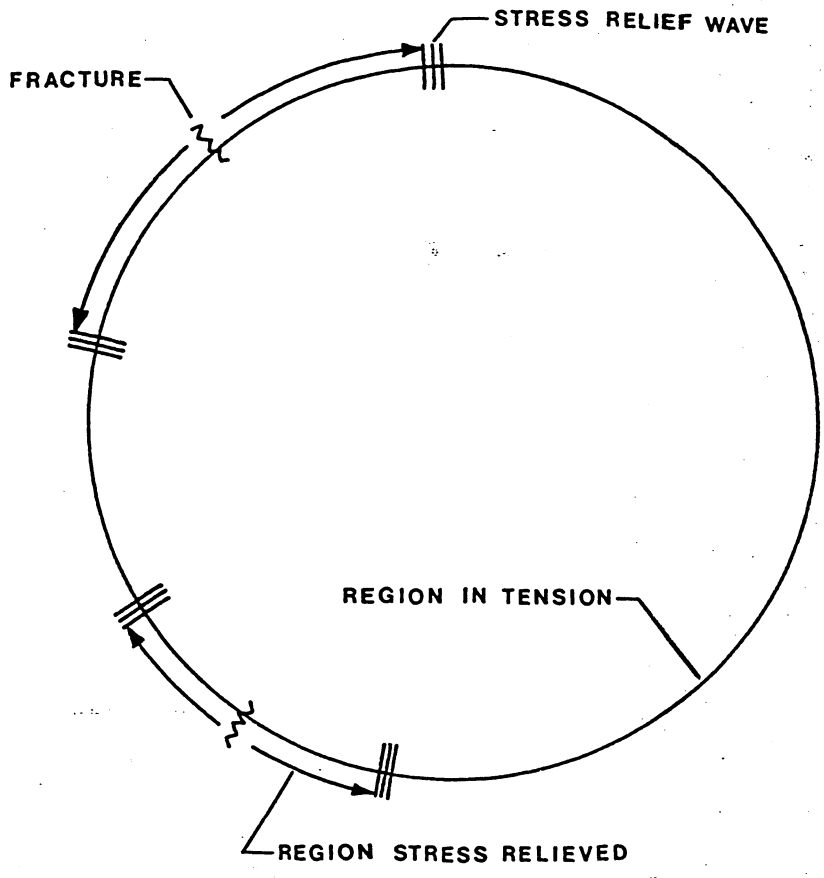

FIG. 6. The one-dimensional Mott problem.

and has an amplitude substantially higher than σ_c. He proposed the following expression for the thickness of the spalled layers (direct contact explosives detonating on top of the metal were used):

$$\delta_1 = \frac{x_1}{2} \tag{4}$$

where x_1 is such that: $\sigma(x_1) = \sigma_0 - \sigma_c$. For the second spall, the thickness δ_2 is:

$$\delta_2 = \frac{x_2 - x_1}{2} \tag{5}$$

where $\sigma(x_1) - \sigma(x_2) = \sigma_c$. Figure 7 shows the sequence of spalling as well as the stress distribution function. The shape of the pulse determines the distances δ_1, δ_2, etc. The process repeats itself until the stress value of the wave has been reduced to less than σ_c. Shortly after Rinehart's experiments, Skidmore[18] and Breed *et al.*[19] published their results. Breed *et al.*[19] determined the spall strength of Al, Cu, Ni and Pb by flash radiography.

3.2. *Major Research Effort*

Table 1 shows in a synoptic way the main research efforts conducted since Rinehart's work. The three groups at Los Alamos, Sandia, and Stanford Research Institute have played a key role in the development of the present understanding of spalling. For this

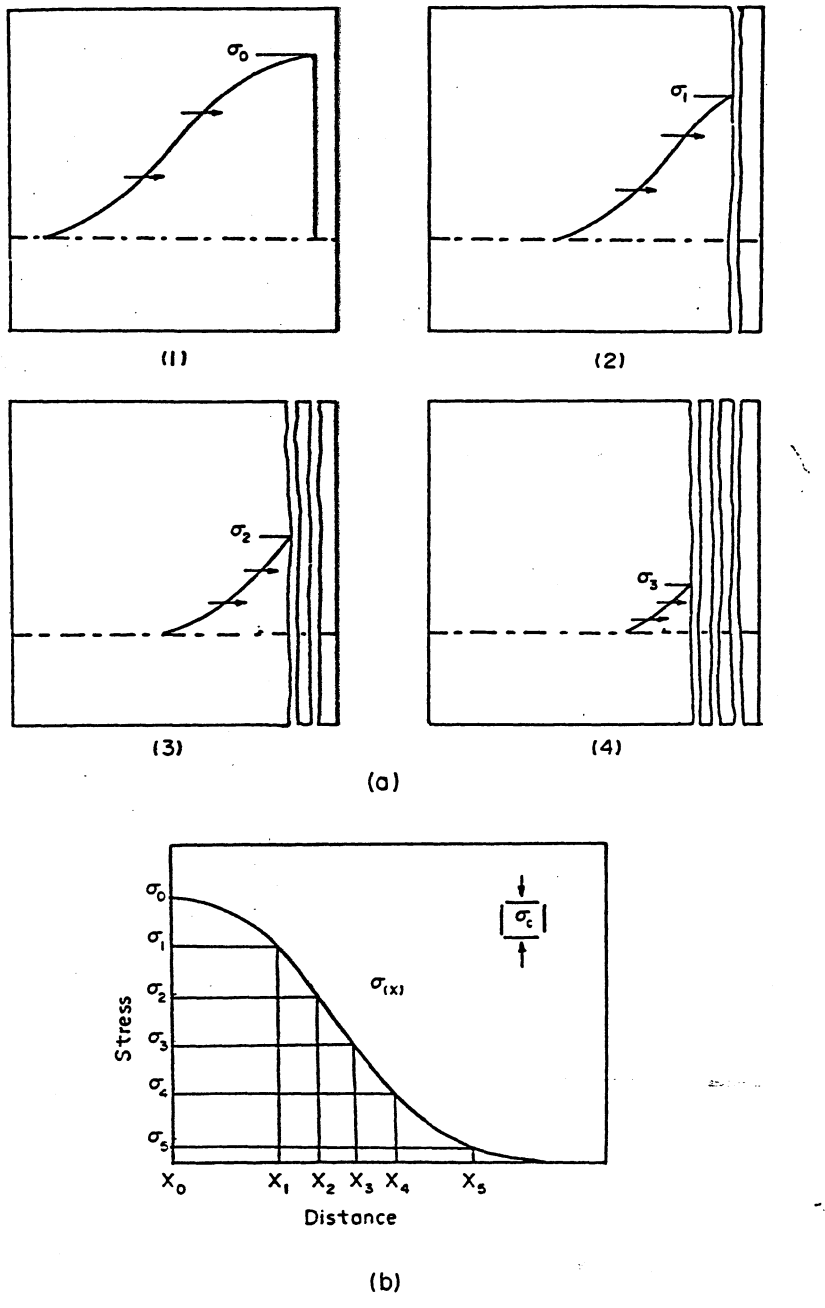

FIG. 7. (a) Process of multiple spall generation. (b) Corresponding profile of stress with positions of various stress levels that are separated by c. (From J. S. Rinehart, *J. Appl. Phys.*, **23** (1952) 1229, Figs 3 and 2.)

Table 1. Major research efforts in spalling*

Group	Investigators	Year	Nature of Study
Los Alamos	Smith[20]	1958	Wave reflection of free surface iron
	McQueen and Marsh[21]	1962	Spall Strength of Copper (complete separation)
	Breed, Mader and Venable[19]	1967	Spall strength of Al, Cu, Ni, Pb
	Johnson[22]	1981	Model for spalling by void nucleation and growth

(*Continued*)

Table 1—continued

Group	Investigators	Year	Nature of Study
Sandia	Butcher, Barker, Munson and Lundgran[23]	1964	Confirmations that spalling is a time-dependent mechanism. Use of SWAP code.
	Tuler and Davies[24]	1968	
	Stevens and Tuler[25]	1971	
	Davison and Stevens[26]	1972	Continuum measure of spall damage
	Stevens, Davison and Warren[27]	1972	Model for void growth
	Stevens and Pope [28]	1973	Spall in titanium
	Davison, Stevens and Kipp[29]	1977	Theory of spall damage for ductile solids
	Davison and Stevens[30]	1973	Theory of spall damage for brittle solids
	Davison and Graham[1]	1979	General Review
	Grady[5]	1981	Fragmentation
	Grady[31]	1981	Fragmentation theory
Stanford Research Institute	Erlich, Wooten and Crewdson[32]	1971	Spalling of glycerol
		1971	(by void nucleation + growth)
	Curran[33]	1971	Spalling in iron at room temp. and 300°C.
	Barbee, Seaman, Crewdson and Curran[34]	1972	Broad study of spalling ductile and brittle materials; use of PUFF code.
	Seaman, Shockey and Curran [35]	1973	Dynamics of crack growth in spalling
	Curran, Shockey and Seaman[36]	1973	Spalling of polycarbonate
	Shockey, Seaman and Curran[37]	1973	Microstructural effects of spalling
	Seaman, Curran and Shockey[38]	1976	Models for nucleation and growth; use of NAG code
	Curran, Seaman and Shockey[39]	1977	Descriptive overview of State-of-the-art NAG-FRAG code.
	Shockey, Dao and Jones[40]	1979	Spalling in tatanium; effect of grain size.
	Shockey, Curran and Seaman[41]	1979	Models and codes
	Seaman, Curran and Crewdson[42]	1978	Topology of cracks
	Curran, Seaman and Shockey[43]	1981	Modeling vs. experiments
	Moss and Seaman[44]		Threshold stress for spall damage in Ni–Cr Steel.
Other Groups			
U. of Tokio	Takahashi[45]	1973	Spalling in PMMA
Weizmann Inst. of Science	Maron and Blaugrund[46]	1982	Instrumented observation of spalling in copper and aluminum
CEA-France	Dormeval, Chevallier and Stelly[47]	1981	Dynamic fracture for long pulse durations ($\sim 20\ \mu s$).
BRL	Rosset[48]	1973	Modeling of void coalescence
GM	Warnica[49]	1968	Spalling of berillium
USSR	Altshuler, Novikov and Divnov[50]	1966	
U. of Washington	Jones[51]	1973	Effects of metallurgical variables on spalling in 2024 and 6061 aluminum
	Jones and Dawson[52]	1973	
	Axter, Jones and Polonis[53]	1975	
Rutgers/BRL	Dietrich and Greenhut[54]	1973	Effect of spalling on recrystallization
	Greenhut, Chen, Banks and Golaski[55]	1975	Effect of spalling on aging kinetics
New Mexico Tech.	Murr[56]	1975	Grain-boundary separation in molybdenum
Naval Surface Weapons Center	Mock and Jones[57]	1982	Spalling in HF-1 steel (fitted to SRI NAG-FRAG)

*USSR and Lawrence Livermore activity is described in the addendum.

reason the papers are grouped by research institution in Table 1. One should at this point make a distinction between levels of spall damage. Figure 8(a) shows a steel and a nickel plate after they were sectioned. The lower surface is completely separated from the top surface at the center; no separation occurred in the sides because the lateral release waves eliminated the shock wave (produced by the impact of a flyer plate on the top surface of the plates. This type is commonly referred to as "complete spall". The process of spalling does not involve the propagation of one single crack or failure front. In this way, it differs significantly from quasi-static fracture. Rather, one has the independent nucleation and growth of microfailure regions; these are either voids or cracks. The rate at which the tensile load is applied is such that the growth of the individual microfailure regions occurs without interference from the ones that are more distant. On the other hand, in quasi-static failure the growth of a crack proceeds by the alteration of the stress field ahead of it; the nucleation of other microfailure regions is obviously affected if one superimposes the stress field due to the crack to the applied stress. Figure 8(b) shows the section of a specimen that, macroscopically, has not spalled. If one observes it microscopically, one can observe a number of microflaws which formed in the region where the tensile reflected pulse had a maximum amplitude and duration. This spall damage is sometimes called incipient spall. The growth and coalescence of these microvoids/microcracks will evantually lead to complete spalling. The extent of spall damage is dependent on shock-wave parameters (stress, duration of the stress, stress gradients, strain rate, etc.) and material parameters.

The first shock-wave parameter to be recognized as important was the tensile stress, as evidenced in Rinehart's[16,17] work. McQueen and Marsh[21] continued this work and obtained tensile stresses of the order of 15 GPa for complete spalling of copper. Continued experiments by Smith[58] and Blincow and Keller[59] showed that the thickness of the

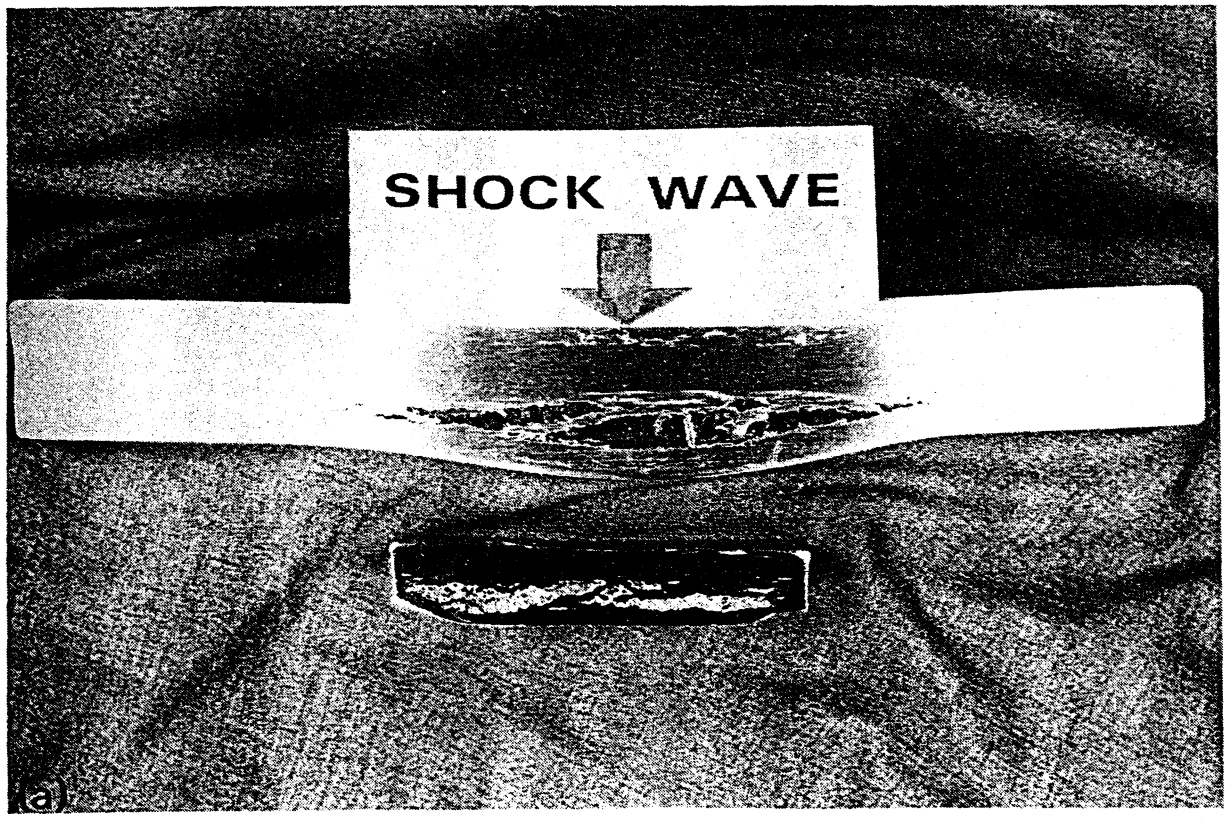

FIG. 8.

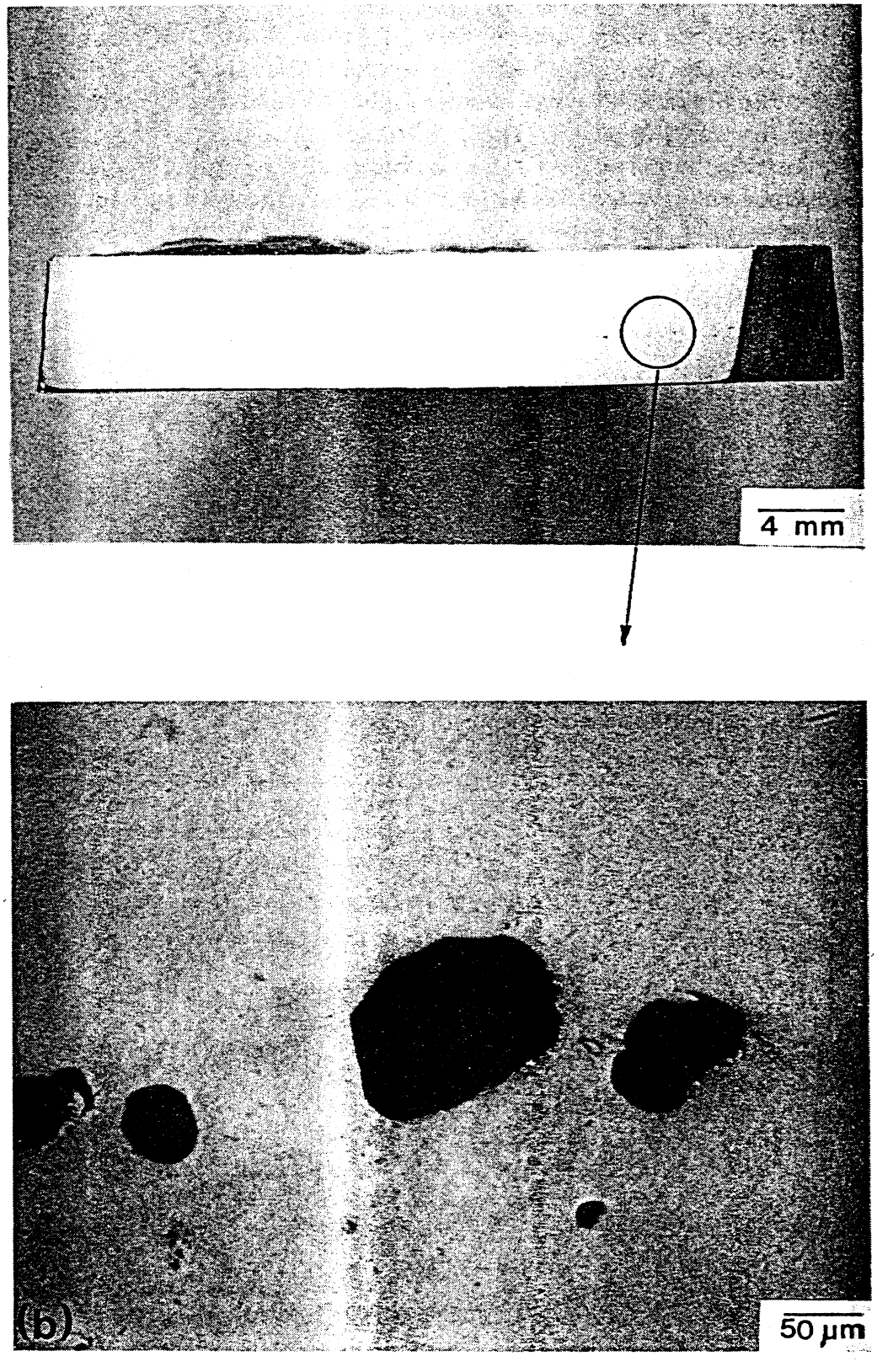

FIG. 8. (a) Complete spalling of AISI 1008 steel (large plate) and nickel plate. (Spec. A and B)
(b) Incipient spall damage in copper (specimen courtesy of D.A. Shockey, S.R.I.). (Spec. H.)

projectile affected the spall threshold; Smith[58] found three thresholds for spalling in copper. In 1964, Butcher *et al.*[23] published a comprehensive paper in which they presented a description of the growth of the failure; they confirmed Smith's and Blincow and Keller's results and said, for the first time, that the fracture mechanism is not instantaneous; it depends on the rate of crack (or void) initiation and propagation. Therefore, the duration of the tensile pulse is also important. The importance of characterizing the stress pulse at various positions was evidenced by the development of a computer code to describe the stress history. This code, named SWAP, was based on the strain-rate independent elastic–plastic theory. As an illustration, a sequence of pulse shapes predicted by SWAP-2 is shown next. Figures 9 and 10 show predictions of stress histories at various positions inside AISI 304 stainless steel target (9.6 mm thick) impacted by a projectile of the same material (5 mm

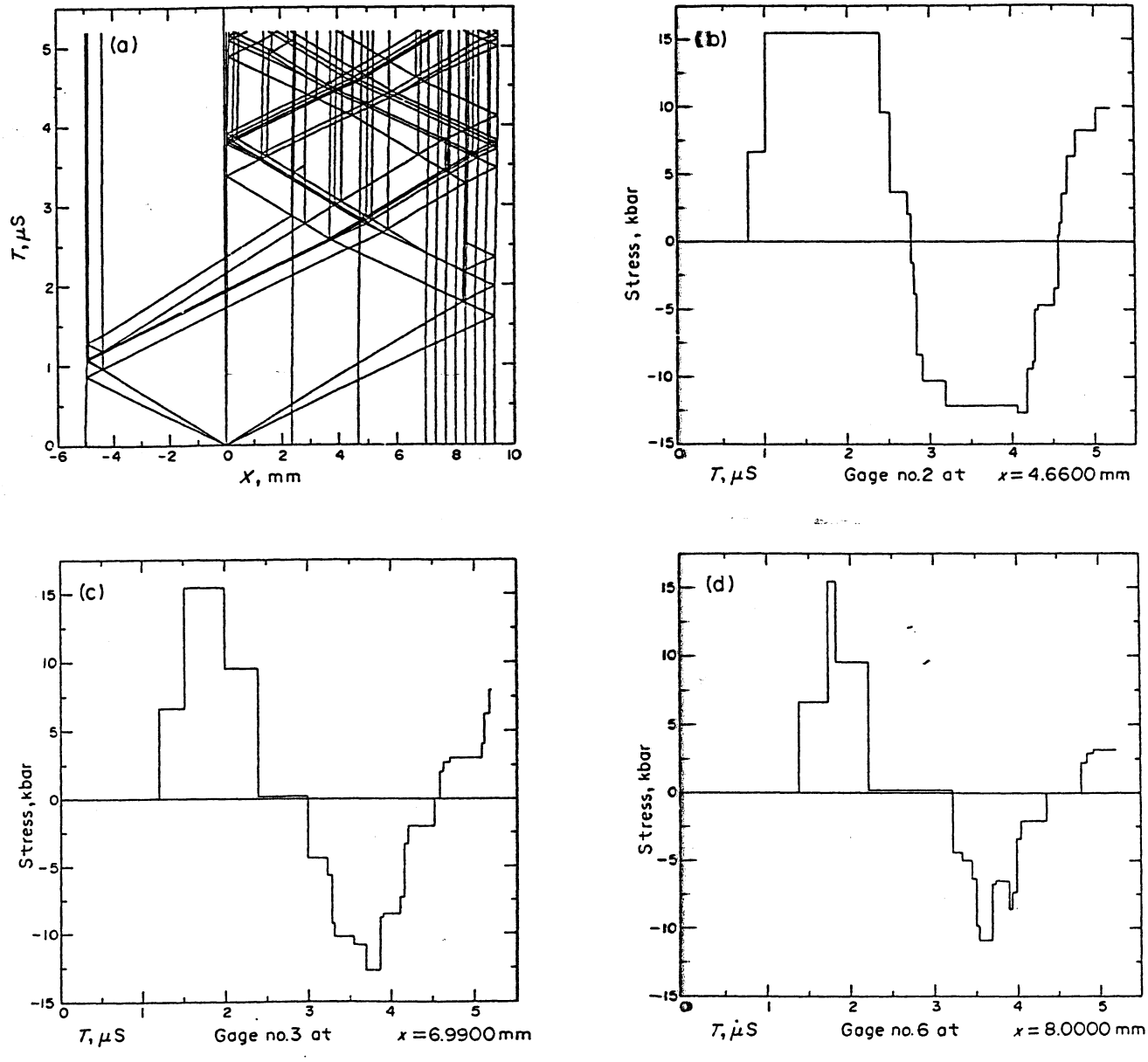

FIG. 9. Computer simulation (SWAP-2) of impact of 5 mm-thick projectile against 9.6 mm-thick target (both of SISI 304 SS) without spalling. (a) Distance–time diagram. (b) Stress history at 4.66 mm form impact interface. (c) Stress history at 6.99 mm from impact interface. (d) Stress history at 8.00 mm from impact interface. (Courtesy of D. C. Erlich, Stanford Research Institute.)

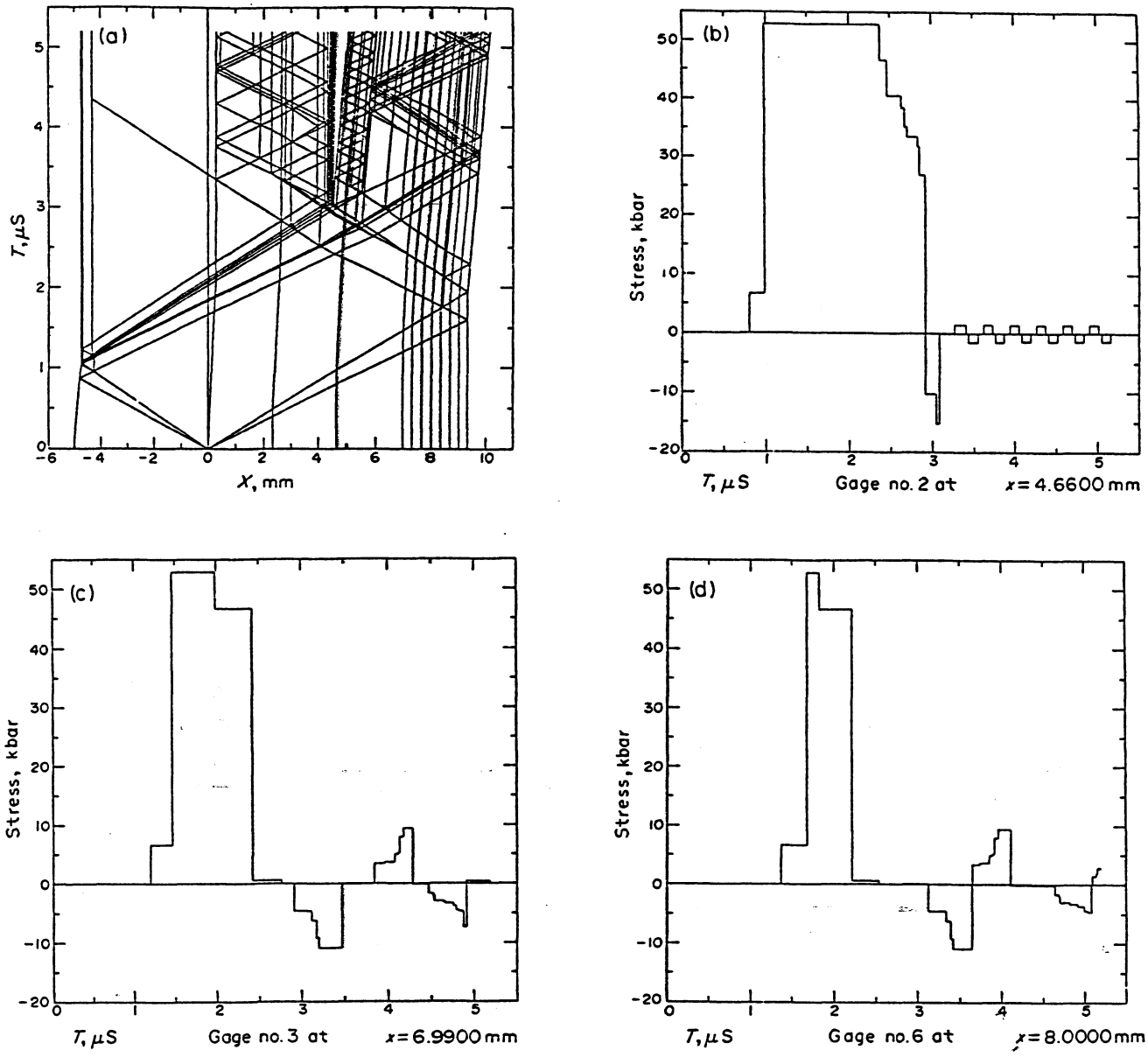

FIG. 10. Computer simulation (SWAP-2) of impact of 5 mm thick projectile against 9.6 mm-thick target (both of AISI 304 SS) with spalling; tensile strength of specimen assumed to be equal to 1.52 GPa. (a) Distance–time diagram. (b) Stress history at 4.66 mm from impact interface. (c) Stress history at 6.99 mm from impact interface. (d) Stress history at 8.00 mm from impact interface. (Courtesy of D. C. Erlich, Stanford Research Institute.)

thick). It is a one-dimensional code, and is nowadays obsolete, but it is very helpful to obtain a first estimate of the effects to be expected. One sees, in Figs 9(a) and 10(a), the distance–time (x–t) plots, incorporating the elastic precursors and their interactions with the wave. While Fig. 9 simulates the case where the metal does not spall, Fig. 10 assumes that the tensile strength of the metal is 1.52 GPa, which is lower than the tensile stress; in the latter case, one sees the spall forming in the x–t plot at a specified time, and the production of release waves at the newly formed internal surfaces. One can see that the region at 4.66 mm from the impact interface is the one that *experiences the tensile pulse first* ($\sim 3\ \mu$s after impact). As the metal spalls, the stress experienced by the adjacent regions is reduced, because of the release of the tensile pulse due to the free surfaces. One can see that by

comparing the tensile portion of the pulses in Figs 9(c) and 10(c). One should emphasize that SWAP does not take into account the dynamics of the formation of the spall, and does not predict incipient and intermediate spall damage. Being one-dimensional, the lateral dimensions of the plate are assumed infinite and the lateral release waves, very important when projectile and/or target have finite lateral dimensions, are not considered. More contemporary codes incorporate these important features.

3.3. *The Sandia Work*

In 1971, Stevens and Tuler[25] investigated the effect of the amplitude of the compressive shock wave which precedes the tensile pulse that produces spalling; they concluded that shock-wave strengthening does not have a significant effect on the dynamic tensile strength of 1020 steel and 6061-T6 aluminum. Previous experiments conducted by Buchanan and James[60] on mild steel with varying precompression pulses, showed that the spall strength increased linearly with the precompression amplitude; however, the duration was not kept constant. Stevens and Tuler,[25] on the other hand, took into account this fact and maintained a constant pulse duration; no effect of the precompression was found on the spall strength. The technique consisted of using a backup material behind the target in order to change the amplitude of the reflected pulse for the same compressive pulse, due to the differences in shock impedance. Figure 11 shows the results of their experiments; the compressive and tensile pulses were computed from the measured impact velocity by means of a SWAP-9 computer code. Davison and Stevens[26] introduced the concept of a continuum measure of spalling after reviewing the existing spall criteria and systematizing them. They classified them into *instantaneous* and *cumulative*; *local* and *nonlocal*; instantaneous, if spalling depends only on current values of the field variables, and cumulative if it depends on the history of these variables; local, if only values of field variables at a candidate spall plane enter into the determination of damage of this plane, and nonlocal if field values at distant points also have a bearing on the determination. Further, the cumulative-damage criteria are classified into *simple* and *compound*; simple, if the mechanism of damage accumulation does not depend on the amount of previously accumulated damage, and compound, if it

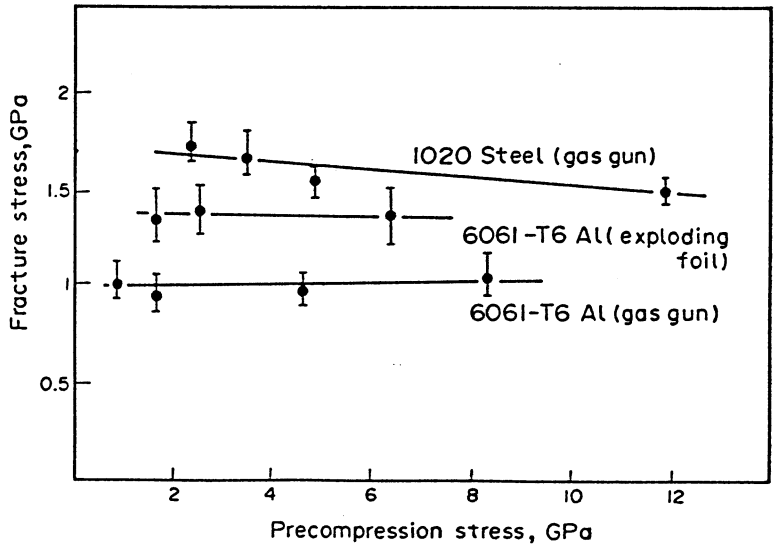

FIG. 11. Tensile stress amplitude required to produce incipient spalling as a function of compressive stress amplitude. (From A. L. Stevens and F. R. Tuler, *J. Appl. Phys.*, **42** (1971) 5665, Fig. 5.)

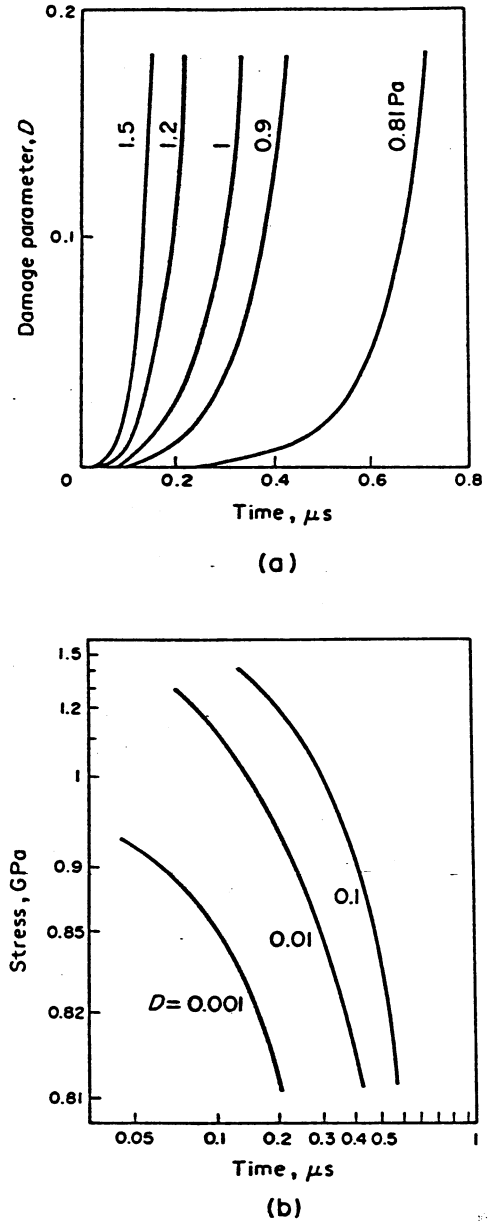

FIG. 12. Spall damage prediction according to Davison and Stevens'[26] theory. (a) Time dependence of accumulated spall damage for five different pressures (0.8, 0.9, 1, 1.2 and 1.5 GPa). (b) Curves of constant damage (D) in time–stress plane. (From L. Davison and A. L. Stevens, *J. Appl. Phys.*, 43 (1977) 988, Figs 1 and 2.)

does. Davison and Stevens[26] introduced a continuous measure of damage, D, and proposed a theory of compound-damage accumulation. Their function D can be assumed to be the degree of separation along the spall interface and varies from 0 (no incipient spall) to 1 (complete spall). Their predictions are shown in Fig. 12. One can see that, for a constant pressure, the damage increases with time. At 0.8 GPa, there seems to be a time delay of 0.3 μs before damage starts occurring. Davison and Stevens' theory is phenomenological in the sense that no detailed mechanisms for the initiation and propagation of microfailures are incorporated. In 1973; Davison and Stevens[30] presented a more detailed theory for spall damage for the case where failure occurs by the initiation and propagation of cracks. The damage was represented by vector fields describing the size and orientation of the

cracks. This continuous treatment eliminated the consideration of individual cracks, the stress concentration around each crack, its orientation, size, and location, etc. The theory was applicable to alloys exhibiting brittle behavior under dynamic conditions, such as iron and beryllium. Later, in 1977, Davison *et al.*[29] published a detailed theory for the case where spalling occurs by void nucleation and growth (ductile spall damage). The ductile and brittle spalls, shown schematically in Fig. 1, are described in greater detail in Section 4. These seem to be the two most common modes of failure. Davison *et al.*[29] assumed a viscoplastic behavior for the material in the establishment of the equations simulating spherical void growth. They computed the damage D as the void volume percentage in the spall region. Incorporating their dynamic void nucleation-and-growth parameters into a WONDY code (a one-dimensional Lagrangian wave propagation code using finite-difference method), they were able to compare experimental results with computations. The WONDY code was developed at Sandia for shock-wave computations. The results obtained for a 3.5 mm-thick fused-quartz projectile impacting a 1100-O aluminum alloy target (6.4 mm thick) are shown in Fig. 13. The impact velocity of 142 m/s yielded a pressure in the target of 1.0 GPa. Figure 13(a) shows the calculated and observed velocity histories in the back surface, for both the case of spalling and no spalling. The experimental measurements were made by laser interferometry (using the Sandia VISAR system). When no spall is observed, the free surface velocity should return to zero after the passage of the shock pulse ($\sim$2.5 μs). The formation of the spall, on the other hand, generates a release wave that produces the hump behind the shock wave, once it reaches the back surface ($\sim$3.0 μs). Davison *et al.*[29] call this hump the 'spall cusp'. One can see the good agreement between observations and calculations. It should be noticed that the WONDY code, incorporating void growth dynamics, simulates spalling much more realistically than the early SWAP code. Figure 13(b) shows the calculated damage as a function of position after various times, and one can clearly see the peak at approximately 3.5 mm. This is, as discussed briefly in Section 2, the thickness of the projectile. The final state, represented by the dashed line, corresponds to a time of approximately 3.5 μs. Figure 13(c) shows more clearly how the degree of damage drops slightly from its maximum value of 2.8 μs. In addition to the time dependence of damage, Fig. 13(c) shows more time dependence of stress and temperature, for both the cases of spall and no spall. The stress required for nucleation of the voids is taken to be much larger than the one required for growth. There is also a considerable amount of heat generated in the growth of voids, as shown by the bottom plot.

Davison and Graham,[1] in a comprehensive review on the effects of shock waves on materials, summarized the information available on the spall strength into a single table, reproduced here, after some simplifications and adaptations (Table 2). One can see that the incipient spall strength varies substantially. The highest reported value is for the AM 363 steel; values for different pulse durations (determined by the projectile thickness) are given with a hyphen. Davison and Graham[1] state that, while most fundamental models are developed for spherical voids and cracks, technical alloys often exhibit "blunted cracks". They also state that most research has been devoted towards establishing spall criteria; the concept of spall damage is, in modern work, quantified as the number density and size distribution of the cracks and voids in the material (this will be discussed in greater detail in Section 3.3). At low damage levels, they are typically 10^4/mm^3 and 1–100 μm radius, respectively.

Recently, Grady[31] extended Mott's[13] theory on the expansion of a ring driven by an internal explosion and its subsequent fragmentation. The fragment size distribution calculated by him using survival statistics for the case of ductile fracture compared very favor-

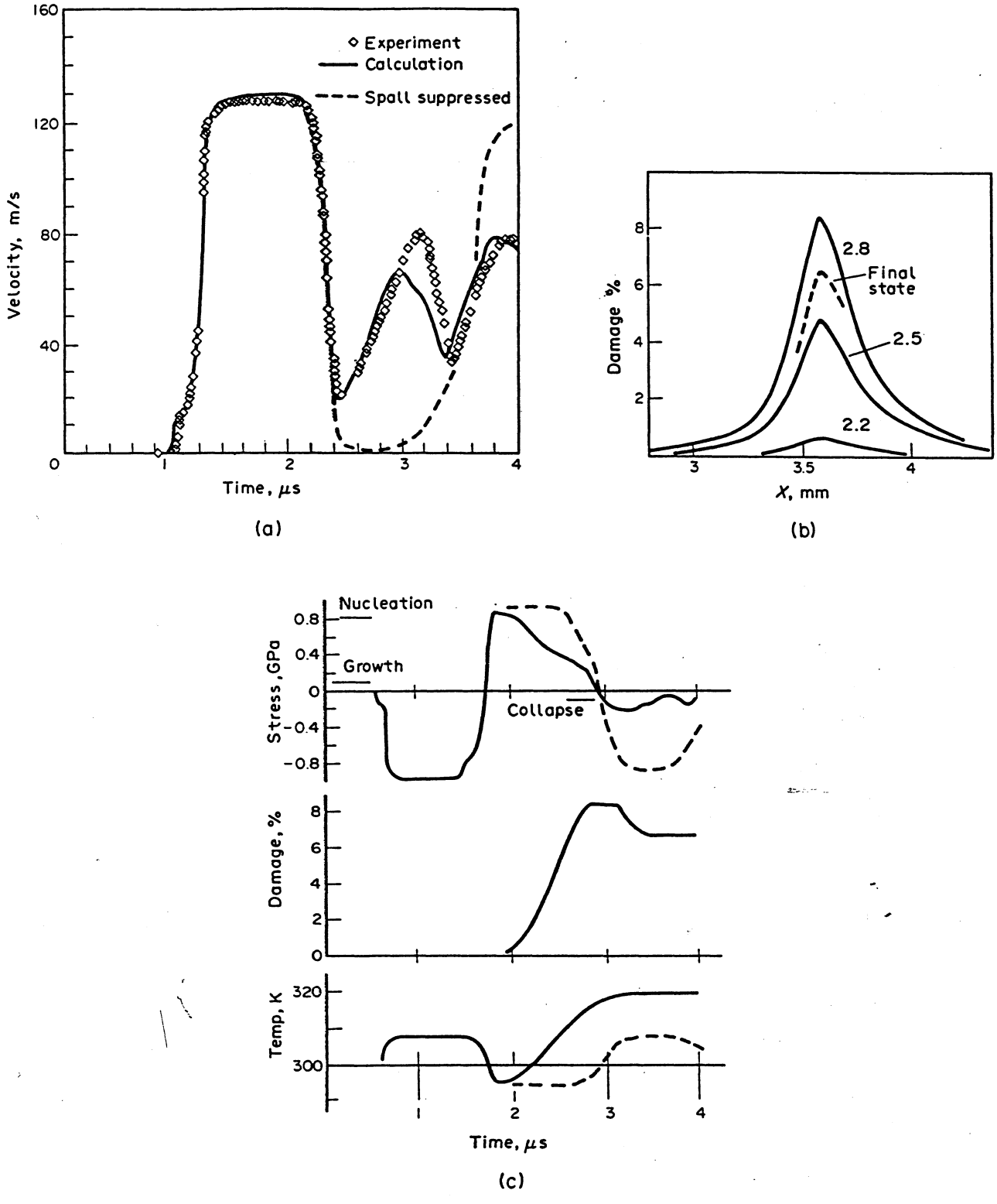

FIG. 13. (a) Calculated and observed velocities of free surface of target. (b) Calculated void volume distributions in central region of 6.4 mm target. (c) Calculated histories of axial stress component, damage function D, and temperature (3.57 mm from impact interface). Dashed lines correspond to case where damage is suppressed. Stress thresholds for nucleation, growth, and collapse of voids marked in plot. (From L. Davison, A. L. Stevens and M. E. Kipp, *J. Mech. Phys. Sol.* 25 (1977) 11, Figs 3, 5 and 6.)

Table 2. Incipient spall strengths (adapted from Davison and Graham[1])

Material	Spall Strength (GPa*)	Projectile thickness (mm)	Character of Damage	Method**
Aluminum & alloys				
Al	1.0	1.58	ductile voids	M
1145	0.5–1.1	1.14–5.84	ductile voids	M
2024-T4	1.25	3.8	blunt cracks	M
2024-T81	0.6	3.36	blunt cracks	M
2024-T86	2.0–1.8	0.3–1.0		V, PB
6061-T6	1.5–0.8	0.25–1.75	blunt cracks	M
6061-T6	1.0	3.17	blunt cracks	M
6061-T6	2.0–1.3	0.25–4.0	blunt cracks	M,PB
6061-T6	2.3–0.8	0.25–6.35	blunt cracks	M
2014-T6	1.76–1.47	0.61–1.57	blunt cracks	M
AMg-6	2.14–1.36	3.0–5.0	blunt cracks	M,V
Beryllium				
a-cut crystal	1.0	1.27 (quartz)	prism cleavage	M
c-cut crystal	1.15	0.76 (quartz)	basal cleavage	M
HP-10	0.92	1.02 (quartz)	cleavage	M,PB
HP wrought ingot	0.54–0.36	1.27–5.08	cleavage	M
S-200	1.3–0.78	0.64–2.54		
N50A	0.9–0.5	0.25–5.08	irregular crack	M
Brass, 60–40	1.4	6.35		M
Copper				
OFHC	0.95–0.75	1.5–3.2	blunt cracks	M
OFHC	2.5–1.8	0.5–3.0	voids and cracks	M
OFHC	2.3–0.62	0.4–1.6	voids and cracks	M
Iron and Steel				
Fe(99.99%)	1.9	1.16	brittle cracks	
Armco iron	3.5–1.7	0.51–2.36	brittle cracks	M
1020	1.6	3.17	brittle cracks	M
4340 Rc15	2.5	6.35		
Rc 54	4.1	6.35		
Rc 52	5.3	6.35		
Armco 21-6-9	3.7	3.2–12.8		PB
AM 363	4.5–2.1			PB
Titanium	3.9–2.1	0.22–4.09	blunt cracks	PB
	3.7–2.2	0.4–6.0	voids, cracks	M
Uranium	2.4	0.77–3.01		PB

*All values inferred from plate-impact experiments done at ambient temperatures with thickness ratios approximately 2 to 4.

**V—visual inspection; M—microscopic examination; PB—inferred from free-surface velocity history.

ably with experimental results obtained by Wesenberg and Sagartz[62] (6061-T6 aluminum cylinders expanded at a circumferential strain rate of $10^4\,s^{-1}$ by means of a capacitive discharge). Grady[31] then developed a general expression for the sizes of fragments based on an elegant treatment involving an energy balance. The basic precepts of this theory are that the interfacial energy generated by the fragmentation process is balanced by the local inertial or kinetic energy of the material. The method is first applied to the dynamic fragmentation in a fluid; it is then extended to brittle solids, by incorporating fracture mechanics concepts. The general equation is developed from an expanding fluid which, at a

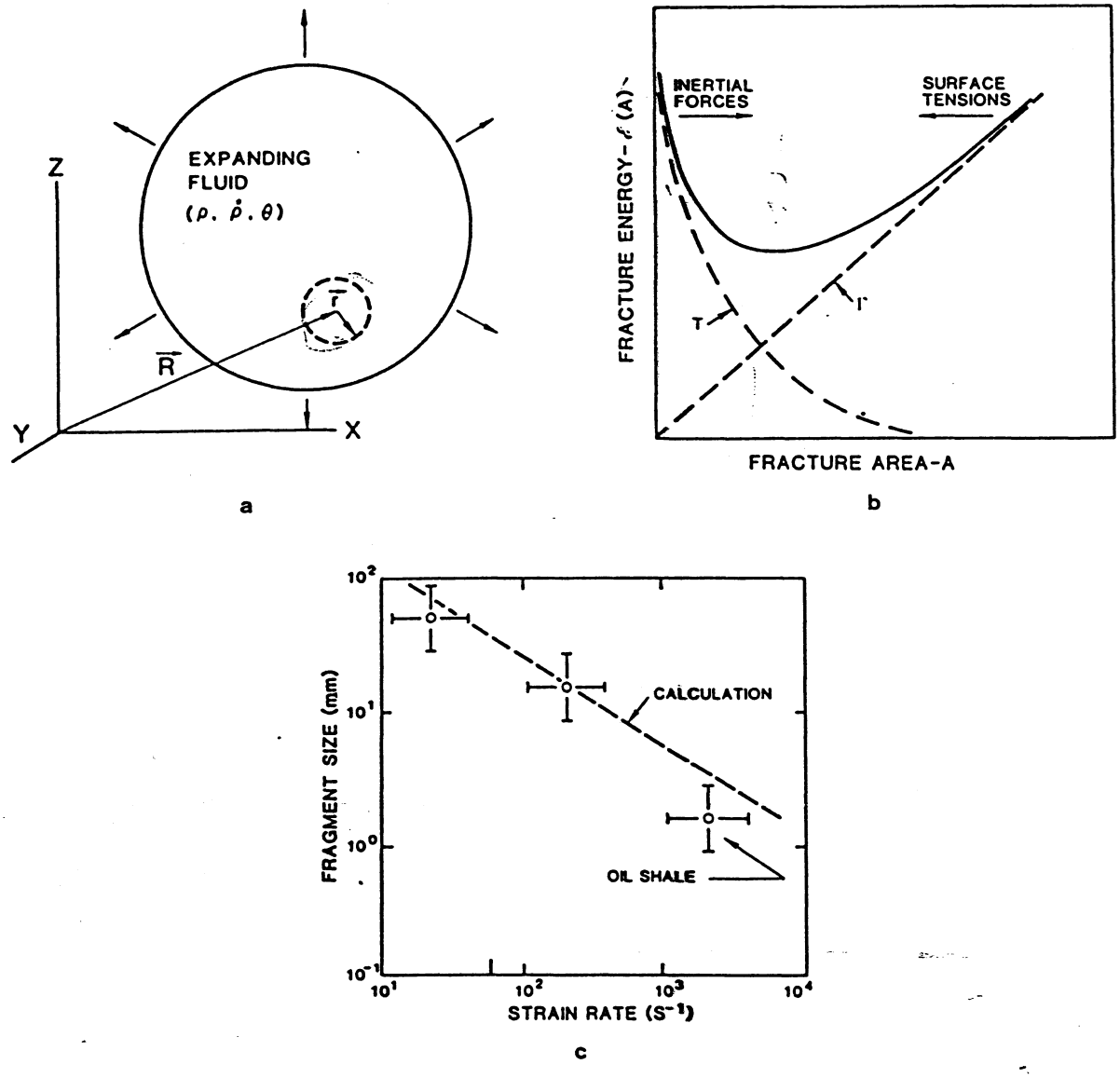

FIG. 14. Grady's theory for fragment sizes. (a) Schematic view of expanding fluid which will, at a time t, fragment. Dashed circle represents volume for which kinetic equations are applied. (b) Kinetic energy and surface energy terms; minimum establishes fracture area. (c) Application to fragment-size determination of steel. Fragment size increases with fracture toughness. (From D. E. Grady, *J. Appl. Phys.*, 53 (1982) 322, Figs 1, 2 and 4.)

time, t, has density, ρ, temperature, T, and a rate of change of density, $\dot{\rho}$. Surface tension alone resists the fracturing process. After fracturing, the fragments will fly apart at a certain velocity; this term also has a kinetic energy. Figure 14(a) shows (dashed circle) an element isolated for study. Since the fragments continue flying apart, the kinetic energy of the center of mass of each fragment is maintained and does not contribute to the generation of new surface. The component of the kinetic energy with respect to the center of mass is of importance. Figure 14(a) shows the two curves and the fragment size is determined by the minimum in the curve ($dE/dA = 0$). This corresponds to an area per fragment of

$$A = \left(\frac{3\dot{\rho}^2}{5\rho\gamma}\right)^{1/3} \tag{6}$$

where γ is the surface energy. Assuming spherical fragments of equal size, the fragment diameter, d, is

$$d = \frac{6}{A}. \tag{7}$$

Hence,

$$d = 6\left(\frac{5\rho\gamma}{6\dot{\rho}^2}\right)^{1/3} \tag{8}$$

For solids, elastic stored energy has to be considered; the equation linking fracture mechanics to the surface tensions is

$$\gamma = \frac{K_{IC}^2}{2\rho C^2} \tag{9}$$

where K_{IC} is the fracture toughness, C is the sound velocity, and ρ is the density. Substituting (9) into (10), one finds

$$d = \left[\frac{(20)^{1/2}K_{IC}}{\rho C\dot{\epsilon}}\right]^{2/3}. \tag{10}$$

Figure 14(c) shows the comparison of calculated and measured fragment sizes for high-strength steel cylinders (FS-01 steel) with varying fracture toughnesses. A reasonable agreement is found. One should, however, notice that some important factors are neglected in Grady's analysis. First, there is a considerable amount of plastic work at the crack tip; the corresponding energy could surpass the surface energy. Second, the dynamic fracture toughness is, for steels, substantially different from the quasi-static one. And third, the density of fracture nucleation sites necessarily plays an important role in establishing the final fragment size. Nevertheless, Grady's approach shows considerable promise.

Grady's treatment could be rendered more general by incorporating the crack-tip plasticity into the computations. Hertzberg[68] explains this in greater detail. An "effective" crack length is calculated by incorporating some fraction of the plastic deformation zone ahead of the crack. For plane strain, the plastic zone radius, r_y, has been estimated to be equal to:

$$r_y = \frac{1}{6\pi}\frac{K^2}{\sigma_{ys}^2} \tag{11}$$

where σ_{ys} is the yield stress and K is the stress-intensity factor. The effective stress-intensity factor is found by increasing the crack length, a, by r_y:

$$K_{\text{eff}} = \sigma[\pi(a + r_y)]^{1/2} \tag{12}$$

Substituting equation (11) into equation (12), one finds the K_{eff}. Since fracture occurs, at the highest stress, when σ equals σ_{ys}, one finds $K_{\text{eff}} = 1.41\,K_{IC}$. Consequently, equation (10) becomes:

$$d = \left[\frac{(20)^{1/2}K_{\text{eff}}}{\rho C\dot{\epsilon}}\right]^{2/3} = \left[\frac{6.3K_{IC}}{\rho C\dot{\epsilon}}\right]^{2/3} \tag{13}$$

Equation (13) expresses the fact that part of the detonation energy is consumed in the formation of the plastic zone surrounding the crack.

3.4. *The Stanford Research Institute Work*

The SRI research effort in spalling, initiated in the early seventies and continued to the present date, characterizes itself by the definition and establishment of nucleation-and-growth parameters for describing the failure process. The resultant computer code, successfully used in a number of configurations, is called NAG. The systematic measurement of crack and void sizes and orientations after different degrees of spalling was used to establish the nucleation and growth equations. The concept of damage function introduced by Tuler and Butcher[64] and Gilman and Tuler[63] was used by Barbee *et al.*[34] after careful determination of void and crack sizes. Figure 15(a) shows the cumulative number of voids with radius larger than R at various sections parallel to the free surface of the specimen (1145 aluminum alloy). Hence, $N(R) > R_1$ represents the number of voids (or cracks) per unit volume with radius larger than a certain value R_1. The SRI group developed techniques for measuring the cracks and for transforming the apparent crack orientations, length, and numbers observed in a polished surface to true orientations, length, and numbers.[42] These metallographic calculations are of great importance in the development of quantitative parameters (and laws) describing the damage accumulation process. The techniques developed in quantitative metallography[65] are of great use in these transformations. Figure 15(b) shows the distribution of cracks in Armco iron at various distances (zones) from the back surface of the target.

In their work, Curran and co-workers[33–43] developed the quantitative understanding of the rate of nucleation and the rate of growth of microcracks and voids from the systematic collection and processing of data for a number of materials. They found that the equations that describe the rate of nucleation $\dot{N}$ and the rate of growth $\dot{R}$ (time change of radius R) are:

$$\dot{N} = \dot{N}_0 \exp\left[(\sigma - \sigma_{no})/\sigma_1\right] \tag{14}$$

$$\dot{R} = \left(\frac{\sigma - \sigma_{go}}{4\eta}\right) R \tag{15}$$

where $\dot{N}_0$ is the threshold nucleation rate, σ_{no} is the tensile threshold stress, σ_1 is the stress sensitivity for nucleation, σ_{go} is the threshold stress for growth and η is the viscosity of the medium. The equation for the nucleation rate is derived from earlier results by Zhurkov,[66] who considered it as a statistical process. The viscosity term, η, represents the crack-tip viscosity for cracks. Further attention will be paid to the growth rate in Section 3.5, but it is generally accepted that the limiting growth rate for cracks is the Raleigh wave velocity. Equation (14) expresses the fact that below σ_{no}, no nucleation is observed; above the threshold stress the nucleation rate increases exponentially with the tensile stress σ. Equation (15) states that the growth rate $\dot{R}$ is proportional to the radius R of a void (or crack); for cracks, this proportionality would break down as the Raleigh wave speed is approached. The damage produced by spalling can be more simply described than in the plots of Fig. 15, if one just considers the void density (number of voids per unit volume) or the relative void volume. In this case, the void size is neglected. It can be shown that for the case of spherical voids the relative void volume is given by:

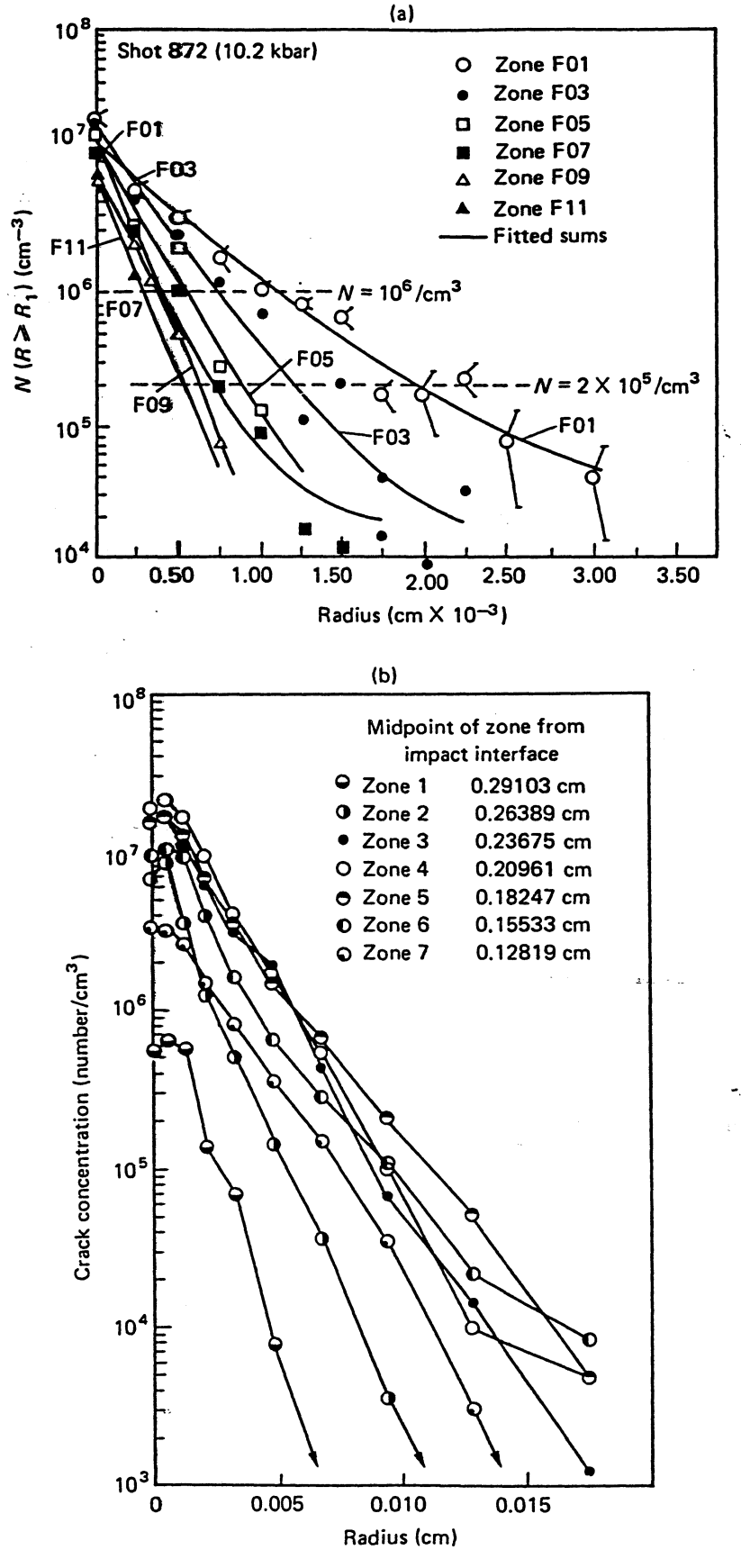

FIG. 15. (a) Volume distribution of voids in 11145 aluminum. (b) Volume distribution of cracks in Armco iron. (From T. W. Barbee, Jr., L. Seaman, R. Crewdson and D. Curran, *J. Mater.* 7 (1982) 393, Figs. 8 and 9.)

$$V_v = \frac{8\pi \dot{N} R_0^3}{3[(\sigma - \sigma_{go})/4\mu]} \left[\exp\left(\frac{3(\sigma - \sigma_{go})t}{4\eta} \right) - 1 \right] \tag{16}$$

where R_0 is the smallest visible void radius; Barbee *et al.*[34] assume it to be equal to 1 μm. Once the parameters above are determined, it is possible, by inserting the nucleation and growth equations into one and two-dimensional Lagrangian (or Eulerian) codes, to obtain realistic predictions of the relative void volumes and void concentrations as a function of distance from the back surface. Seaman *et al.*[38] describe how these models were incorporated onto subroutines; the NAG-FRAG code was developed by SRI for this purpose. Figure 16 shows the distribution of voids (both density and relative volume) obtained by the use of the code, compared with experimental results, for S-200 beryllium. The spall plane corresponds, as expected, to the region of maximum damage and the agreement between calculated and measured relative void volume and void concentration is excellent. The calculations take into account the change of bulk modulus and yield stress with the distension produced by the damage. There is also an important effect of stress relaxation as the cracks grow and coalesce. Figure 17 shows the variation of stress with nucleation, growth, and coalescence of cracks, and final fragmentation, as a specimen of Armco iron is extended at a constant strain rate of $1.5 \times 10^5\ s^{-1}$. One can see that the stress peaks at a value of 4.5 GPa and then starts to decay. In an analogous way, the stress in the spall regions, peaks and then relaxes itself as the process of damage progresses. The NAG-FRAG model of SRI

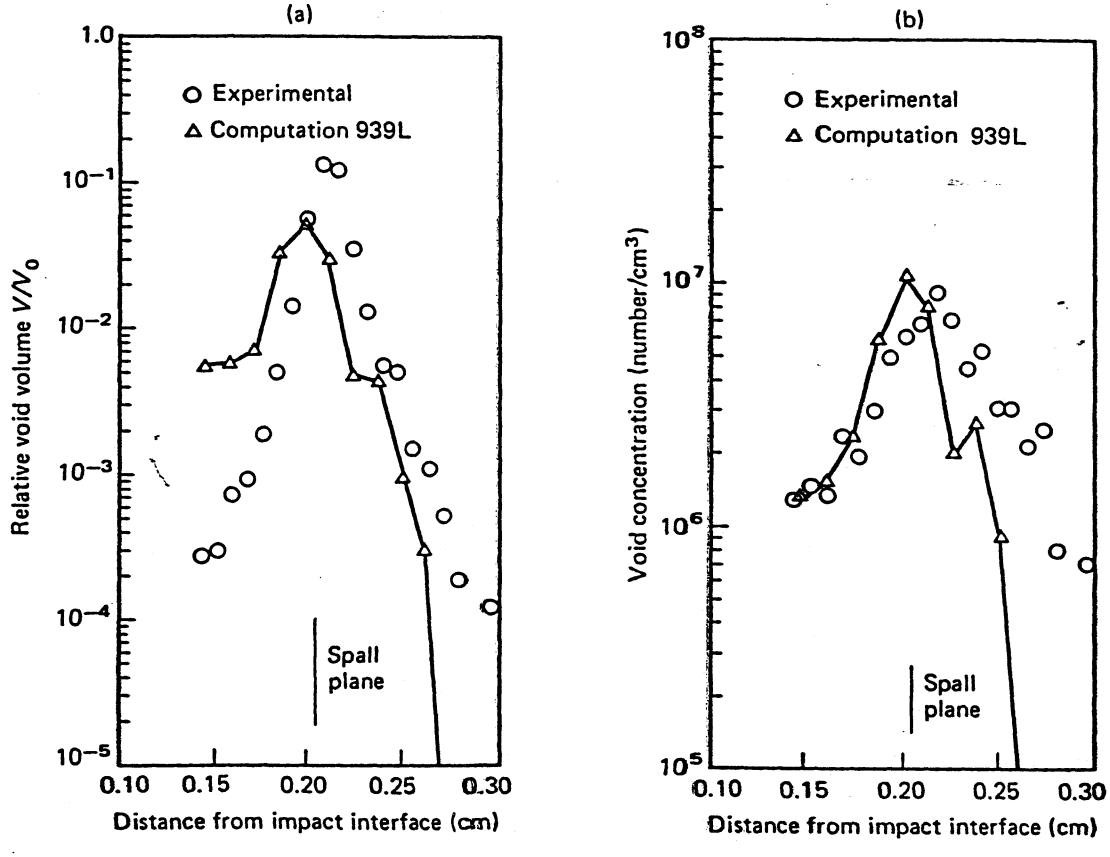

FIG. 16. Calculated (NAG code) and measured fracture damage as a function of distance from free surface for S-200 beryllium impacted by electron-beam irradiation. (From L. Seaman, D. R. Curran and D. A. Shockey, *J. Appl. Phys.* 47 (1976) 4814, Fig. 19.) (a) Relative void volume. (b) Void concentration.

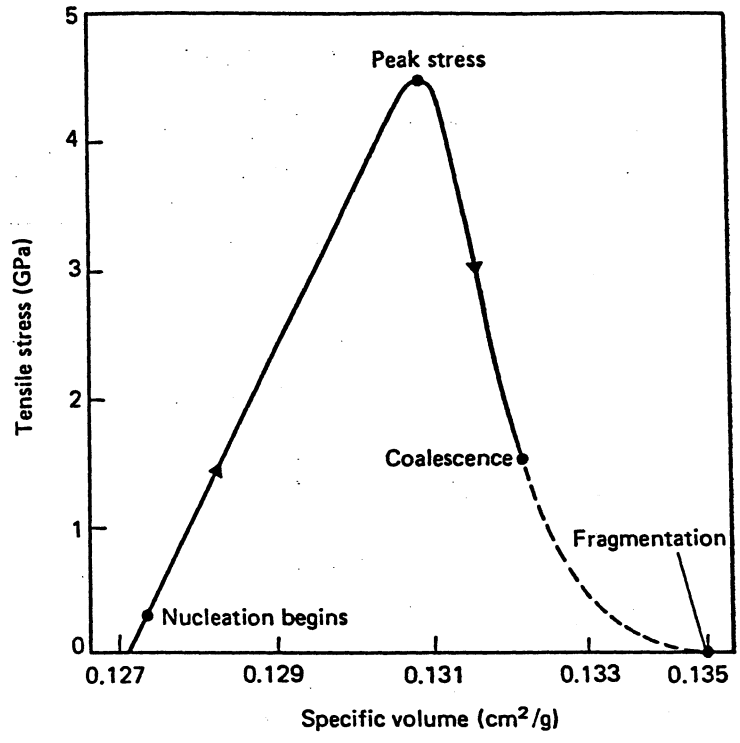

FIG. 17. Stress-volume path of Armco iron loaded to fragmentation at constant strain rate. The dashed line marks the region in which fragmentation progresses by microcrack coalescence. (From D. R. Curran, L. Seaman and D. A. Shockey, *Physics Today*, Jan. (1974) 46, Fig. 7.)

incorporates these aforementioned capabilities and Curran *et al.*[36] refer to it as being of the active type.

Curran *et al.*[36] also studied dynamic failure by spalling in polycarbonate; this model material presents the advantage of being transparent, so that the crack morphology can be clearly observed. The cracks exhibited typically several morphologies in a ring pattern, which were interpreted in terms of the different regimes of propagation. They nucleated at flaws, and moved first slowly, increasing in velocity as their size increased, up to the size determined by the equation of fracture mechanics which defines plane-strain fracture toughness, K_{IC}, for the particular crack morphology (penny-shaped crack in infinite medium):

$$R \geqslant \frac{1}{\pi}\left(\frac{K_{IC}}{\sigma}\right)^2 \tag{17}$$

This is the radius R of crack at which it propagates catastrophically; σ is the applied tensile stress. After the tensile pulse has passed, growth stops; however, the wave continues to reverberate throughout the specimen, and subsequent tensile pulses promote further growth. The same type of behavior is expected to occur in brittle metals. A sequence is shown in Fig. 18.

At the 1980 EXPLOMET conference, Curran *et al.*[43] gave a comprehensive review of the progress achieved in the understanding of spalling and placed dynamic fracture in the broader framework of fracture, emphasizing similarities and differences. Figure 19 provides a "bird's eye" view of the various ranges provided by the different experimental approaches. On the lower level of the strain rate spectrum, one has the creep tests. At increasing rates, one has tensile bars and conventional fracture mechanics tests. At yet greater strain rates,

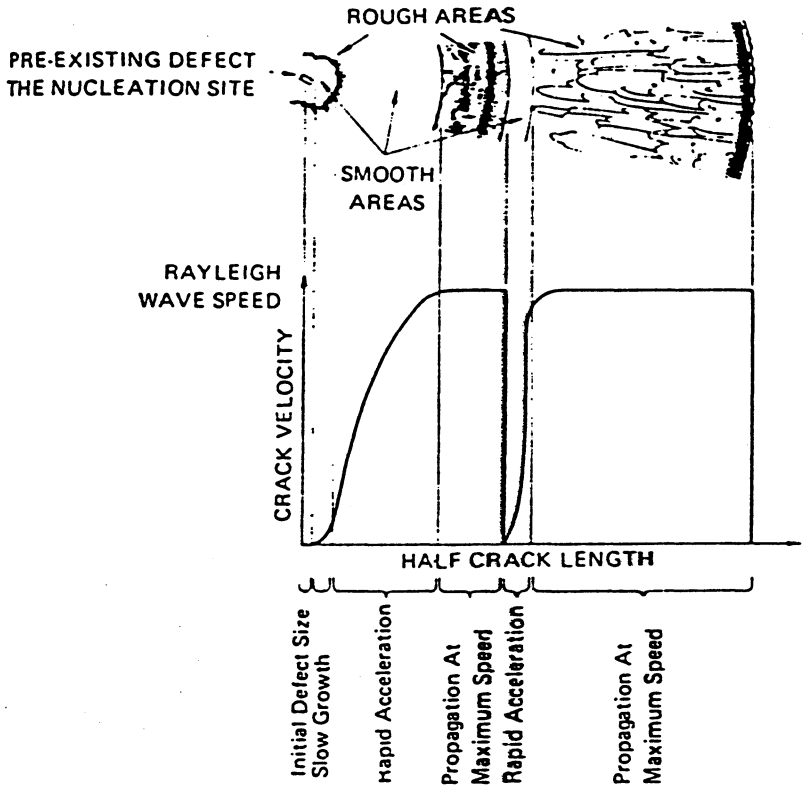

FIG. 18. Schematic illustration of change in crack morphology with growth and interpretation in terms of stress history of crack. (From D. R. Curran, D. A. Shockey and L. Seaman, *J. Appl. Phys.*, 44 (1973) 4025, Fig. 21.)

the Hopkinson bar (both in tension and torsion); the plate impact tests are characterized by strain rates of the order of $10^6\ s^{-1}$ and little residual deformation. In the exploding cylinder tests, on the other hand, the fracture may be preceded by substantial plastic strain. Poker seems to be a slow and stressful process. Curran *et al.*[43] then proceeded to analyze the mechanisms of nucleation, growth, and coalescence of microflaws for the various modes of deformation. They compare the equation for the nucleation rate (equation 14), with an equation derived by Raj and Ashby[67] for much lower strain rates. Starting from some more fundamental hypotheses, they propose the following equation for the nucleation rate:

$$\dot{N} = \left.\frac{\partial N_i}{\partial t}\right|_{\underline{x}} = \underset{\text{I}}{A(\sigma_m, T)} + \underset{\text{II}}{B(\sigma_m)\dot{\sigma}_m} + \underset{\text{III}}{C(\epsilon_i^p)\dot{\epsilon}_i^p} \tag{18}$$

where $\underline{x}$ is a Lagrangrian (material) coordinate, σ_m is equal to $1/3(\sigma_{11} + \sigma_{22} + \sigma_{33})$ and is the hydrostatic stress, ϵ_i^p is the plastic strain tensor, $\dot{\sigma}_m$ and $\dot{\epsilon}_i^p$ are the mean stress rate and plastic strain rate, respectively. The first term (I) $[A(\sigma_m, T)]$ describes nucleation under constant stress as a result of a thermally-activated mechanism; it is the nucleation rate of Raj and Ashby's[67] theory. Diffusional processes are the mode of forming the void nucleus according to this mechanism, and Eyring's theory of thermally-activated processes provides the fundamental assumptions in the derivation. The second term (II) $[B(\sigma_m)\dot{\sigma}_m]$ describes nucleation arising from debonding at second-phase particles as the stress progressively increases. The third term (III) $[C(\epsilon_i^p)\dot{\epsilon}_i^p]$ describes the nucleation by debonding due to plastic strain accumulation. Preferred nucleation sites will be described in Section 4. In steels, a

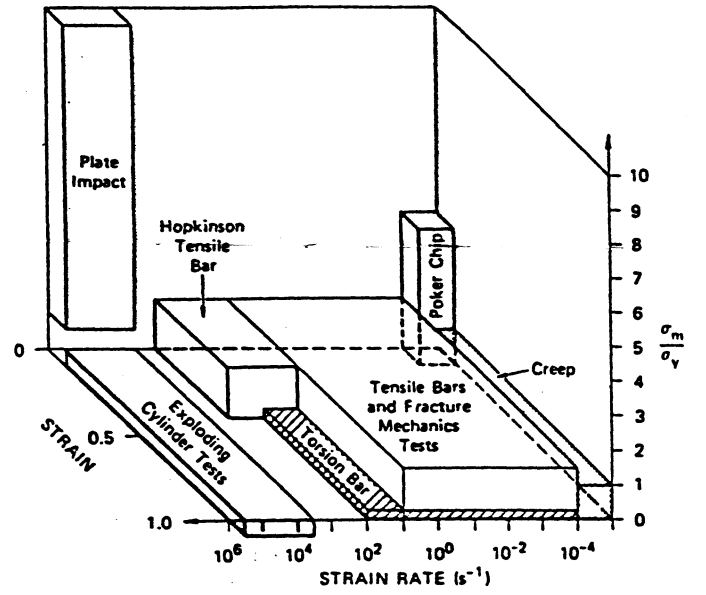

FIG. 19. Regions of stress, strain, and strain rate attained by various mechanical tests according to Curran, Seaman, and Shockey. (From D. R. Curran, L. Seaman, and D. A. Shockey, in: *Shock Waves and High-Strain-Rate Phenomena in Metals*, eds. M. A. Meyers and L. E. Murr, Plenum, NY (1981) p. 132, Fig. 18.)

large number of cracks are found to nucleate at particle–matrix interface. Indeed, this is the case in both high- and low-strain rate deformation. Hertzberg[68] presents statistical data for steel and shows that cracks are much more likely to occur at embrittled grain boundaries and brittle second-phase particles than as a result of twin and/or slip interactions. Almost every microcrack found in 0.035%C and 0.005%C steels could be traced to the fracture of a carbide particle.

Curran *et al.*[43] proceed by assuming threshold nucleation stress and strain as a function of inclusion size. They arrive at a general expression for the nucleation of cracks incorporating the three aforementioned mechanisms (diffusion-controlled vacancy migration, debonding of inclusions produced by stresses, and debonding produced by plastic strain).

Continuing their quest to provide a fundamental background for the empirical equations describing nucleation and growth, Curran *et al.*[43] described growth as composed of a diffusive and a plastic component. The diffusive growth is the principal mechanism of void growth at high temperatures and low stresses, and is treated by Raj and Ashby.[67] Plastic expansion of a void by movement of dislocations is also considered in a preliminary way; this topic is discussed again in Section 3.6. At dynamic loading rates, viscous and inertial effects become important, and the temperature rise due to the frictional processes involved in plastic deformation might have an important contribution. However, the state of development of the theory is not at a point, at the present moment, at which one can distinguish between the various possible mechanisms by comparison with experimentally-observed growth kinetics.

Third stage in fragmentation, which is coalescence of cracks and voids, is also discussed by Curran *et al.*[43] They refer to the approach of McClintock[69] for ductile failure in which coalescence of elliptical voids is caused by their impingement. The impingement of voids takes place when the relative void volume is between 50 and 60%. However, other researchers have conducted more detailed analyses showing that the structure becomes unstable prior to impingement. Unstable regions form between the voids; they are the

equivalent of necks in a tensile test. For brittle crack propagation, impingement is the *de facto* criterion for coalescence. Although little is known, at the present moment, on the exact mechanisms of coalescence, a model has been proposed recently by Shockey *et al.*[101] for the fragmentation of rocks.

3.5. *Other Efforts*

Spalling research has not restricted itself entirely to Sandia and SRI. Wilkins[70] of Lawrence Livermore National Laboratory, a pioneer in the development of computer codes in the simulation of dynamic phenomena, presents a description of the effect of material strength on spalling. De Rosset[48] of the Ballistic Research Laboratories simulates void coalescence during dynamic fracture by a computer code and compares the predictions with results obtained for aluminum that underwent incipient spalling. He concludes that interactions (coupling) between the nucleation and growth caused by the coalescence of voids is a complicating factor not considered in the early SRI work and proposed a modified expression. Greenhut and co-workers[54,55] of Rutgers University, investigated substructural changes produced in spalling; their work is discussed in greater detail in Section 4. Jones and co-workers[51–53] subjected a number of hollow cylinders of aluminum alloys (2024 and 6061) to internal detonations and observed the spalling produced close to the external wall. The damage observed depended upon the heat treatment undergone by the specimens (for more details see section 4). Takahashi[45] at the University of Tokyo, Japan, studied the spalling characteristics of polymethyl methacrylate; the transparency of the polymer lends itself very well to crack nucleation and morphology studies. This study is similar in nature to the one conducted by Curran *et al.*[36] Johnson[22] at Los Alamos, conducted a theoretical analysis of the development of voids produced by spalling and applied it to computer codes. His basic approach was to use the theoretical model of void collapse in a porous ductile material under pressure developed by Caroll and Holt,[71] and inverting the stress sign in such a way that void collapse is replaced by void growth. The changes in properties with distension are incorporated into the model, as well as the material resistance to void growth. Figure 20 shows the comparison of measured and predicted relative void volume (porosity) for a copper target (1.6 mm thick) impacted by a copper projectile (0.6 mm thick) at a velocity of 0.16 mm/μs, providing an initial pressure of 3 GPa. Up to 30% porosity is observed in the spall plane, and the calculated and observed results show good agreement. It should be noticed that there are a number of input parameters in the computer code; they have to be adjusted to provide a good fit and some of them (the viscosity, η, for instance) cannot be independently obtained.

Maron and Blaugrund[46] of the Weizmann Institute of Science in Israel recently reported measurements of free-surface velocity in the back surface of specimens of copper and aluminum during spalling. A technique involving microwave interferometry was used and apparent discrepancies were found between the tensile stresses calculated from the free-velocity measurements and those predicted by extrapolating the Hugoniot equation of state (developed for compressive stresses) to the tensile regime. However, the photomicrographs shown in their publication indicate that the inclusion content of both copper and aluminum is extremely high, undoubtedly affecting the spalling mechanism and producing a relaxation of the stresses by debonding at the inclusions. Their results would have to be validated by repeating the experiments for high-purity copper and aluminum.

Dormeval *et al.*[47] report some recent developments in the technique to produce dynamic failure. The loading rates achieved by a conventional Charpy test are of the order of

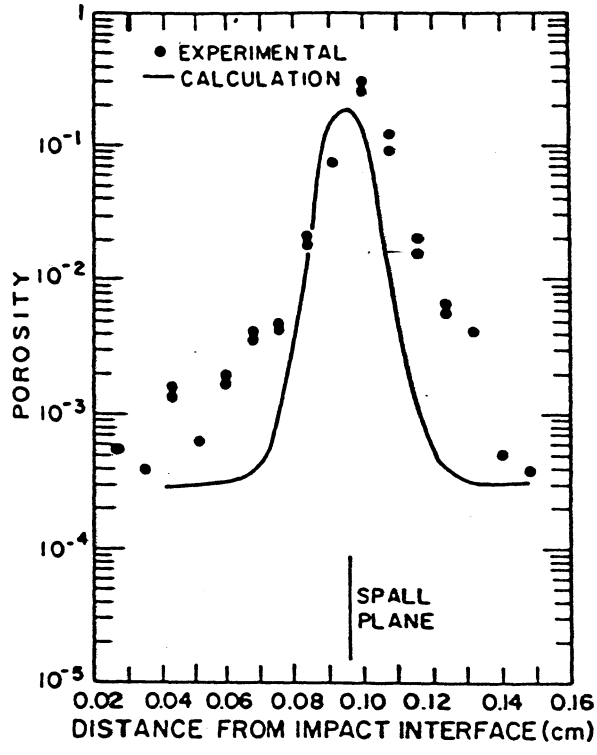

FIG. 20. Comparison of calculated (solid line) and measured (data points—SRI) post impact porosity for a copper sample. (From J. N. Johnson, *J. Appl. Phys.* 52 (1981) 2812, Fig. 8.)

10^5 MPa $m^{\frac{1}{2}}$ s^{-1}. Dormeval *et al.*[47] modified a machine developed by Costin *et al.*;[72] this machine is essentially a Kolsky bar (second generation Hopkinson bar) modified to carry a tensile specimen of cylindrical shape with a notch. The elastic tensile pulse traveling though the specimen produces the failure at the notched region because of the stress concentration. This machine allows loading rates of the order of 10^6–10^8 MPa $m^{\frac{1}{2}}$ s^{-1} and is well suited for the determination of dynamic fracture parameters, such as K_{IC} and J. Dormeval *et al.*[47] obtained dynamic fracture toughness values for a high strength steel. The dynamic K_{IC} was found to be higher than the static one by about 25%; this result is in line with other experimental studies. However, low-carbon steels have a lower dynamic fracture toughness than the quasistatic one. These steels undergo a ductile-to-brittle transition when the strain rate is increased, with the associated decrease in toughness. It is well known that brittle fractures require less energy to propagate than ductile ones, because the work required for plastic deformation at the regions adjoining the microflaws is much lower.

There is undoubtedly a considerable body of work published in the USSR, and unknown to the authors.

3.6. *Dynamics of Crack and Void Growth*

The velocity at which cracks and voids can grow determines the rate at which a spall can form. A number of experimental and analytical studies have been conducted on the stress-dependency of crack and void-growth velocity; some of these studies are discussed in Sections 3.6.1 and 3.6.2. One should recognize an important fact when studying the growth velocity in spalling: there is a great number of individual nucleation and growth events, and as the cracks/voids coalesce, one might obtain an apparent growth velocity that greatly

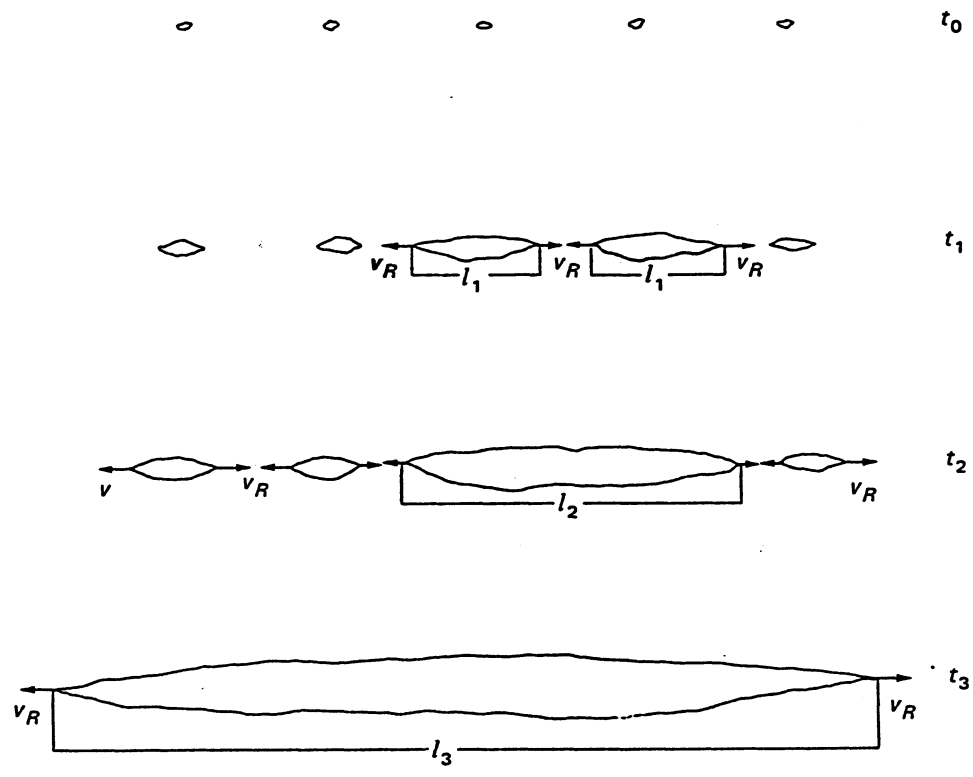

FIG. 21. Apparent and real crack-growth velocity.

exceeds the actual velocity. On the other hand, in conventional fracture one usually has the propagation of one crack whose tip is well defined. Figure 21 shows how the independent nucleation from four different flaws leads to an increased apparent velocity. At t_1, the four flaws have given origin to four cracks with tips growing at velocities v_R. When, at t_2, two cracks coalesce, two cracks with length l_1 become one crack with length l_2. Although the tips are still moving at v_R, the coalesced crack showed, at the coalescence moment, a large increase in velocity due to the instantaneous doubling of the crack length. As this process repeats itself, one might obtain an apparent crack velocity which exceeds the real velocity by a large extent. Hence, at t_3 the crack has reached a length of l_3 by combined nucleation, growth and coalescence.

3.6.1. *Crack growth*

It is generally accepted that the limiting velocity for the growth of a crack in a brittle material is the Raleigh wave velocity (Raleigh, or Love waves are surface waves which propagate at a velocity slightly inferior to the velocity of shear or equivoluminal waves in the bulk). Figure 22 shows the ratio of the energy release rate at a velocity $C(G_1)$, and the energy release rate at rest (G_1^*) for a crack of constant length travelling in an infinite material under a mode I displacement. This treatment, developed by Yoffé,[73] is presented by Sih.[74] The energy release rate represents the force required to extend the crack at a given rate. Yoffé[73] determines the ratio G_1/G_1^* for plane strain:

$$\frac{G_1}{G_1^*} = \frac{S_1(1 - S_2^2)}{[4S_1S_2 - (1 + S_2^2)^2]} \tag{19}$$

where

$$S_j = \left[1 - \left(\frac{C}{C_j}\right)^2\right]^{1/2}, \qquad j = 1, 2 \tag{20}$$

C_1 and C_2 are the longitudinal and shear wave velocities, respectively, and S_1 and S_2 are parameters relating shock and particle velocities. One can see from Fig. 22, which represents a plot of equation (19) for three different values of Poissons Ratio, ν, that the energy release rate approaches infinity as the wave velocity approaches the shear wave velocity. For $\nu = 0.25$, the limit of infinity is reached at a value of C equal to 0.92 C_2. This corresponds to the Raleigh wave velocity. More realistic crack configurations have also been studied and the same limit is obtained. It is implicit in the above development that one has a supercritical crack, i.e. that the stress is such that the critical crack radius, r_c, is exceeded. The equation below gives the critical crack size at a certain stress level and for a certain value of the plane strain fracture toughness for a centrally located penny-shaped crack in plane strain.

$$r_c = \frac{K_{IC}^2}{\pi \sigma_y^2} \tag{21}$$

Paxson and Lucas[76] describe some of the work done on the determination of upper limit for crack growth; experimental measurements of the ratio C/C_1 for glass, fused quartz, steel, and cellulose range from 0.2 for steel to 0.42 for fused quartz. Paxson and Lucas[76] determined the maximum crack velocity for polymethyl methacrylate (plexyglass) and found it to be equal to 0.36 C_1. Broberg[77] conducted a detailed theoretical analysis of the region around the crack tip and pointed out that material instability occurs in that region, imply-

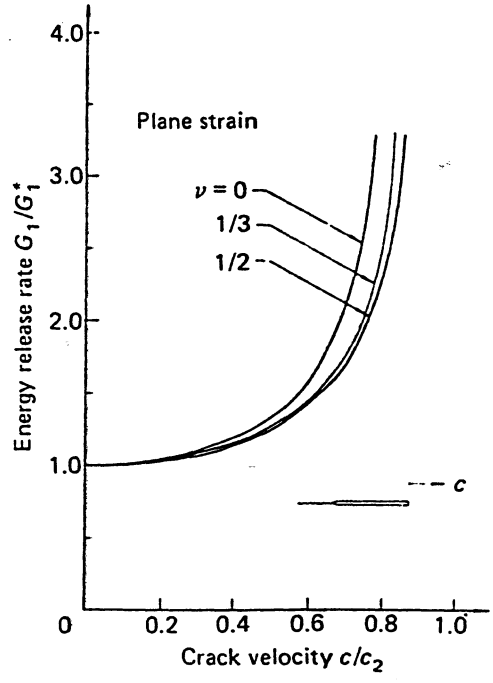

FIG. 22. Energy release rate as a function of crack velocity for a fixed length crack according to Yoffe's calculations. (From G. C. Sih, in: *Inelastic Behavior of Solids*, eds. M. F. Kanninen, W. F. Adler, A. R. Rosenfield and R. I. Jaffee, McGraw-Hill (1970) p. 607, Fig. 3.)

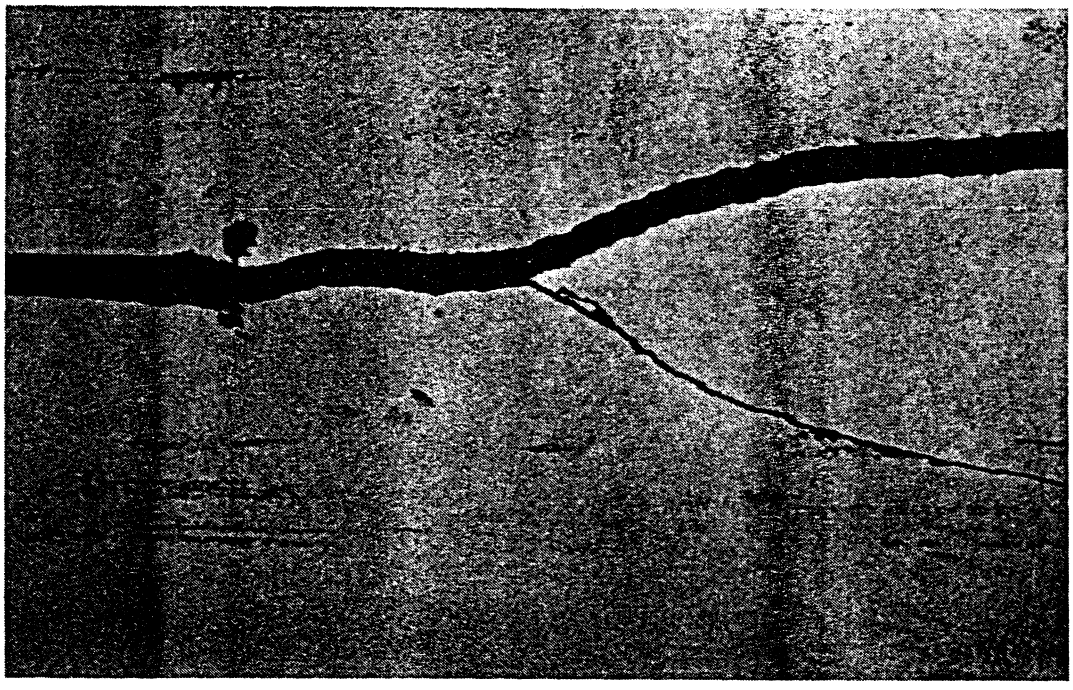

FIG. 23. Crack bifurcation in mild steel fractured at −60°C. (From J. Congleton, "Practical Applications of Crack-Branching Measurements", in: *Dynamic Crack Propagation*, ed. G. C. Sih, Noordhoff, Leyden (1978) p. 427, Fig. 4.)

ing that the sound velocities of the material are approaching zero in the continuum outside the region of material instability. For the elasto-plastic deformation case, the sound velocity is reduced in the region of plastic deformation adjoining the crack. The effect of these alterations of sound velocities on the propagation characteristics of cracks is discussed.

While an isolated crack might approach the theoretical limit when the driving energy is sufficient, another phenomenon, crack bifurcation or branching, interferes with it. Figure 23 shows the bifurcation of a crack in mild steel deformed at −60°C. Congleton[78] discusses the critical conditions for crack branching; both crack velocity and the stress-intensity factor have been claimed as the reason for branching. The redistribution of the stresses around the crack induced by branching seems to be of critical importance and the reduction of the overall stored energy or energy release rate seems to be the driving energy. Congleton[78] states that the high crack velocity is a necessary but not sufficient condition for branching and that there is a critical stress intensity factor, K_B, above which branching is observed. Branching occurs most readily in very brittle solids; hence the range of alloys exhibiting this behavior is fairly limited. Branching affects fragmentation and should be an important consideration in fundamental models describing the size distribution of fragments. Sih[74] states that the maximum crack velocity (C_R) is never attained; in practice bifurcation occurs and the velocity is limited to $\sim 0.7\, C_R$.

A unique experiment conducted by Winkler, Shockey and Curran[79,80] and yielding supersonic crack velocities is described next. Laser irradiation of a KCl crystal was conducted in such a way that the laser beam focussed in the center of the crystal; a plasma (10^6 K) was induced in the center of the specimen, driving the cracks that formed at velocities between 10^4 and 10^5 m s^{-1}. Photographs taken 80 ns after the irradiation revealed cracks of a length yielding the velocities above. The explanation provided by Curran *et al.*[80] for this unique phenomenon can be readily understood by referring to Fig. 24. Figure 24(a) shows a wedge pushed subsonically into a crack. Since the wedge velocity is lower

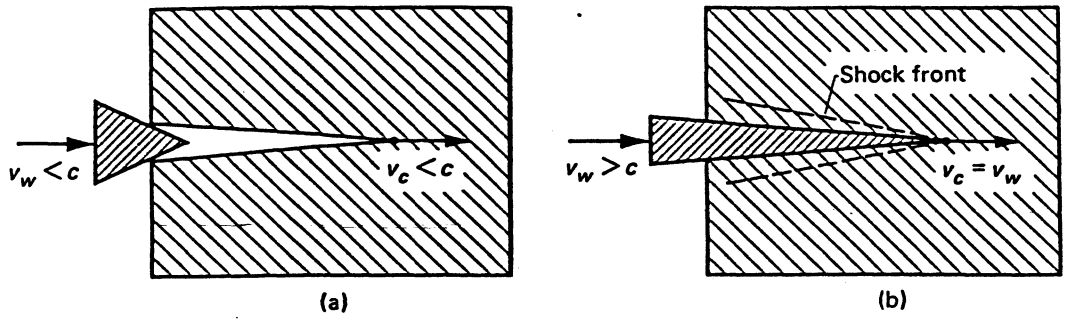

FIG. 24. Schematic explanation of propagation of crack driven by (a) subsonic wedge and (b) supersonic plasma. (From D. R. Curran, D. A. Shockey and S. Winkler, *Int. J. of Fract. Mech.* 6 (1970) 271, Fig. 1.)

than the sound velocity, the elastic waves preceding the wedge create elastic stress fields which provide energy to the crack; the maximum crack velocity simply is given by the rate at which the stress field can deliver energy to the crack tip. It is equal to C_R. On the other hand, the wedge of Fig. 24(b) is pushed supersonically into the crystal; the energy is transferred directly from the wedge to the crack tip.

3.6.2. *Void growth*

Ductile metals fail, both quasi-statically and dynamically, by void nucleation, growth, and coalescence. There is a greater similarity in this case between quasi-static tensile failure and spalling, because in both cases the number of voids is large and necking between the voids produces coalescence.

The quasi-static growth of voids has been treated theoretically by McClintock,[81,82] Rice and Tracey,[83] and Needleman.[84] Knott[85] reviews McClintock's[81,82] and Rice and Tracey's[83] treatments. McClintock[81,82] assumed cylindrical voids subjected to a plane strain situation. The radial expansion of these cylinders leads to their eventual coalescence. McClintock's calculations were compared with results in plasticine and revealed a very strong inverse dependence of fracture strain on tensile stress transverse to the holes. The presence of transverse strains of a tensile nature drastically decreases the ductility of the material. This phenomenon is of importance to spalling, where the uniaxial strain condition establishes strong transverse tensile stresses in the spall region. One should expect very little plastic deformation, which is actually observed. The fracture strain in spalling is invariably low.

Needleman[84] has taken the analysis of void growth one step further by considering the interaction between the stress fields of voids. He considered a doubly periodic array of parallel cylindrical voids and, using the variational method, estimated the changes in void shape and size with increasing overall strain; he was also able to follow the development of the plastic zone around a void. Figure 25 shows the development of the plastic zone around a void; the void interaction is considered because the void is surrounded by other voids, as shown in Fig. 25(b). The void elongates in the direction of the applied load; the plastic deformation starts close to the diametral part of the void and proceeds until it links up with plastic deformation from adjoining voids. It is important to understand this process in order to develop a microscopic understanding of the process of spalling by ductile void growth and coalescence. As the space between two adjacent voids is decreased, the metal will neck, leading to coalescence.

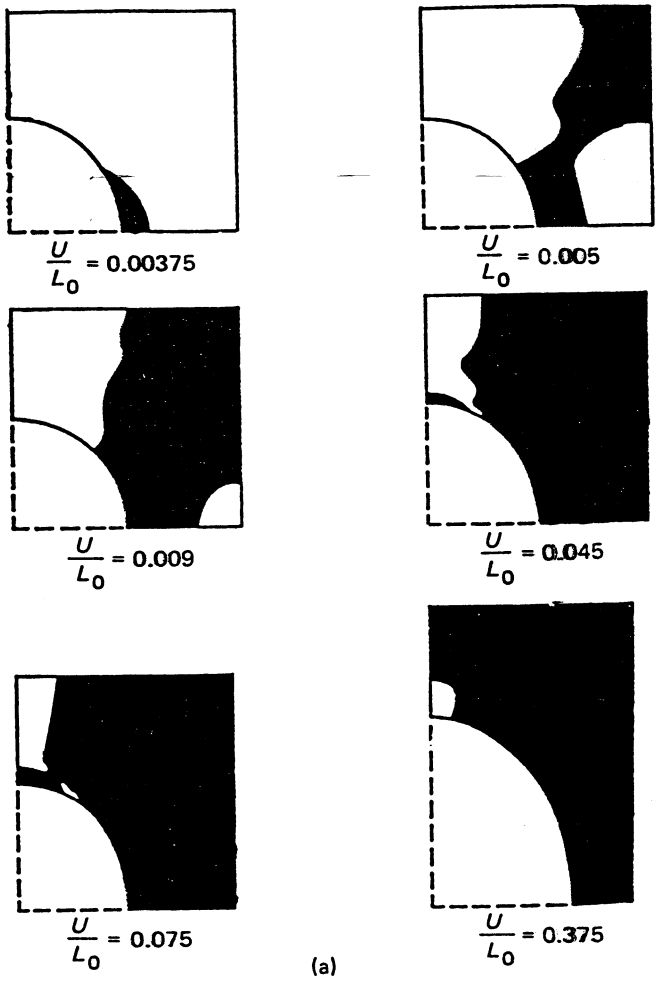

FIG. 25. (a) Growth of plastic zone (black region) around a void under increasing strain. (b) Doubly periodic array of voids. (From A. Needleman, *J. Appl. Mech.* 39 (1972) 964, Figs 7 and 1(a), respectively.)

The initiation of voids, in quasi-static deformation, has also been the object of a number of studies. In the case of large inclusions which are not strongly bonded to the matrix, debonding produces, in effect, a void which has the size of the inclusion. MnS inclusions in steel are a typical example of a case where the bonding strength is negligible.[85] However, in some cases the stresses arising from differences in thermal expansion coefficient between the inclusion and matrix put the latter in compression and provide structural integrity to the interface. Strongly bonded particles might give origin to void growth by fracturing during deformation. The region at which the fracture impinges on the matrix is an ideal initiation site. Another mechanism by which they can act as initiation sites is through the emission of vacancy loops which may condense into voids.

The dynamic growth of a void presents some additional complications:

(a) The heat generated by plastic deformation cannot dissipate itself due to the high rate of deformation.
(b) Inertial effects associated with the displacement of the material adjoining the void walls become an important consideration.
(c) Wave interactions have a bearing on the final configuration.

Glennie[86] modified the calculations of Rice and Tracey[83] taking into account inertial effects. Experimental observations of crack propagation in ductile metals seem to show that the maximum velocity is much lower than in the case of brittle fracture; for ductile steels, the value of $275\ m\ s^{-1}$ is given by Glennie.[86] Glennie attributes this reduction in the maximum velocity to inertial effects and provides an approximate solution for the growth of voids taking into account these inertial effects.

3.7. *Computer Codes*

The nucleation, growth and coalescence of microflaws is a product of the stress state, amplitude and duration undergone by the material. Hence, the development of computer codes describing fracture is an extension of the codes describing the stress and strain in the material. This section will present a brief description of the numerical techniques used in these deformation codes. In order to envisage the complexity of dynamic deformation, one can say that there are three regimes, each with characteristic wave morphologies and velocities; in the elastic regime, one has longitudinal and and shear waves; in the plastic regime, one has longitudinal and shear plastic waves whose velocity and front configuration depend on the stress level; in the shock-wave regime, one has shock waves. A realistic code has to incorporate these features. Fracture simulation codes are usually subroutines in larger dynamic deformation codes.

A number of explicit computer codes have been developed to described non-linear material response to dynamic loading as a shock have passes through a medium. For wave propagation at low stress amplitude, elastic theory adequately describes the linear response for pressures near material yield strength, whereas elastic-plastic models incorporate yield criteria for slightly higher pressures. However, for very high pressures (high stress applied over very short durations), material is modeled like a compressible fluid for which material strength is neglected. Hydrodynamic relations are used to describe material flow to solve axially symmetric, time-dependent impact problems.

This section provides a general overview of computer codes used to model stress/strain propagation in materials subjected to shocks. Fundamental relations and assumptions used in codes are described. A comparison of selected hydrodynamic codes is presented in

addition to a summary of fracture models linked to various codes. For a complete description of mathematical treatment, the reader is directed to references cited.

3.7.1. *Fundamental relations*

For wave propagation in a continuum, the constitutive relations describing conservation of mass, momentum, and energy are integrated over time. In fluid dynamics, the equations of state describing material behavior include relations for pressure, density or specific volume, and internal energy. Many codes incorporate temperature effects from shocks and hence temperature is included. Material behavior regimes range from elastic, elastic-plastic to hydrodynamic depending on stress levels. For codes which predict dynamic tensile fracture, an appropriate yield criterion for the regime selected is specified and, in most cases, is rate dependent.

For hydrodynamic material behavior, in response to impulsive high shocks, the Hugoniot equation of state relates pressure and density for adiabatic compression under hydrostatic pressures in uniaxial strain. Shocks are treated as abrupt, but continuous transitions in flow variables.

Wave codes are written in one or two dimensions with coupled fracture models extending to a third dimension when full description of fracture orientation is desired. In one dimension, computational grid points relate a single material dimension with time (x,t), whereas, in two dimensions, material properties are calculated in two-dimensional space integrated over time (x,y,t). In the former case, both finite difference approximations and the method of characteristics[87] have been applied numerically to solve compatibility equations, whereas solutions with three independent variables are restricted to finite difference methods.

For given mesh dimensions in the finite difference method, the non-linear equations of state and constitutive relations are integrated with respect to time at each time step. The described material properties, along with displacements, velocities and accelerations are calculated for each computational grid point based on relative displacement and property values of adjacent cells.

In the method of characteristics, the finite-difference approximation is applied to the characteristic curve equations which develop from the hyperbolic wave equation, in addition to the compatibility equations. It should be noted that the method of characteristics is used when details of wave motions are desired, whereas finite difference methods apply when the ultimate state of material is to be described. A more detailed comparison of these two methods is given in Section 3.7.4.

3.7.2. *Computational schemes*

Hydrodynamic codes use either a Lagrangian, Eulerian or particle-in-cell (PIC) approach in describing motion of a fluid. Each scheme uniquely computes material motions and changes in material properties with reference to a mesh of computational grid points or interior cells. Table 3 summarizes the numerical capability of selected codes categorized by computational schemes. References are also cited.

In the Langrangian coordinate system, the grid, embedded into the material, deforms as the material responds to a shock load traveling at a non-linear rate through the material. The Langrangian system treats material interfaces and free surfaces (interior and boundary) in a straight-forward fashion. Boundary conditions specify either pressure or velocity along

Table 3. Synopsis of features of different codes

Numerical Coordinate Scheme	Code Name	Dimensional Capability	Numerical Method (1)	Material Modeled (2)	Model Treatment: Time Rate Effects	Work Hardening	Temp. Effects	Spall	Dynamic Crack and/or Void Growth	Aniso-tropic Materials	Model Features: Artificial Viscosity	Sliding Inter-faces	Grid Rezoning	Applications
Lagrangian	WONDY[88]	1-D	FD	EP HD	+	+	NA	+	cracks	NA	+	NA	+	Dynamic fracture, piezoelectricity, ferroelectricity, viscoelasticity, explosive reactions, plate impacts
	TOODY[89]	2-D	FD	EP HD	+	+	NA	+	+	+	+	+	+	
	PUFF[90]	1-D	FD	E HD	+	+	NA	NA	(4)	NA	+	NA	NA	
	HEMP[70,91]	1,2-D	FD	EP HD	+	+	+	NA	voids	NA	+	+	+	
	SWAP[70,91]	1-D	MC	EP HD	NA	+	NA	+	+	NA	NA	NA	NA	
	STEALTH*[94]	1,2 3-D	FD	E EP HD	+	+	+	NA	NA	US	+	+	+	Soil structure, interaction, cratering, impact fracture, seismic wave propagation
Eulerian	CSQII**[95]	2-D	FD	EP HD	+	NA	+	+	cracks	NA	NA	NA	NA	
General Lagrangian–Eulerian	CRALE (previously AFTON[96])	1,2-D	FD	EP HD	+	+	NE	+	cracks	limited to orthographic fracture	+	+	(3)	Crater calculations from chemical and nuclear explosions (5)
	SCRAM (adapted from SALE[97])	1,2-D	FD	HD	+	NE	+	+	+	+	+	+	(3)	Oil shale fracture, mechanical sensitivity of propellants.

(1) FD—Finite Difference; MC—Method of Characteristics
(2) E—Elastic; EP—Elastic-Plastic; HD—Hydrodynamic
(3) Only required when using code in Lagrangian system.
(4) When coupled to fracture codes.
(5) CRALE version adapted by S. Schuster, California Research and Technology, Woodland Hills (CA).
*STEALTH is an adaptation of HEMP and TOODY.
**CSQII is categorized as Eulerian, however is modified to use Lagrangian calculations during each computational cycle.
+—Model addresses topic.
NA—Not applicable or does not address.
US—User specified.
NE—Not explicity.

boundary grids. Slide-line routines handle changes of material properties and displacements when they occur at different rates on either side of the boundary. The stress history of the material is taken into account over time. This approach, however, is sensitive to highly active regions in the flow field; instabilities occur in areas of high deformation which requires frequent grid rezoning. In describing spalls, a Lagrangian system is not appropriate due to large material distortions occurring during spall cone (wedge) formation.

In a Eulerian coordinate system, grids are fixed in space and calculations follow the material which happens to be in a computational cell at a given time. Large distortions do not cause computational problems; this scheme is limited to one material type and free surfaces are not handled easily without artificial constraints on flow. Boundary conditions are imposed by fixing a "mirror image" or reflecting edge along the boundary. Eulerian coordinates are not suitable for keeping track of discontinuities and to achieve stress history accounting, a convective term must be added to equations describing material behavior. Often, tracer particles are used to keep track of discrete masses in space between events as well as to represent interfaces and free surfaces. The use of a fixed grid system is limited when describing a spallation wedge as the artificial constraints impose a false diffusion of material resulting in an inacurate description of the spall envelope.

Most Eulerian codes (e.g. CSQII) utilize Lagrangian calculations during each time step cycle, then enter an Eulerian section which automatically "rezones" mesh deformations. Grids are redefined at the positions used at the start of the Lagrangian section. If redefinition is uniform, initial conditions are inadequately described; if rezoning is non-uniform, then a poor definition of material moving into large zones occurs.

The PIC method combines features of both Lagrangian and Eulerian methods. In this case, the material consists of discrete mass particles whose positions are monitored each cycle. The material is divided into Eulerian cells which are fixed. Particles represented by a Lagrangian mesh are fluid elements which carry a cellular mass, momentum and energy for a specified time cycle as it moves through the fixed mesh. Field variables are characterized by the fixed mesh, while the particles describe the material itself. This method is ideally suited to problems of large slippage and distortion. The method does not allow for stress history but adequately describes spallation and other discontinuities.

For finite difference codes, a typical two dimensional code uses a 200 to 400 square mesh, with total material widths on the order of 5–10 cm (or Δx typically ranges from 0.25 to 4 mm). Between 9 to 40 variables are stored per cell per time cycle.

3.7.3. *Finite difference methods*

3.7.3.1. *Accuracy and stability.* Inherent to finite difference methods are the requirements of consistency or accuracy and stability which lead to added rezoning routines. In the presence of steep shock fronts in axially-loaded materials, non-linear equations become unstable. In the system of differenence equations extending from the wave equation, values of pressure and velocity as a function of time are erratic as shown in Fig. 26. The solution for pressure behind the wavefront becomes noisy as numerical oscillations persist. Therefore the shock front must be smoothed over a certain number of grids, and results in a solution similar to that shown in Fig. 26(b).

One method used to smooth high frequency oscillations is to apply "shock fitting", or a series of small steps along the steep front as shown in Fig. 27. By using the Rankine–Hugoniot jump conditions, the constitutive relations, equations of state, and Rankine–Hugoniot equations must be solved simultaneously using iterative techniques. For Lagran-

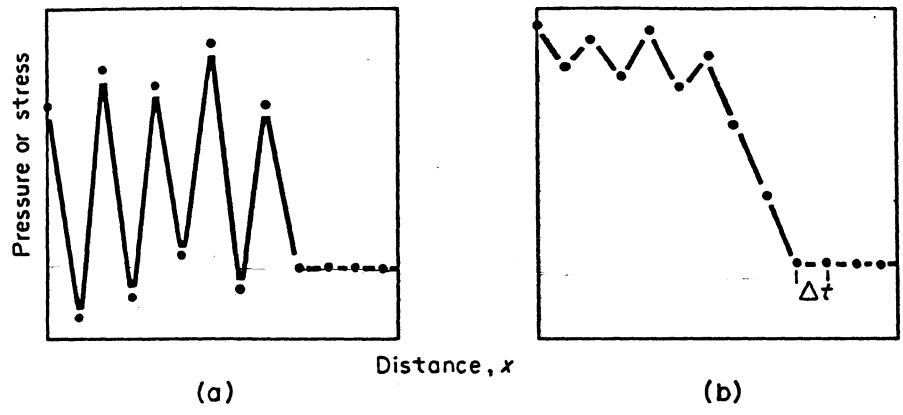

FIG. 26. Simulation of shock pulse by finite-difference technique (a) without artificial viscosity and (b) with application of artificial viscosity. (After R. T. Walsh, in: *Dynamic Response of Materials to Intense Impulsive Loading*, eds. P. C. Chou and A. K. Hoskins, AFML (1972) p. 377, Fig. 7.6 and p. 379, Fig. 7.7.)

gian or Eulerian grid systems, additional complications arise as the shock front passes each grid point in space. Therefore, "shock fitting" is limited to the method of characteristics.

For finite difference methods, the shock front is smoothed over two to three grids in the direction the wave is traveling by applying a dissipative term referred to as artificial viscosity, or the "q" term defined by von Neuman and Richtmyer.[98] The term is introduced such that the pressure term in the equations of motion and internal energy becomes

$$P' = P + q. \tag{22}$$

Depending on the magnitude of the q term (coefficient) as shown in Figure 26(b), the desired steepness of the shock front is set.

Physically, artificial viscosity is a function of cell width (Δx), wave velocity (C_1) and time increment (Δt) and therefore proportional to strain rate, controlling both growth and decay of shock waves. In most cases, artificial viscosity is applied to smooth the shock front over two to three cell widths which is approximately the characteristic length over which events occur for shocks. The artificial viscosity term is also used to account for the decay of the shock pulse as it travels through the material. This decay (also called attenuation) greatly

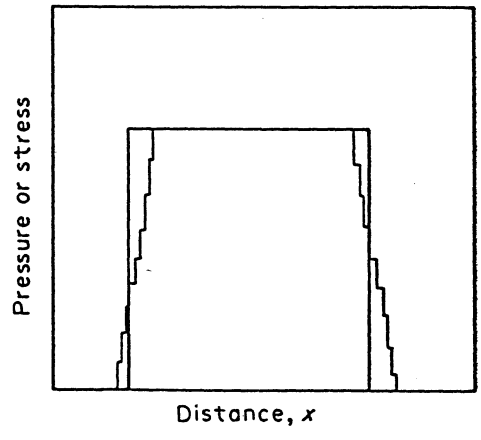

FIG. 27. Simulation of shock pulse "fitting" using step function for the method of characteristics. (After R. Karpp., in: *Dynamic Response of Materials to Intense Impulsive Loading*, eds. P. C. Chou and A. K. Hoskins, AFML (1972) p. 337, Fig. 6.26.)

exceeds the one predicted strictly from the Rankine–Hugoniot hydrodynamic treatment. Erkman and Christensen[99] and Curran[100] describe how the application of an artifical viscosity term increases the attenuation rate of a wave.

Accuracy in the solution is controlled by the Courant stability criterion which specifies that the time increment, Δt, must be selected such that changes in material properties cannot propagate faster than the propagation velocity of the shock front, or

$$\Delta t \leq \frac{\Delta x}{C_1}. \tag{23}$$

As shock waves move through materials, the Lagrangian finite difference mesh distorts, loosing uniformity throughout the material. This causes inaccuracies in computation as the mesh becomes too large in regions of inactivity while in highly active zones, Δx becomes very small, requiring excessive numbers of calculations. Furthermore, large distortions create errors in numerical values. Therefore, based on the rate of changes in physical quantities across zones, a new, undistorted mesh is created by a geometric overlay process with the old mesh. Values of the old mesh variables are computed for the grid. In the Eulerian coordinate system, most codes use a Lagrangian coordinate system for computations. Upon completion of each time cycle, automatic rezoning occurs, as the coordinate system is transformed from Lagragian back to Eulerian.

3.7.3.2. *Treatment of discontinuities.* In order to treat discontinuities and composite or anisotropic materials for two dimensional codes, slide-line routines are used. Slide-lines allow adjacent materials of dissimilar properties to deform independently. TOODY IV[89] handles two types of slide lines: (a) one where material on either side is in contact and remains in contact during deformation, and (b) a colliding and separating interface allowing two straight line segments, not co-planar, to grow together (crack or void closure) or apart as materials separate (crack growth). Mesh sizes and material properties are different on either side and a friction coefficient is specified for lines in contact.

The HEMP code[70,91] allows for a decoupling of grids along an assumed line. One side becomes a fixed boundary for one time step along which the sliding material changes position. The fixed boundary then advances in time using the force field of the adjacent sliding material. Cracking or spallation is handled by a separate routine.

3.7.4. *Alternative methods of integration and numerical schemes*

3.7.4.1. *Method of characteristics.* An alternative approach to numerically treating discontinuites is the application of the method of characteristics to non-linear problems of one-dimensional wave propagation.[87] In this method, the shock front, treated as a discontinuity, propagates along two characteristic curves resulting from the hyperbolic wave equation system. The finite difference approximation is applied to compatibility equations and to the characteristic curve equations rather than to the original partial differential equations. Dependent variables are integrated along characteristic curves at grid points formed in the mesh. Both interactions of shocks and reflection of waves from free surfaces are included. SWAP-9[93] uses this method.

The discontinuous shock front is described by the Rankine–Hugoniot jump relationships for pressure, volume and energy. This jump condition is written into the conservation laws as the continuous flow variables are modeled with a series of small shocks, as shown in Fig. 27. This reduces the number of equations traditionally needed for continuity and shock

separately, since shocks are treated explicity and the concept of artificial viscosity is not required to maintain continuous flow.

3.4.7.2. *Mixed coordinate schemes.* The AFTON code (now called CRALE) developed at Lawrence Radiation Laboratories[96] utilizes a time-dependent mesh with options for sliding interfaces. Similar to SALE[97] (now called SCRAM), the user specifies any coordinate motion (Lagrangian or Eulerian), or the space coordinates can be arbitrarily moved for continual rezoning. The CRALE codes are used to model elastic-plastic behavior in materials generally at great distances from a shock source, whereas SCRAM treats hydrodynamic behavior.

3.7.5. *Finite difference fracture models*

Coupled to one- and two-dimensional wave codes which do not treat dynamic failure[90,96,97] are finite-difference fracture models in which stress levels are compared to failure criteria. In other codes which treat fracture,[88,89] fracture models are accounting routines which statistically compute the quantity of damage or fracture or the volume of voids created within a material due to stress concentrations. These models are based on the physical theories of fracture in three distinct stages of fracture mechanisms: (1) activation of inherent or preexisting micro-flaws, (2) crack growth and development (extension of inherent flaws), and (3) coalescence of cracks or voids. Conditions for void or crack growth are specified by material properties (constitutive relations) and the induced stress field from the coupled wave code.

Linked to WONDY and TOODY (both of which incorporate strain rate effects), are routines which relate the rate of damage to stess and time. The damage parameter describes the loss in material strength which in turn adjusts the equations of state in the wave code to account for this loss. Three fracture-criterion options are available in TOODY, one of which is the BFRACT brittle fracture model developed at Stanford Research Institute. The model, incorporated in the NAG-FRAG (Nucleation and Growth-Fragmentation)[101,102] fracture routine and linked to SRI's PUFF code,[90] treats nucleation and growth of penny-shaped cracks of a given radius. Crack orientations are grouped into ranges and volumetric crack densities per cell computed for a statistical degree of fragmentation (fragments being formed by the intersection of cracks). Spallation occurs when fractures coalesce along one plane.

The hydrocodes developed at Los Alamos do not include yield criterion; however, they describe the stress field under which penny-shaped cracks grow. A generalized Griffith criterion for tensile failure is used. Two fracture models are linked to SALE, one being scalar and the other written in tensor notation. CDM (Continuum Damage Model), the scalar model, computes a damage parameter associated with cell strength loss, and stress relief due to cracking.[103,104] The tensor model, SCM (Statistical Crack Model) includes solutions for penny-shaped crack from fracture mechanics theory. Code input requires inherent crack size distributions and orientations.[103] Cracks grow in tension or shear depending on tip orientations with reference to the applied stress field. Up to eight different orientations can be described.

CAVS (Crack and Void Strain) includes a time–dependent description of codes in three-dimensions for crack lengths, orientations, width, and inter-crack spacings.[105,106] CAVS is incorporated in STEALTH codes for fracture description.

4. Metallurgical Factors

The metallurgical aspects of spalling (crack/void initiation sites, effects of parameters such as grain size and substructure, micromechanical aspects of growth and coalescence) have

Table 4. Experimental conditions for shock-loaded specimens whose microstructures are shown in this monograph

Code	Alloy	Pressure (GPa)	Pulse Duration (μs)	Technique
A	AISI 1010	10	2	*Expl. (spall plate)
B	Nickel 200	9.4	1	*Expl. (spall plate)
C	Fe-32% Ni-0.035%C	6	1.5	Gas Gun (SRI)
D	Armco Iron	2.6	0.65	Gas Gun (SRI)
E	AISI 1010	25	2	*Expl. (no spall plate)
F	AISI 1010	13	2	*Expl. (no spall plate)
G	AISI 1010	8	2	*Expl. (spall plate)
H	Copper	2	0.6	Gas Gun (SRI)
I	AISI 1020	13/26	0	Expl. (direct contact)

*Explosively-driven flyer plate producing impact.

not received the detailed attention that other deformation phenomena have. The limited research conducted in this area will be reviewed in this section; results of an exploratory investigation conducted on spalling will be interspersed with the review in Sections 4.1 and 4.2 which describe nucleation and growth, respectively. The outline of a model for void nucleation by dislocation generation and motion will be presented in Section 4.4. The shock-loading conditions for the specimens spalled by the authors (nickel, AISI 1010 steels, iron-nickel, Armco iron) are given in Table 4. The specimens are coded by letters (A, B, C, D, etc.) and they are identified by the letters in the subsequent discussion. The most complete account on metallurgical effects is the one provided by Shockey *et al.*[37] at the Albuquerque 1973 conference on metallurgical effects at high strain rates; their work is reviewed below.

The generation and propagation of spall fracture, as well as fragmentation under dynamic loading, is only partially understood metallurgically. The complexity of the situation can be assessed by analyzing Fig. 28, which shows a crack/shear-band combination produced by the impact of a spherical projectile against an armor-plate target (target in center of Fig. 1). The whole band propagating and branching is an adiabatic shear band (shear localization) phenomenon. In certain regions, the shear band has given rise to a crack; hence, it seems clear that the crack was preceded by intense shear localization, which altered the properties of the target locally. These complicating factors are not incorporated into present-day theories/models, and this section will detail metallurgical aspects of micro-flaw generation and propagation in the absence of intense shear localization; the simplest configuration is the one providing uniaxial strain.

There are essentially two modes of dynamic fracturing: brittle and ductile. Brittle fracture is characterized by cracks with sharp tips at which fracture proceeds with relatively little plastic deformation (Fig. 29a). Ductile fracture, on the other hand, is characterized by voids which, in spalling, tend to be spherical up to a certain size (Fig. 29b). BCC and HCP metals tend to spall by a brittle mode, whereas FCC metals exhibit a higher ductility at high strain rates and tend to spall in a ductile manner.

4.1. *Nucleation*

Shockey *et al.*[37] classify nucleation into homogeneous and heterogeneous. Microfracture nucleation at "submicroscopic" heterogeneities such as low-angle grain boundaries, dis-

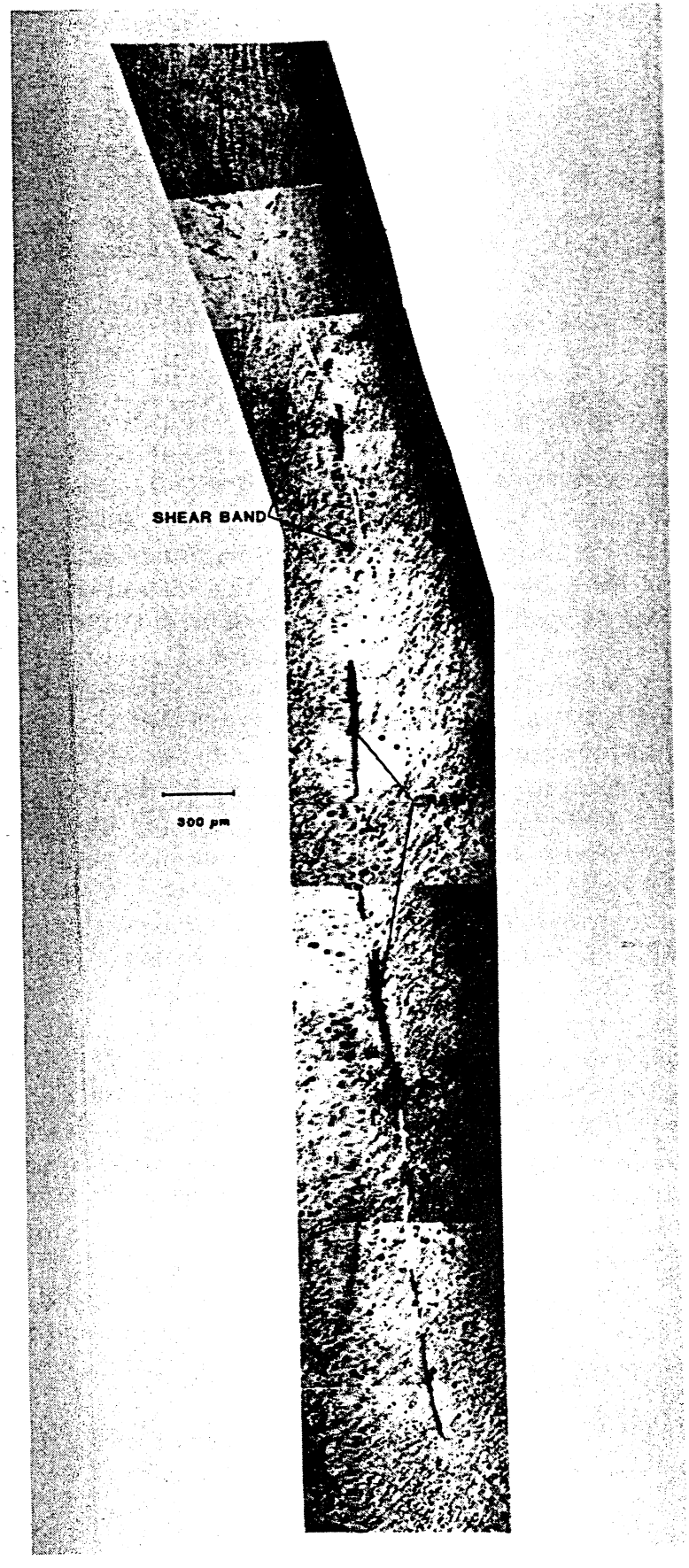

FIG. 28. Adiabatic shear band (white) and cracks along band (black) in armor plate steel (12560B) target impacted by spherical projectile; specimen shown in center of Fig. 1.

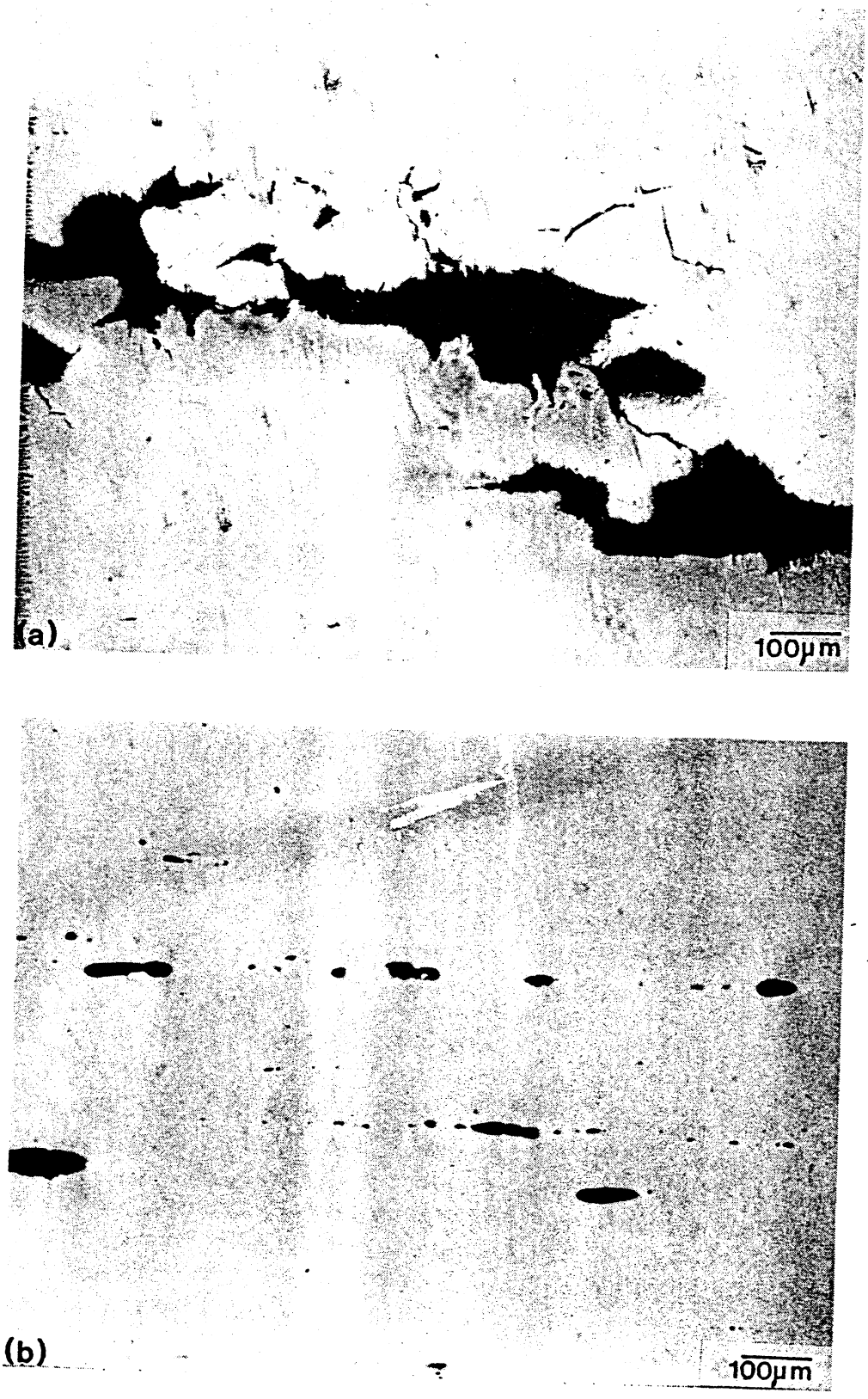

FIG. 29. (a) Spalling by brittle fracture in low-carbon steel. (b) Spalling by ductile void formation in nickel. (Spec. A and B, respectively.)

location tangles and networks, and fine impurity or precipitate particles is considered to be homogeneous. Heterogeneous nucleation sites, on the other hand, are assumed to be the ones visible by optical microscopy (at a magnification of 1000×). This classification is somewhat arbitrary, because homogeneous nucleation, *strictu sensu*, would be the one assisted only by thermal energy fluctuations. Shockey *et al.*[37] consider the following heterogeneous nucleation sites:

(a) Inclusions and second-phase particles. There are three different manners in which fracture initiation might take place.
  (i) Fracture of inclusions; the brittle inclusion, by breaking, creates a crack that operates as a stress-concentration site for the matrix.
  (ii) Separation of interfaces; when the particle is not strongly bonded to the matrix, the separation produces an effective void size that has the size of the particle.
  (iii) Fracture of the matrix; when the fracture strength of the matrix is less than that of the inclusion or interface.
(b) Fracture at grain boundaries.

The presence of a weak phase at grain boundaries favors crack initiation there. Such is the case of spalling Fe-32% Ni-0.035% C alloy discussed later. In other cases, the differences in elastic and plastic properties between adjacent grains are responsible for the establishment of stress concentrations at the grain boundaries. Murr[56] correlated the occurrence of grain-boundary ledges with spalling in molybdenum. However his TEM specimens were not subjected to a tensile pulse; the spalling Murr[56] observed was intergranular and attributed to the ledges (grain-boundary steps) and due to internal wave reflections.

Figure 30 shows four nucleation sites in spalled AISI 1010 steel. Manganese sulfide particles have a low bonding strength with the matrix, as evidenced by the separation in Fig. 30(a). Figure 30(b) shows a more advanced stage, and the cracks propagating away from the MnS particle have definitely started at the interface. A silicate particle, showing as a shark-fin-shaped protrusion in a polished section, shows clear evidence of having been responsible for the nucleation of the crack. The probable mechanism is by debonding. On the other hand, Fig. 30(d) shows that in some instances there is no direct evidence of a heterogeneous site. The spheroidal cavity was observed and similar initiation sites can be found, with no second-phase particle present. It is believed that this is an instance of homogeneous nucleation. The authors believe that both homogeneous and heterogeneous nucleation occur concurrently, if the stress is high enough. The threshold stress for heterogeneous nucleation is, of course, lower than the one for homogeneous nucleation. Most studies have concentrated on the low-to-moderate damage region and heterogenous nucleation might be the main fracture mechanism. On the other hand, higher stresses (above the thresholds for both) will probably induce both homogeneous and heterogeneous nucleation. Another aspect to consider is that different heterogeneities (or similar heterogeneities of different size) most certainly have different thresholds. Figure 31 shows cracks emanating from the two sides of a MnS particle (the fracture is shown by an arrow). Figure 32 shows two additional fracture nucleation events in AISI 1010 steel. There is clear evidence that the process is not entirely brittle and that crack-tip plastic deformation is significant, for the latter case (Fig. 32). Two spheroidal nuclei can be seen in Fig. 32(b). One can also see the complete separation along the MnS particle in the left-hand side of Fig. 32(b). The MnS particle of Fig. 32(b) is cracked; the mechanism of fracture in this case is of void coalescence. Iron and steel undergo a ductile-to-brittle transition when the rate of the application of the load is increased (or the temperature is decreased) below a critical level. This aspect

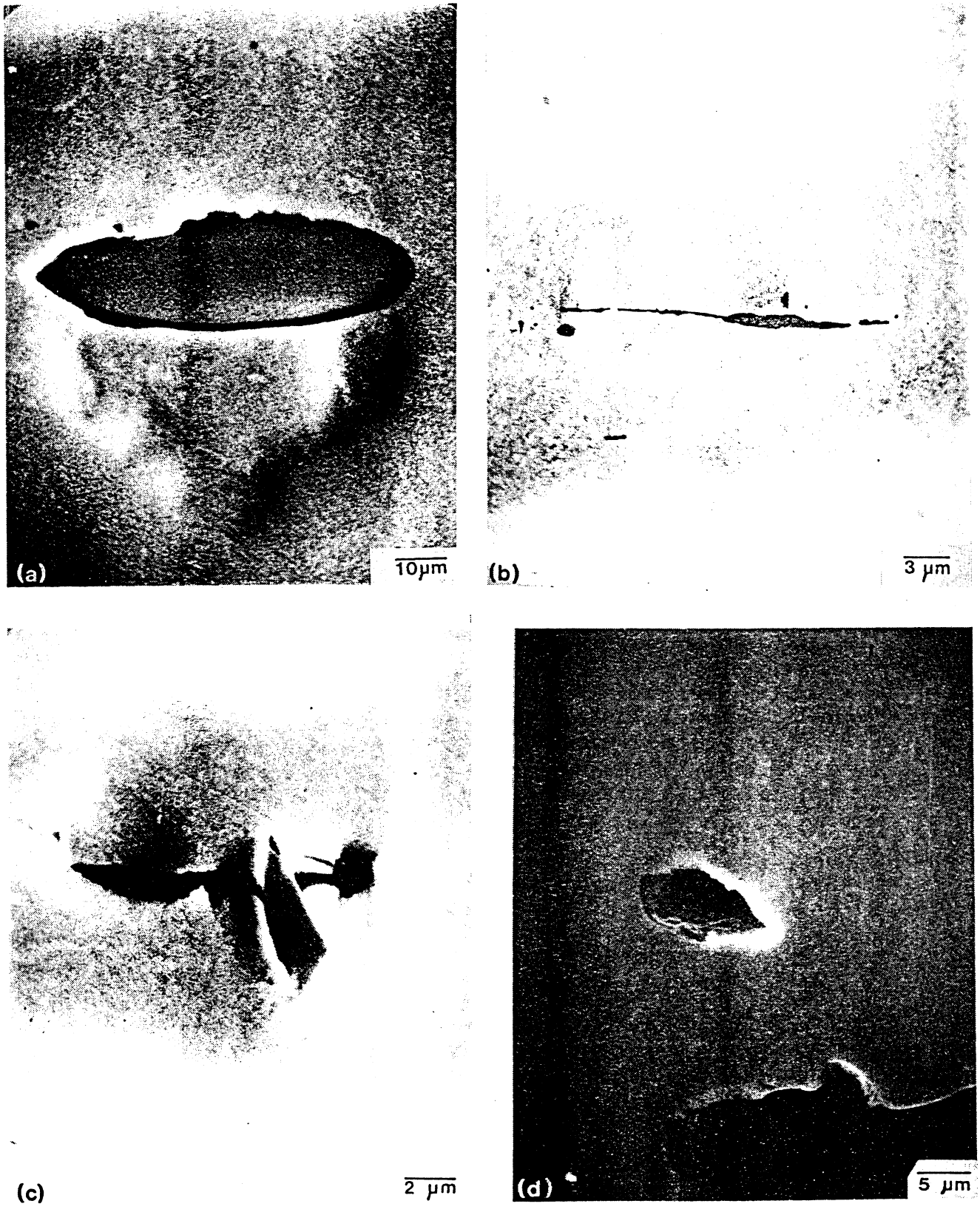

FIG. 30. Four different sources of spall initiation in steel. (a) Debonding at MnS–matrix interface; (b) crack starting at MnS and propagating into matrix; (c) crack starting at silicate interface and propagating into matrix; (d) void apparently homogeneously generated. (Spec. A.)

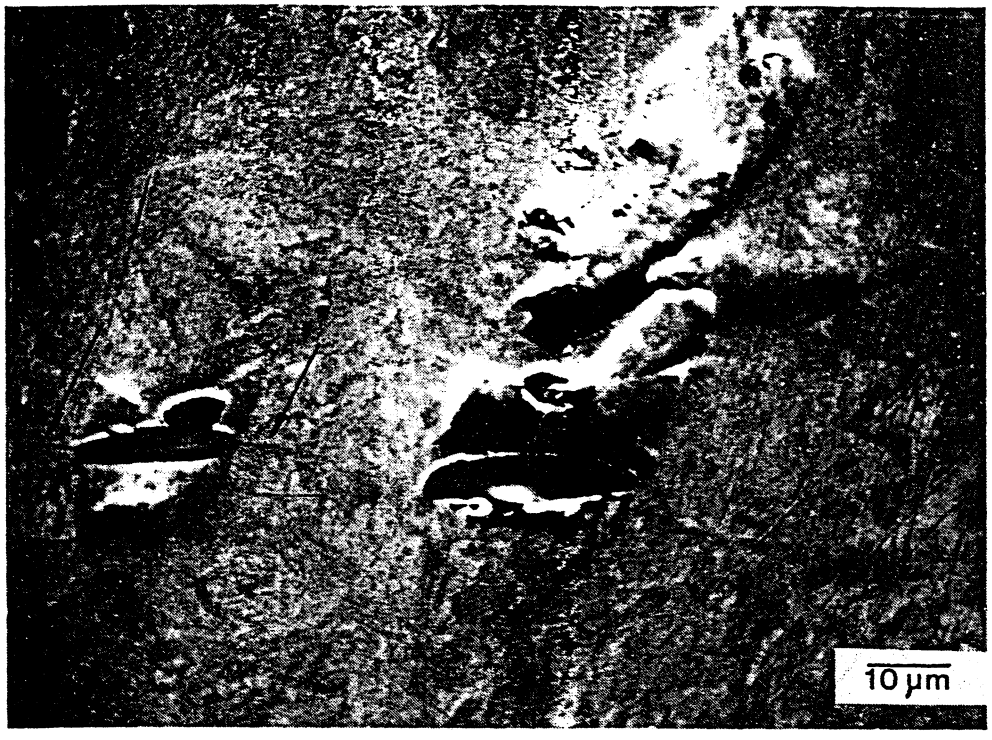

FIG. 31. Brittle fracture in steel initiated at MnS–matrix interface. (Spec. A.)

will be discussed later; in Fig. 32(b) the ductile response of steel might be due to the fact that deformation was imposed at a slower strain rate than in Fig. 31. This could be indicative of the reverberations of the wave. After the first impulse, subsequent reverberations could have lower stress-application rates, such as was demonstrated for PMMA by Curran and co-workers[36] (Fig. 18). Figure 33(a) shows the propagation of a crack throughout a pearlite colony. Cementite being a brittle constituent, the plane of the crack is probably the same as that of the lamellae. The brittle constituent is an easy path for crack propagation. The scanning electron micrograph of Fig. 33(b) shows how the cracks travel from precipitate to precipitate, forming bridges between them. The path is determined by the stress fields around the particles. Some degree of damage by shock-wave interactions with second-phase particles is also expected to occur and is observed in Fig. 33(c). In addition to debonding, one sees some void formation clearly associated with the presence of the inclusions (arrows A in Fig. 33c); the reflection of the wave at the particle is the probable source of the damage. One can also see voids in the same micrograph (arrows B).

Figure 34(a) shows the damage produced in nickel by spalling. Numerous spherical voids can be seen; as they grow and coalesce with other ones, they become elliptical. No obvious heterogeneity is seen in many of them by optical microscopy. Ni-200, containing approximately 0.5% impurities, was used in that experiment, and numerous second-phase particles were seen. Fig. 34(b) shows a string of particles (aligned along the rolling direction). Each of them nucleated a void, and one can see a cracked particle which is indicated by an arrow. Etching of the specimen revealed no predilection of nucleation at the grain boundaries.

The emphasis of past research having been mostly to (a) determine the spall strength of different materials, and (b) develop models for fragmentation based on a homogeneous material, little attention has been given to the observation of microflaws at higher magnification. Indeed, a magnification of 100× has been the highest used, to the author's knowledge. This topic is further discussed in Section 4.4. Figure 35 shows a typical polished

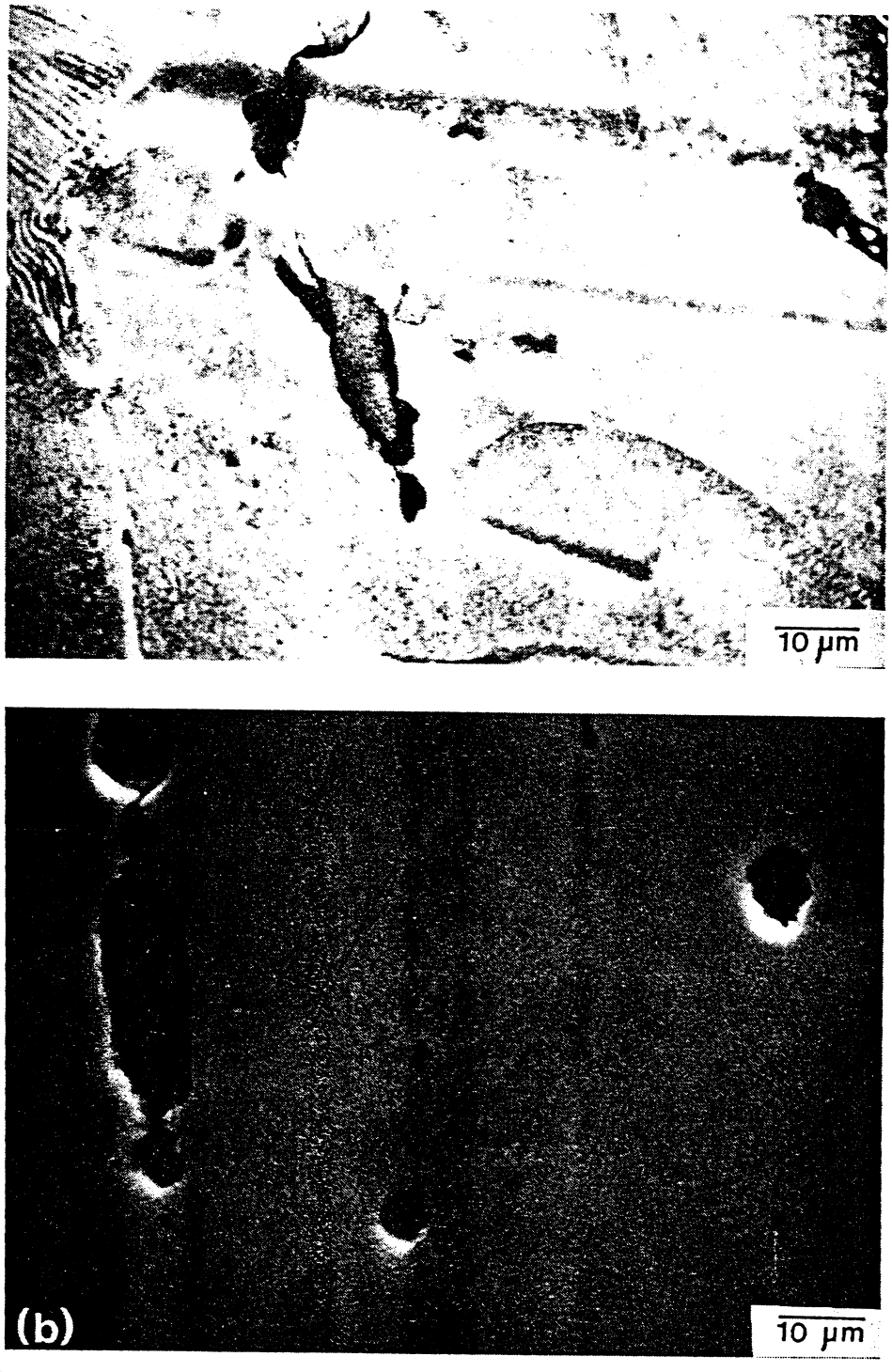

FIG. 32. Two incidences of fracture initiation at MnS–matrix interface in steel. In (b), fracture propagates in a ductile manner, by void nucleation and growth. (Spec. A.)

surface of spalled nickel, at a magnification of 75×. In an attempt to observe smaller voids, the region marked with a square was observed by scanning-electron microscopy, individual photomicrographs being taken at 10.000×. The montage of twenty photomicrographs is shown in Fig. 36. The area was selected at some distance from an incipient flaw. Figure 36 shows second-phase particles, microvoids, and microcracks. However, nucleation seems to be a discrete event, and one cannot see a large number of voids. Inside the second-phase

particles (indicated as inclusions) one can see irregularly-shaped voids which can be labelled as microcracks. As these flaws inside the inclusions grow, they will eventually take up all of the inclusions, so that at a lower magnification the original flaw source cannot be detected. The main conclusion that one can make from Fig. 36 is that the number of small voids is

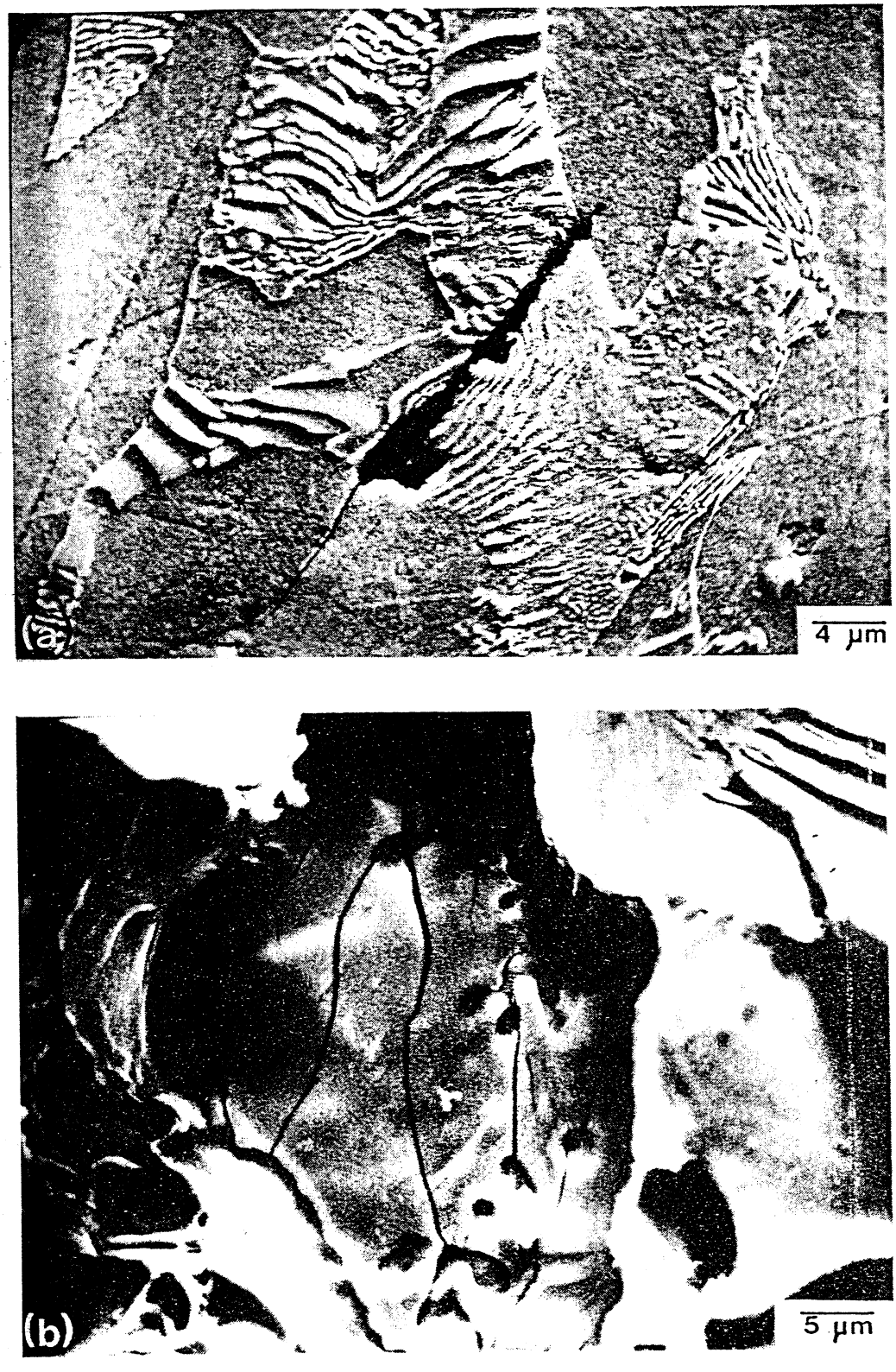

FIG. 33.

FIG. 33. (a) Crack propagating through pearlite colony; notice that crack stops in ferrite grain (SEM). (b) Cracks in steel propagating in brittle mode and joining second-phase particles (SEM). (c) Three MnS particles (indicated by arrows) in whose surroundings damage can be seen. (Spec. A.)

not much larger than larger voids. A quantitative study of the small void density is definitely needed.

4.2. *Growth*

The morphology of the spall is determined by the fracture propagation path and growth mode. Three distinct morphologies are shown in Figs 37–41. The iron–nickel alloy of Fig. 37 underwent a heat treatment that resulted in the precipitation of carbides along grain boundaries; this condition is termed "sensitized" in stainless steel. The fractured carbides along the grain boundaries provide an almost continuous fracture path, and the scanning electron micrograph of the spall surface shows an intercrystalline mode. The individual grain boundaries are seen in Fig. 37(b). while Fig. 37(a) shows a region in which an incipient spall occurs by the separation between two grains at a grain boundary. One can see a martensite lens in the same micrograph. Figure 38(a) shows the spalled surface of AISI 1010 steel. One sees the flat surfaces characteristic of brittle fracture. The preferential cleavage planes determine the plane of the fracture within a grain; when the fracture path has to change to another grain, an accommodation has to take place and the special pattern of stepped cleavage surfaces is thus produced. The brittle fracture is in every aspect similar to the one generated in a Charpy test (Fig. 39). The same flat cleavage surfaces are seen, and one can see, by comparing the two surfaces, that the mechanisms of crack propagation and joining are the same. The ductile-to-brittle transition undergone by steel as the strain rate is increased is similar in nature to the one observed when the temperature is decreased. The Charpy specimen of Fig. 39 was preshocked; it was taken from a plate through which a

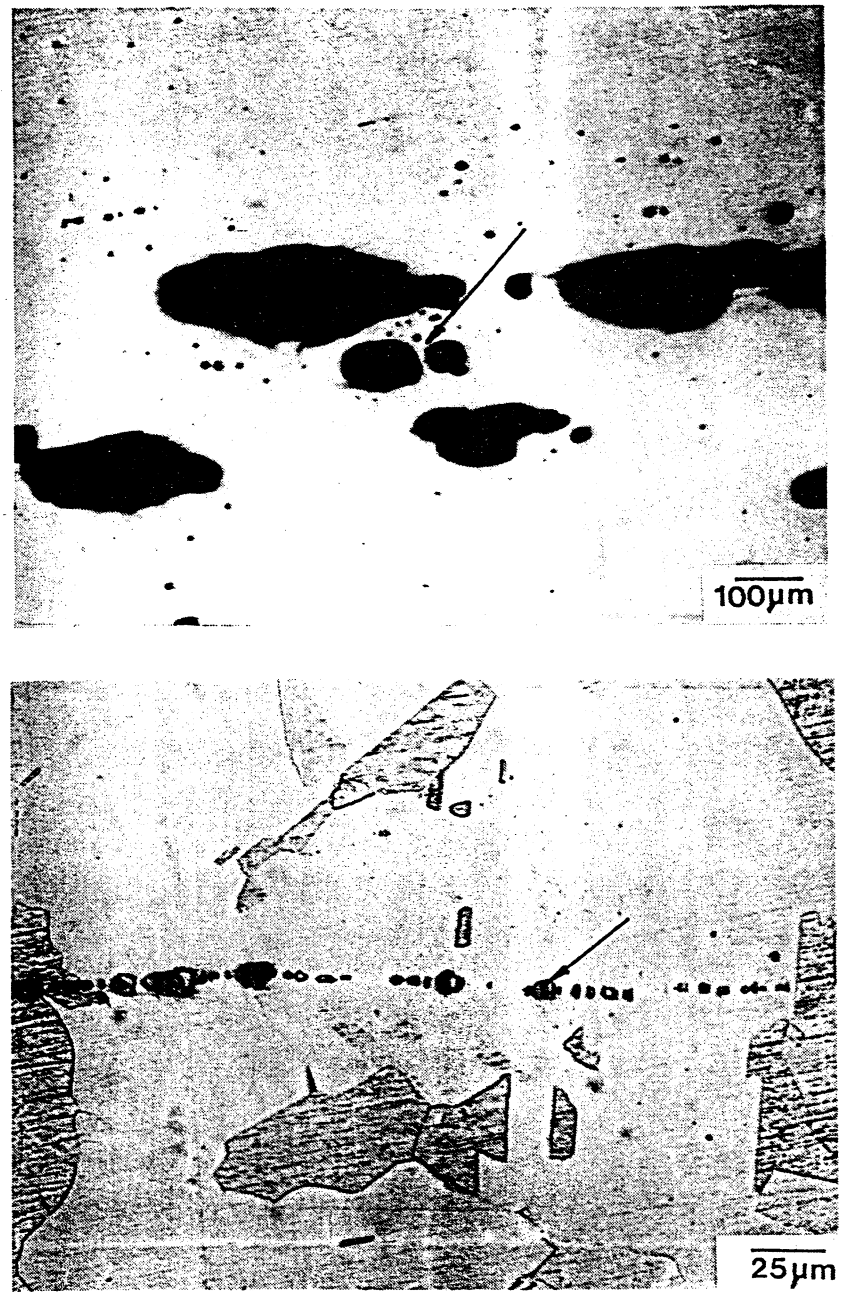

FIG. 34. (a) Void nucleation, growth, and coalescence observed in nickel. (b) Formation of a string of voids by nucleation at second-phase particles in nickel. Some second-phase particles that are fractured can be seen. (Spec. B.)

shock wave had passed, in order to incorporate any effects due to shock conditioning. This care is required because one knows that the compressive shock wave precedes the tensile reflected wave, and strengthening due to the former might affect the development of the latter. Conventional deformation at a slow strain rate does not induce brittle fracture, as is evident in Fig. 38(b); the typical dimpled surface is observed. One should not associate each dimple to a second-phase particle. In some cases, the density of dimples greatly exceeds the areal density of inclusions. Wilsdorf[108] found, in AISI 304 stainless steel, that the void (dimple) density was greater than the particle density by a factor of 100. The same is

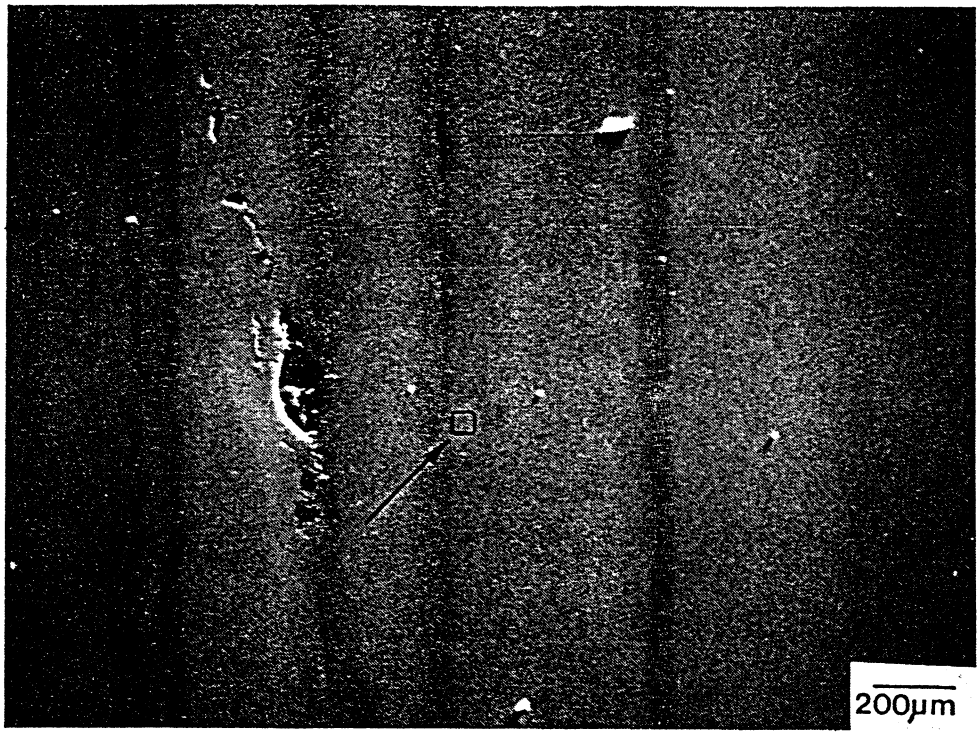

FIG. 35. Appearance of surroundings of spall in nickel (SEM of polished section); square indicates portion that was magnified. (Spec. B.)

probably true in metals that spall in a ductile manner when the pressure is fairly high; while a few dimples are due to nucleation at second-phase particles, a number of them are due to homogeneous nucleation of the voids.

Figure 40 shows a stage of early propagation of the cracks in AISI 1010 steel; one can observe that the cracks, originally formed at MnS particles, join along lines parallel to the tensile wave front, with occasional jumps when no crack is available in the original plane.

Nickel is a very ductile material and both the dynamic and quasistatic (Figs 41(a) and (b), respectively) fractures have the characteristic dimpled appearance. It was observed, however, that the dimples are deeper in the quasistatic (by tensile extension at $\sim 10^{-3}\,s^{-1}$) case than in the dynamic one. Dimple depth is, to a certain extent, a measure of ductility, and this would indicate a certain loss of ductility (and work-hardening ability) at the higher strain rates. The difference could also be due to the more uniform mechanism of fracture propagation in spalling, wherein a large number of voids grow simultaneously and independently. A few interesting observations can also be made on void initiation sites. Although a number of voids initiated homogeneously, it is quite clear from Fig. 42 that second-phase particles are favored initiation sites; this corroborates the observations made in Fig. 34(b). When failure initiation takes place in the second-phase particle, it occurs by brittle fracture and debonding; both are seen in Fig. 42. In the right-hand side of Fig. 42(b), on the other hand, one can see a void that seems to have nucleated homogeneously. Fig. 42(a) also shows void coalescence, a prominent feature of failure propagation. Debonding on the right-hand side of the particle produced a wedge-shaped void which is advancing to meet the void on the right-hand side of the photograph: coalescence will effectively double the void size. Figure 43 shows two other coalescence events, when two adjacent voids grow and are reduced to one. There are mentions in the literature to the possible high temperatures generated by void growth; some investigators believe that melting could even occur. Our observations on nickel seem to contradict this hypothesis. High temperatures would un-

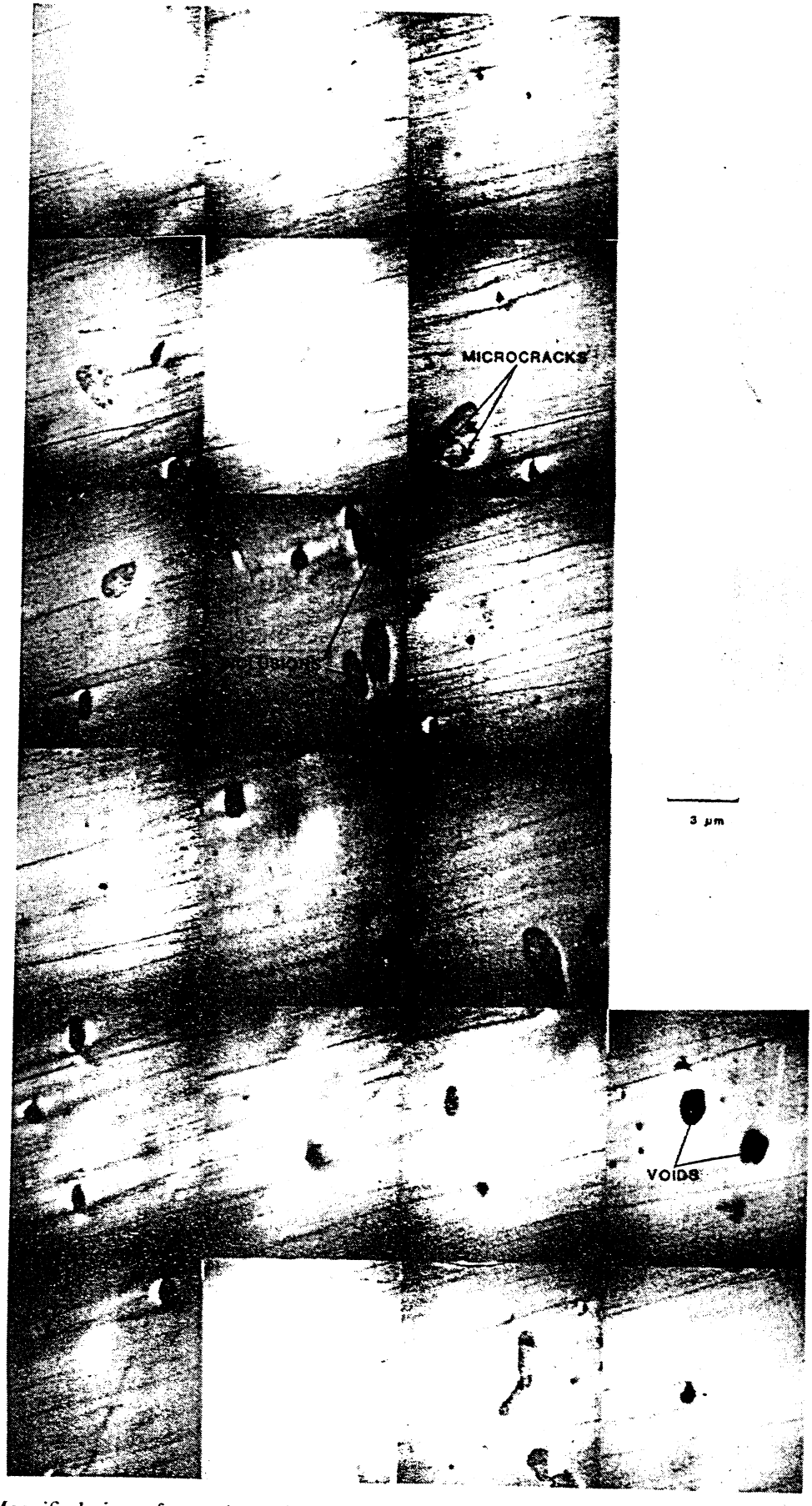

FIG. 36. Magnified view of area shown in Figure 35; individual photomicrographs taken at 10,000 × magnification. Notice microcracks forming at second-phase particles and ductile voids forming homogeneously in matrix.

doubtedly leave "fingerprints" in the structure, and etching of the specimens does not reveal any special feature in the regions adjoining the voids (such as the formation of a microcrystalline or microdendritic structure or grain-boundary migration). One feature of interest in Fig. 43(b) is the deformation undergone by the annealing twin on the right-hand side; its initially straight shape is deformed by virtue of the material flow around the void. In a similar way, a grain boundary on the left-hand side (marked by arrow) is deformed from its original shape.

Another mechanism of fracture propagation which, strictly speaking, cannot be classified as coalescence is the one shown in Fig. 44. It represents the shearing action between two void sheets (planes along which voids are connected), in order to connect them. The region surrounding the shear zone is severely deformed, as evidenced by the distorted grain structure. This jumping of the spall from one plane to the other is responsible for the irregular appearance of the spall surface.

With the exception of the SRI work, little effort has been devoted to the determination of the metallurgical parameters on the propagation of spall fracture. In 1973, Stevens and Pope[28] reported differences in the propagation of the spall fracture among different specimens of hot-pressed beryllium powder. Although the spall strength was not significantly altered by the degree of texturing, the distribution and character of the spall damage was. This is indeed understandable, if one considers that cleavage fracture within the individual grains occurs on the basal plane. If most of the basal planes are in the same plane, such as is the case for highly textured beryllium, one would expect more continuous and parallel spall cracks in the material. If, on the other hand, the grains are randomly oriented, one would expect spall cracks randomly oriented in direction. Thus, Stevens and Pope[28] showed how differences in texture can alter the spall morphology. In another study involving metallurgical variables, Jones and co-workers[51–53] investigated two different aluminum alloys (2024 and 6061) under different stages of age hardening. Their experimental technique consisted of fabricating a hollow cylinder of the alloy and detonating an explosive charge along the central axis, so that spalling was produced close to the external surface of the cylinder. The design parameter that was changed was the external diameter of the cylinder. As it was increased, the amount of spall damage decreased, and this is obviously due to the attenuation of the wave. For the geometry used, one has both the physical attenuation of the wave because of dissipative mechanisms within the material and geometrical attenuation due to the increase in front area of the wave as it expands radially. Jones and Dawson[52] observed that fracture damage in 2024 Al increased during aging while in 6061 Al it decreased from the solid solution condition to the critically-aged condition and then increased again during overaging. They interpreted their results in terms of coherency strains around the G–P zones. They also subjected annealed and pre-strained copper to the same experimental procedure and found an increase in dynamic fracture resistance with increase in pre-strain. Figure 45 shows typical results for 2024 Al (Fig. 45a) and for 6061 Al (Fig. 45b) for a tube diameter of 20 mm. Six different aging conditions are shown in each figure, and one can clearly see that it definitely has an effect on the extent of spalling. Axter *et al.*[53] attributed the differences in spalling to the initiation of fracture at second-phase particles; different aging treatments resulted in different amounts of brittle second-phase particles which, in their turn, produced different concentrations of nucleation sites. Figure 46(a) shows cracked second-phase particles (gray) and voids in 2024 Al; observation by scanning electron microscope by Jones[51] revealed profuse debris of the fractured particles in conjunction with the ductile dimpled fracture of the aluminum matrix. Shockey *et al.*[40] investigated the effect of grain size on the dynamic fracture behavior of α-titanium; they used specimens with average grain diameters of 1.5 and

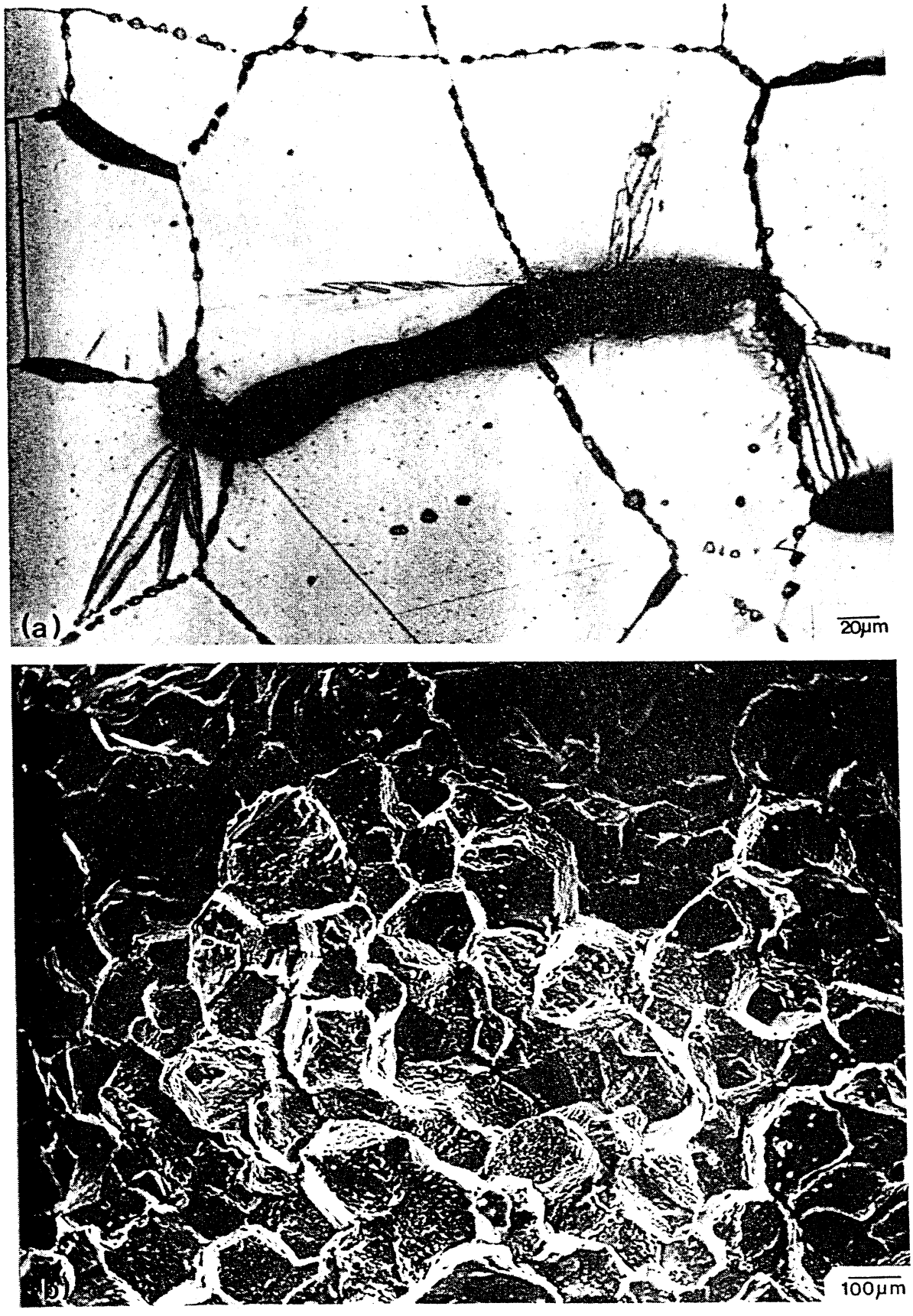

FIG. 37. Spalling by intergranular fracture in Fe-32% Ni-0.035% C. (a) Optical micrograph of polished and etched section showing grain-boundary precipitates; (b) scanning electron micrograph of spall surface showing individual grains. (Spec. C.)

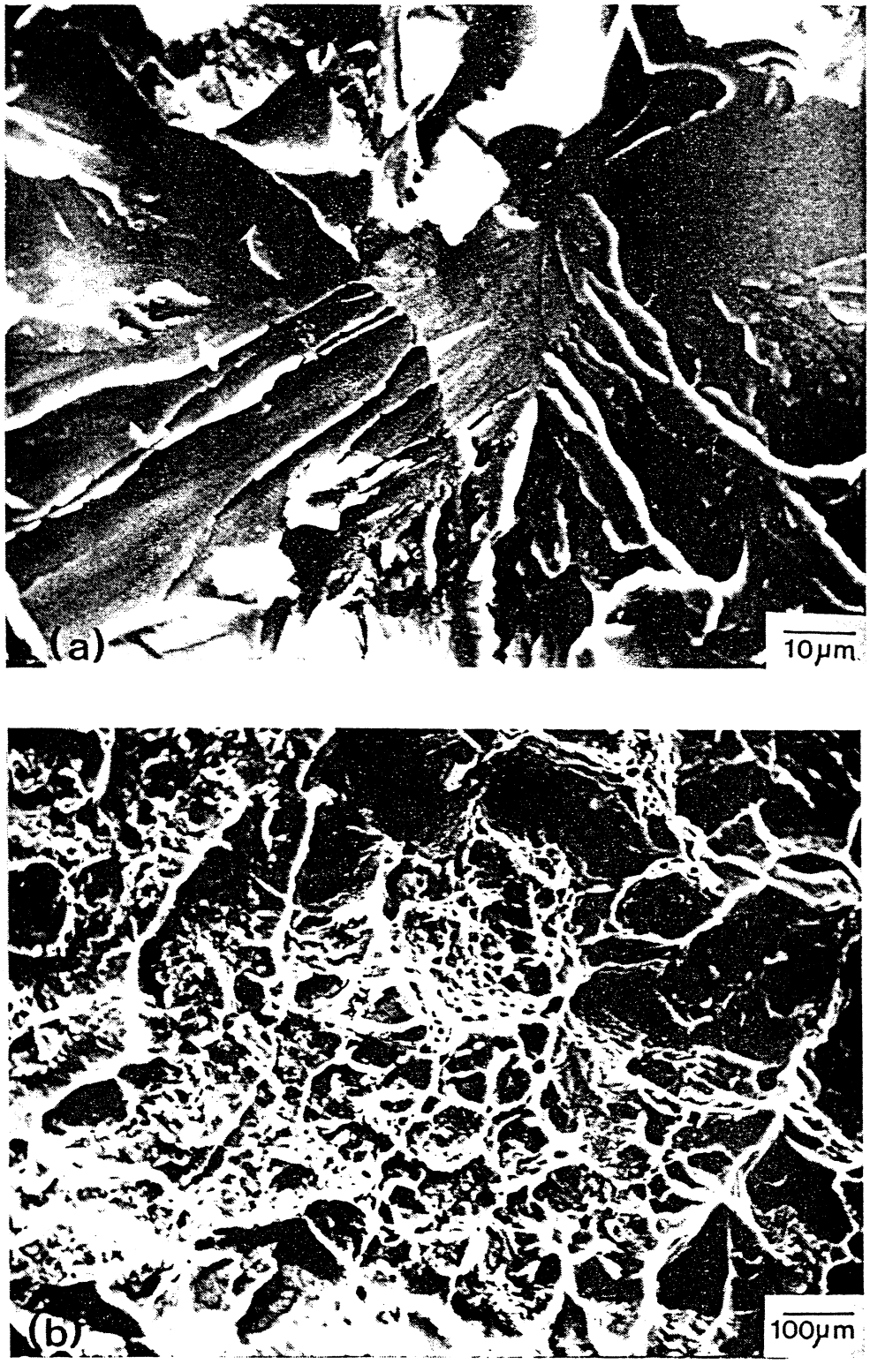

FIG. 38. (a) Spall in steel produced by propagation of cleavage cracks in grain: notice stepped appearance of cleavage cracks to accommodate general fracture plane (SEM). (b) Ductile fracture in steel preshocked and deformed in tension at $10^{-3}\,s^{-1}$ (SEM).

FIG. 39. Brittle fracture of steel in pre-shocked condition after impact in Charpy impact machine (SEM).

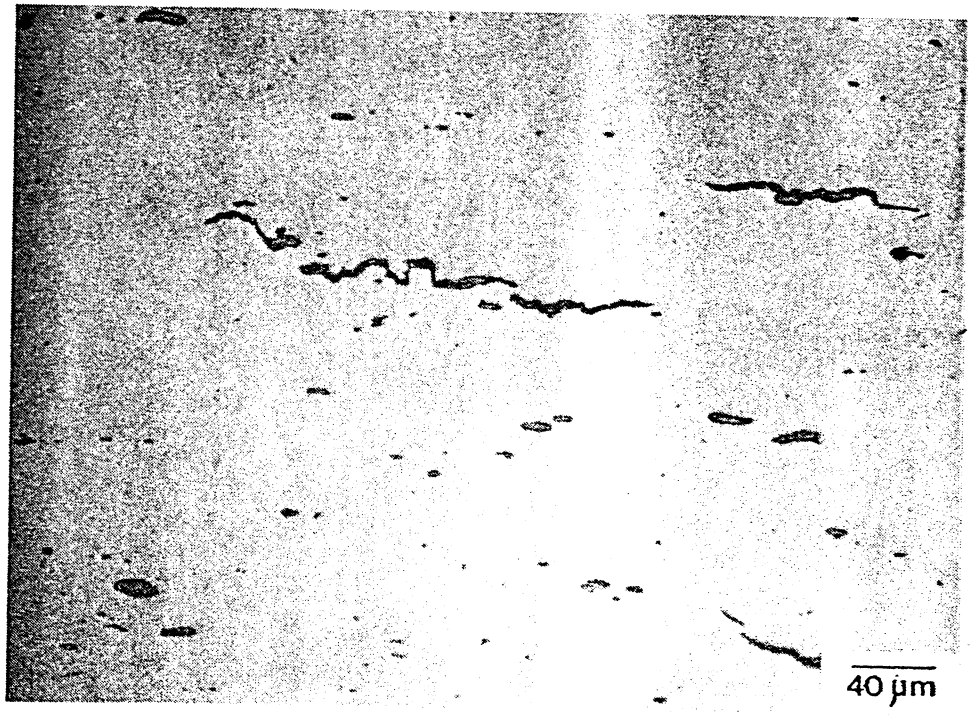

FIG. 40. Fracture initiation and propagation in steel specimen: notice initiation at MnS particles and propagation by joining at different levels (optical). (Spec. E).

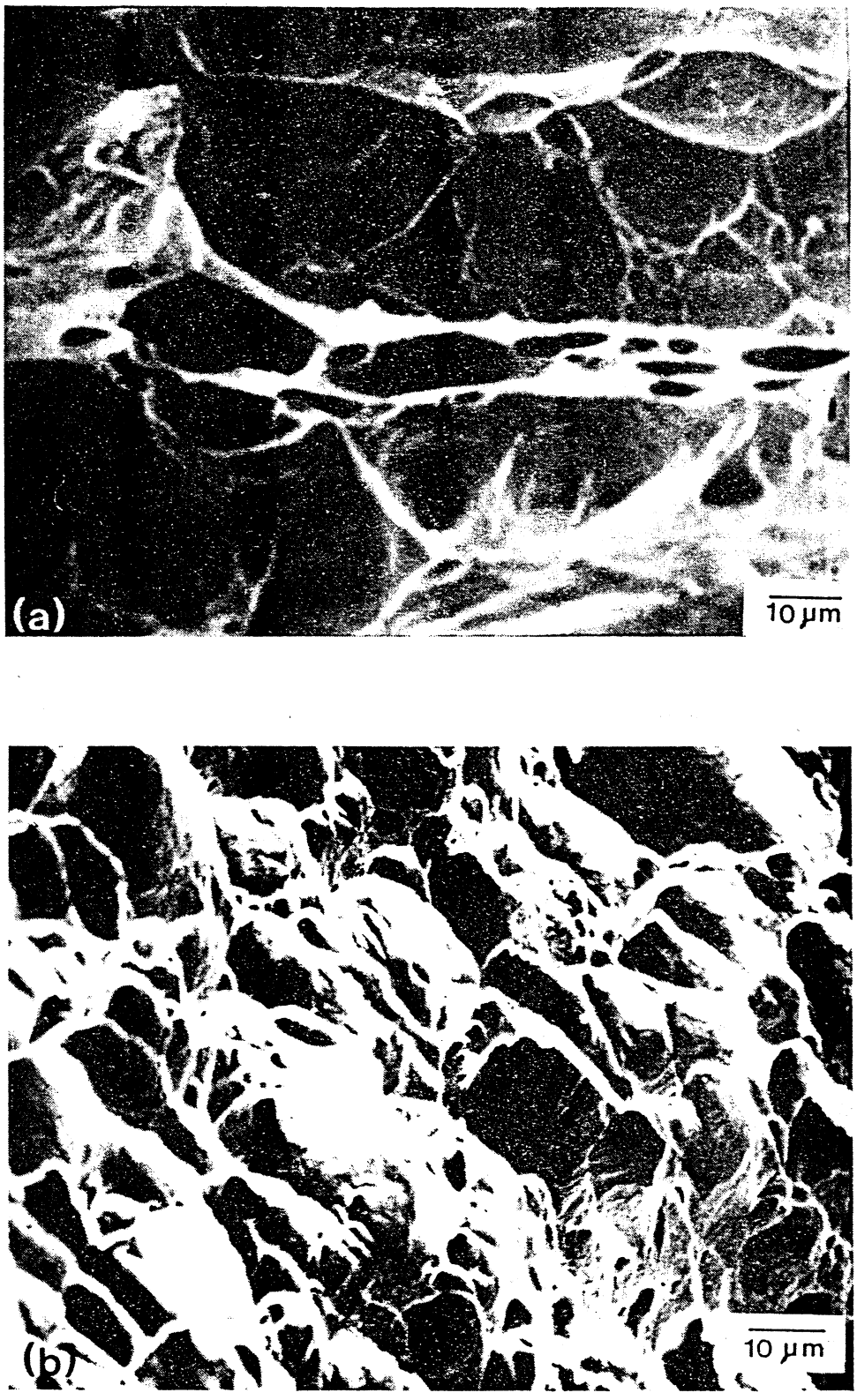

FIG. 41. (a) Spall fracture in nickel (SEM); (b) fracture in nickel produced by conventional extension in tensile test at $10^{-3}s^{-1}$ (SEM). Observe dimples that are deeper in (b) than in (a). (Spec. B.)

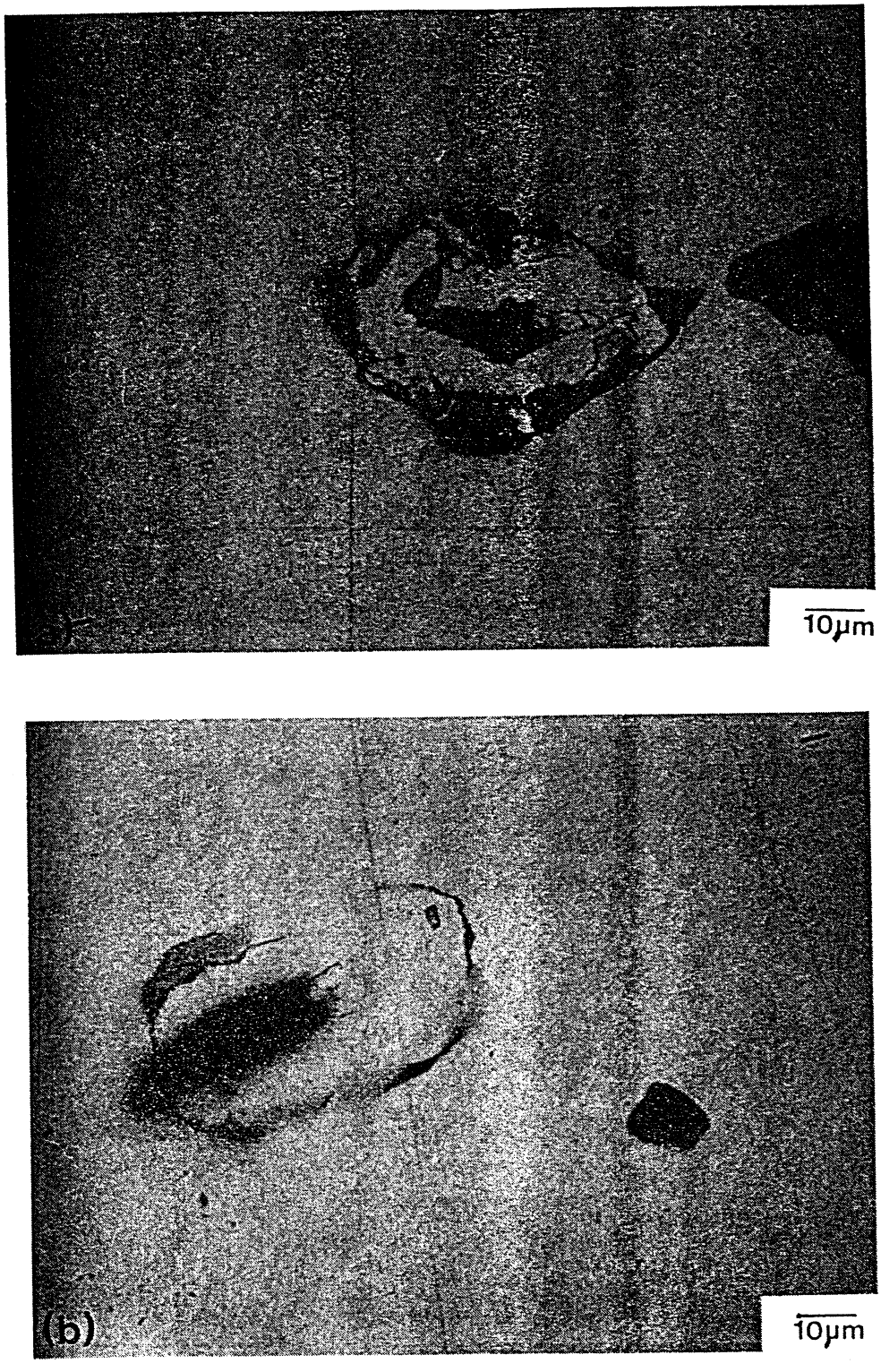

FIG. 42. Fractures starting at second-phase particles in tensile region of pressure pulse in nickel (optical). (Spec. B.)

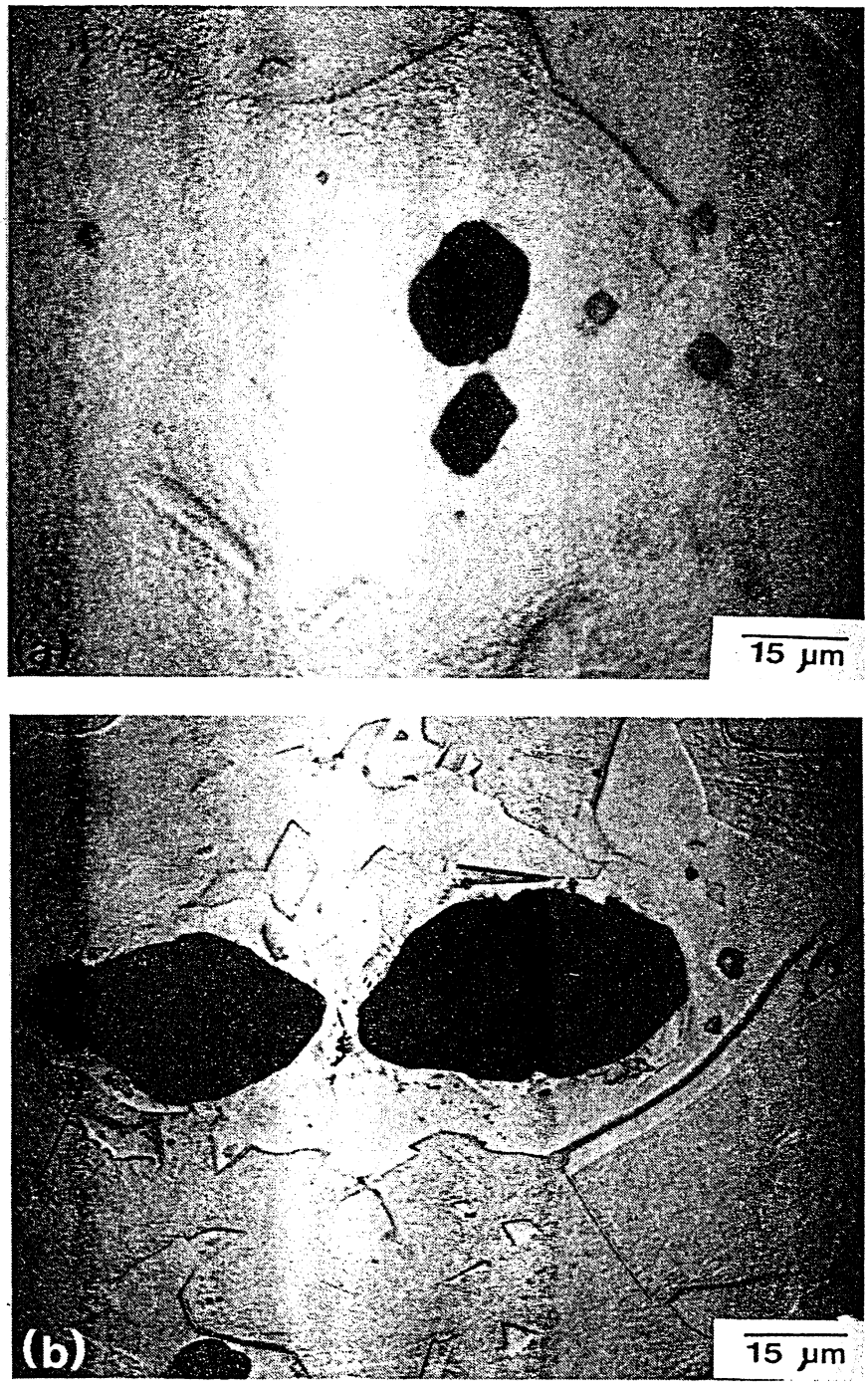

FIG. 43. Adjoining voids in nickel in the process of coalescing. Notice distorted annealing twin in right-hand side of (b) (optical). (Spec. B.)

36 μm and conducted a systematic sequence of gas-gun experiments, producing various levels of incipient spalling; they accomplished this by varying both the pressure and pulse duration. They found that the failure began at the same level for both cases; the rate of propagation of damage was much higher for the small-grained material. They considered the greater number of grain-boundary triple points (the observed failure initiation sites) as the reason for the lowered resistance to dynamic fracture of the small-grain-sized condition. This lower spall resistance of the 1.5 μm material is contrary to the quasi-static behavior; the yield stresses are equal to 522 and 363 MPa for the grain sizes of 1.5 and 36 μm, respectively.

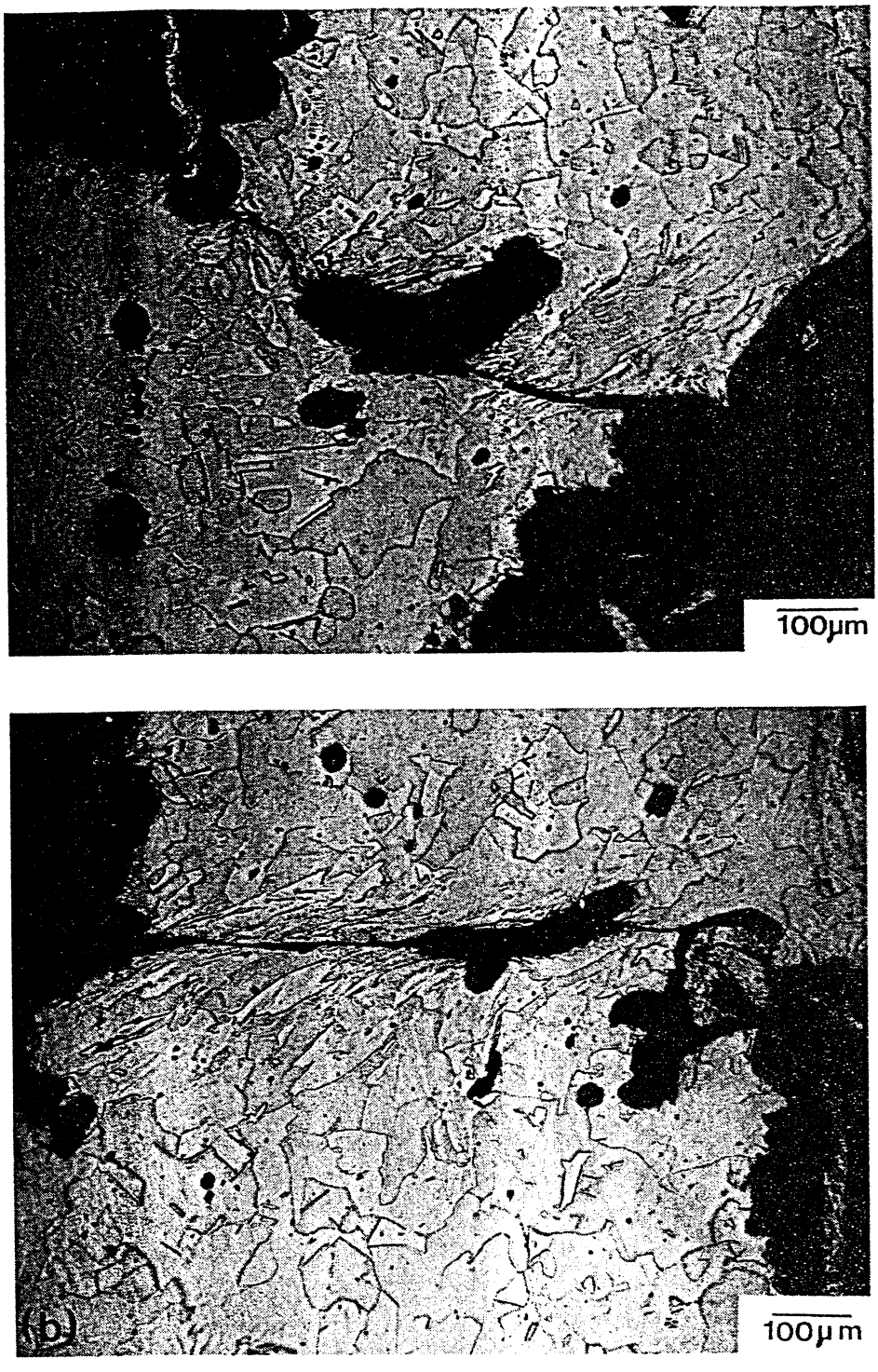

FIG. 44. Intense shear localization in spall region of nickel when void sheets on two different phases coalesce. (Spec. B.)

Morton *et al.*,[109] in an overview of ballistic penetration work done in Australia, report substantial differences in the spall behavior of steels. They found that the extent of spalling was significantly reduced in steels containing unusually fine non-metallic inclusions, such as electroslag-refined low-alloy steel in the quenched and tempered condition. The greater spall resistance of ESR steel was attributed to the absence of large inclusions and they concluded that the nucleation phase of spalling was very important.

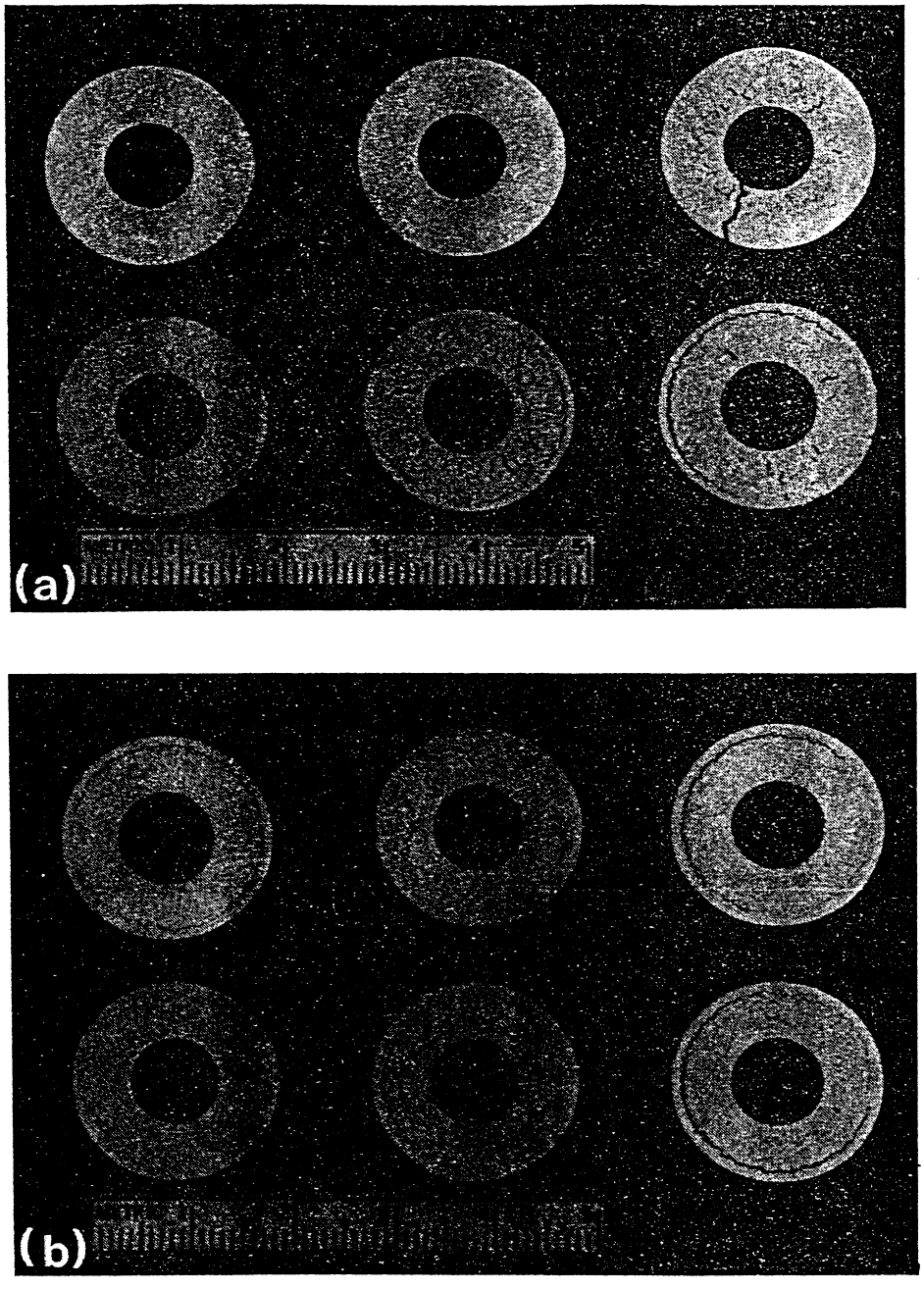

FIG. 45. Effect of aging treatment on spalling produced in (a) 2024 and (b) 6061 Al by an explosive load detonating in the inside of a cylinder. Six different aging conditions shown for each alloy. (From W. B. Jones, M.Sc. Thesis, U. of Washington (1973) Figs. 3.4 and 3.15, respectively.)

Mock and Holt[57] recently determined the spall strength of HF-1 steel and, after performing a number of systematic experiments, determined the rates of nucleation ($\dot{N}$) and growth ($\dot{R}$) of microflaws after different heat treatments. One heat treatment (A) produced tempered martensite, while the other (B) produced pearlite and grain-boundary cementite. Although the growth parameters were similar for the two treatments, the nucleation threshold stress was about 40% higher and the nucleation rate was 30% lower for treatment A. This confirms the contention that metallurgical parameters are of considerable importance in spalling.

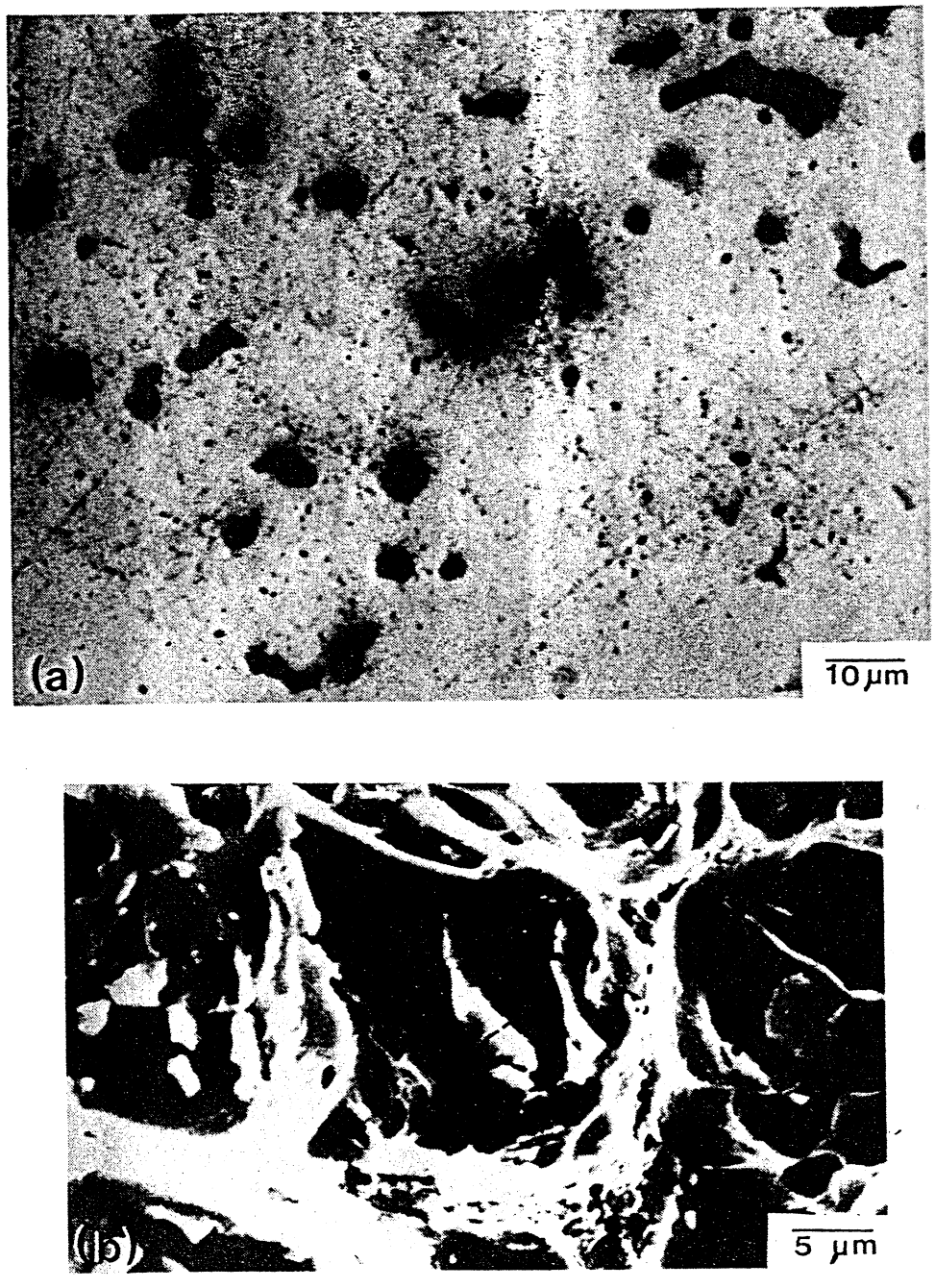

FIG. 46. (a) Cracked second-phase particles (gray) and voids in spalled 2024 Al. (b) Scanning-electron micrograph of spall in 2024 Al showing brittle fracture of second-phase particles and ductile fracture of matrix. (From W. B. Jones, M.Sc. Thesis, U. of Washington, (1973) Figs 3.2 and 3.9(a), respectively.)

4.3. *The Rough and Smooth Spalls in Iron and Steel*

Under certain conditions (above a certain stress) the spall morphology in low-carbon steels changes drastically. No high-magnification observation is required, and the change in fracture morphology can be observed by naked eye. This phenomenon was first reported

and studied systematically by Erkman,[110] Figure 47 shows three spall morphologies in 1010 AISI steel plates (25 × 25 cm) subjected to plane shock waves by impact by 6.5 mm thick flyer plates at various velocities. Figure 47(a) shows the spall formed after an impact (using the mousetrap assembly) producing a pressure of ~25 GPa; Figs 47(b) and (c) show spalls of impacts (using the inclined-plate assembly) producing pressures of ~13 and ~8 GPa, respectively. Details on the mousetrap and inclined-plate assemblies can be found in DeCarli and Meyers.[111] While the whole spall of Fig. 47(a) is smooth and of a texture that resembles machine finishing, Fig. 47(b) shows considerable rough spall in the edges (where the pressure is lower because of non-planarity of the edges of the flyer plate), and Fig. 47(c) exhibits a fully rough spall. Upon closer observation, one can see the details of the fracture; this is done in Figs 48 and 49. Figure 48 shows the section of the plate after etching; the lower surfaces represent the spall. One can see in Fig. 48(a) that the irregularity of the spall is of the order of the grain diameter of the specimen. Little or no damage is observed inside the material, away from the spall. In contrast to this, Fig. 48(b) shows considerable damage inside the material and the damage region extending over a distance equal to several grain diameters. One can also see the greater degree of residual deformation (twins and residues of the transformation) within the grains of Fig. 48(a); this specimen was subjected to a pressure pulse of higher amplitude (125 GPa). Scanning electron microscopy of the smooth surface revealed features shown in Fig. 49. The magnifications were successively increased in Figs 49(a), (b) and (c). The fracture morphology is definitely different from that one produced by the rough spall (Fig. 38a). One cannot see any clear cleavage planes at 1000× (Fig. 49b) while these are abundant in Fig. 38(a). In some instances, one sees deep straight grooves tending to indicate intercrystalline fracture. At the highest magnification (Fig. 49c) one can see ill-deformed dimples as if the fracture occurred in a ductile manner; indeed, this had been suggested earlier by Banks.[112]

The explanation provided by Erkman[110] for the formation of the smooth spall is based on the existence of a rarefaction shock. This is a sudden drop in pressure in the rarefaction part of the wave due to the allotropic $\alpha \rightarrow \epsilon$ phase transformation. This sudden drop in pressure was postulated earlier by Drummond,[113] based on the analysis of the P vs v/V_0 curve and its effect on shock-wave velocities. This sudden drop in pressure results (in the reflected portion of the sequence) in a sudden rise in the tensile pulse. This sudden rise in the tensile pulse occurs in a very narrow region; the ensuring fracture region is highly localized and consequently the spall is smooth. On the other hand, the more gradual increase in the tensile stress pulse that occurs when the rarefaction portion of the pressure pulse is sloped, allows the initiation and propagation of damage over a wider region, resulting in a more irregular pulse. Figure 50 reproduces a distance–time plot developed by Erkman[110] and used to calculate the distance of the smooth spall from the free surface of the target. The smooth spall should occur at the position where the first shock wave (the wave decomposes into two shock fronts at 13 GPa, due to the phase transformation—more details can be found in Barber and Hollenbach[114] intersects the rarefaction shock. This intersection should provide the tensile spike required for spalling. Erkman[110] compared the results of his calculations with experimental results and found reasonable agreement. However, one would expect spall failure at approximately that same position even if no rarefaction shock wave were involved, and the smooth and rough spalls occur in approximately the same plane, as shown by Fig. 47.

Additional reports on the formation of smooth spalls were made by Ivanov and Novikov[115] who applied two explosive charges at the ends of a steel cylinder. The region in which the two waves superimposed (as they converged travelling along the axis of the

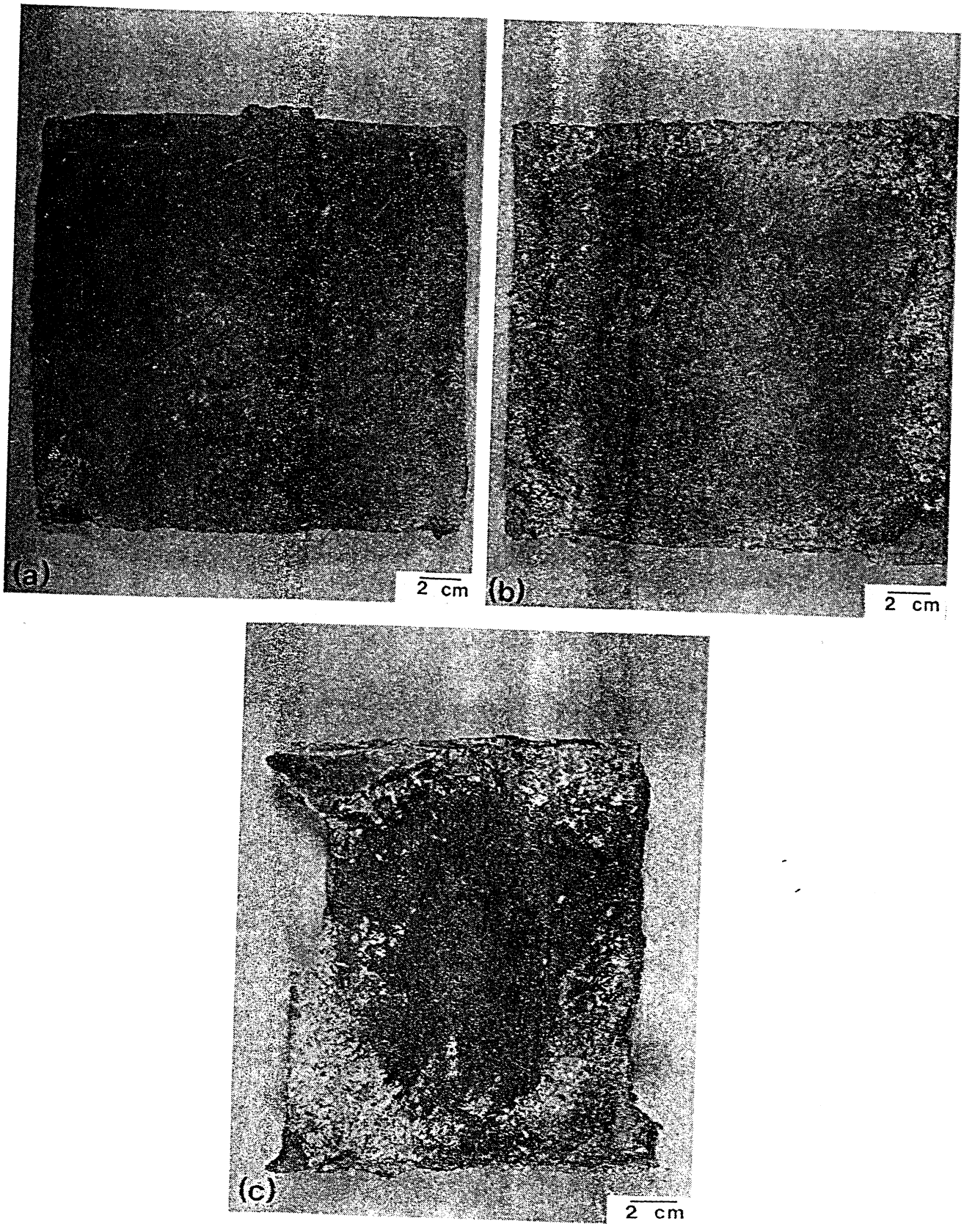

FIG. 47. Spalled AISI 1010 plates (25.4 cm × 25.4 cm) (a) $P > 13$ GPa; (b) $P \sim 13$ GPa; (c) $P < 13$ GPa. (Specs. E, F and G, respectively.)

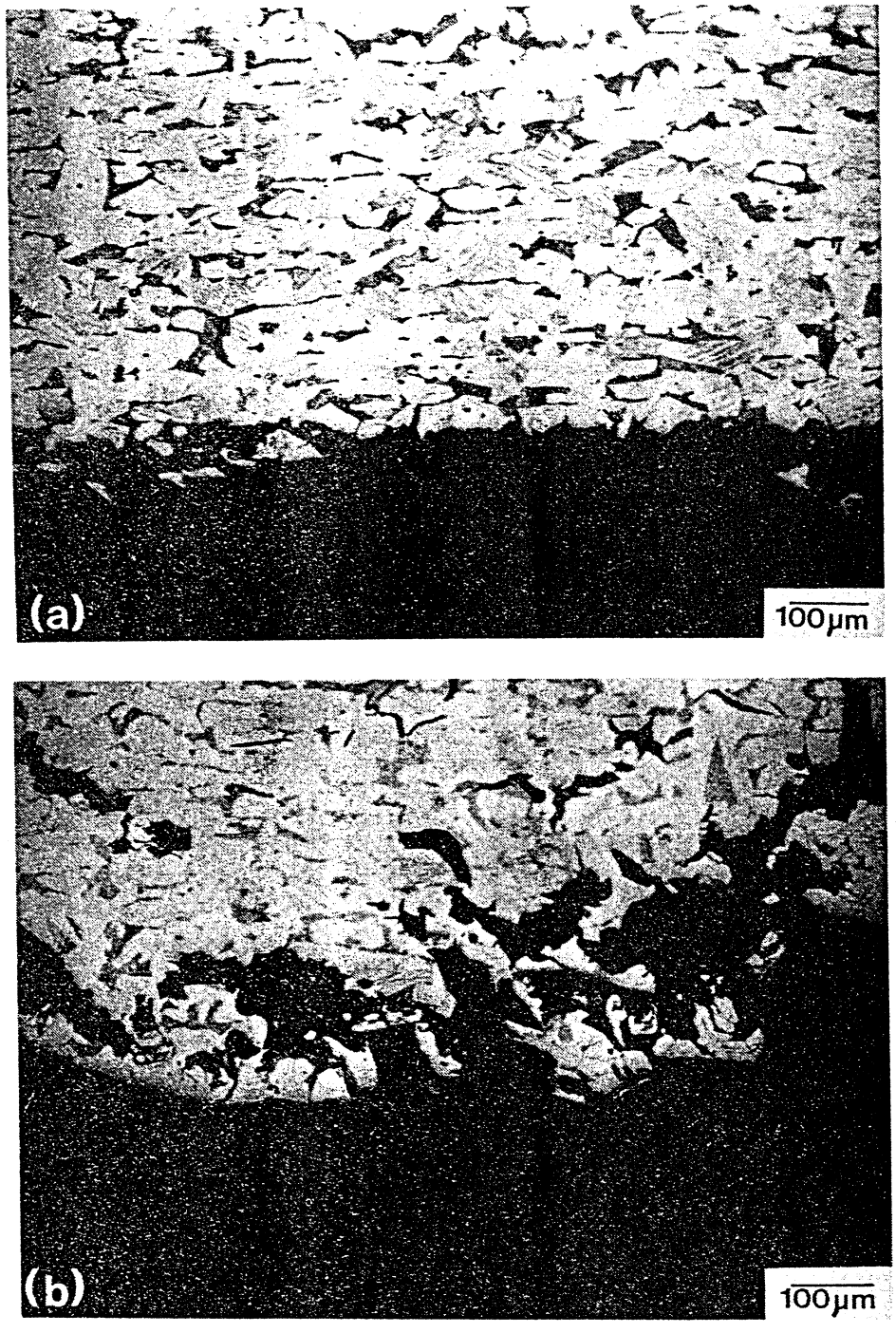

FIG. 48. Optical photomicrographs of etched sections of steel spalls. (a) Smooth spall; (b) rough spall. (Spec. F.)

cylinder along opposite senses) showed a smooth spall. Balchan[116] also found the smooth spall, in Armco iron. Meyers *et al.*[117] observed the formation of the smooth spall in AISI 1020 steel, when they forced two converging shock waves to superimpose, as shown in Fig. 51. A steel slab was covered with Detasheet-C-type explosive; detonation was initiated at the two sides simultaneously, as shown in Fig. 51(a). The inclined shock waves generated in the steel slab superimposed in the center, elevating the pressure (in the superposition region) to above 13 GPa. Subsequent observation after etching the slab revealed a dark triangle, corresponding to the region where the total pressure exceeded 13 GPa (Fig. 51b). At the

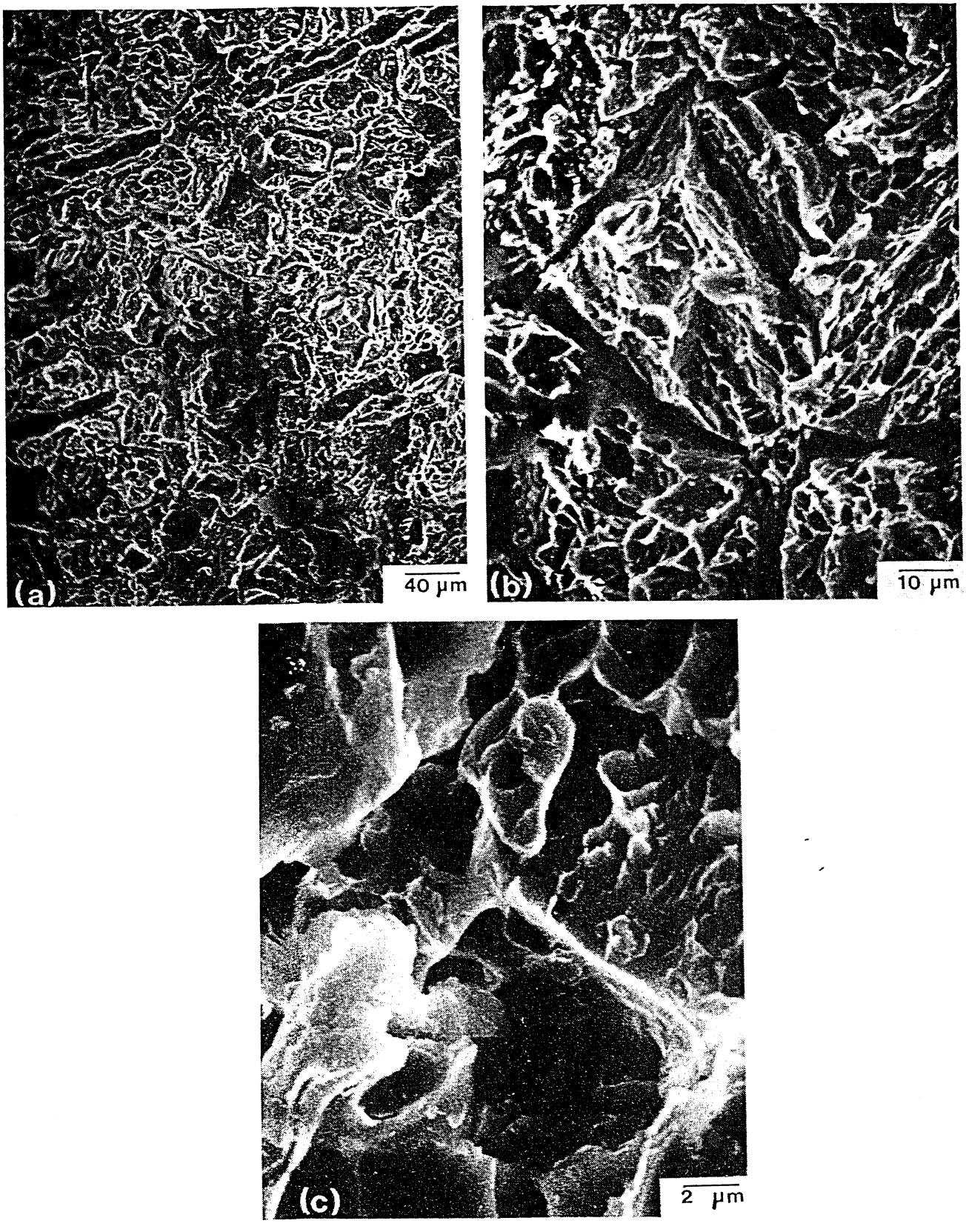

FIG. 49. Scanning electron micrographs at increasing magnifications, of smooth spall in steel.

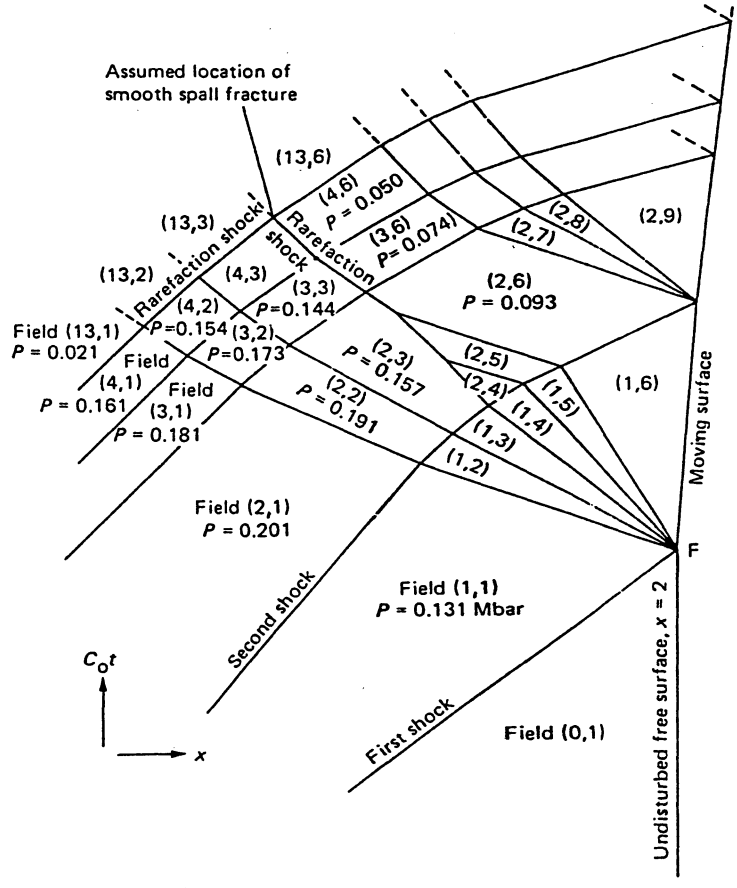

FIG. 50. Distance–time plot of steel specimen showing first and second shock pulse with different velocities reflecting back at free surface; assumed location of smooth spall shown in plot (From J. O. Erkman, *J. Appl. Phys.* **31** (1961) 939, Fig. 8.)

center of the superposition region a shaped crack formed (marked as 1 in Fig. 51c). Observation of the fracture surface revealed this to be a smooth spall. The remainder of the fracture of irregular shape (marked 2 in Fig. 51c) was of the rough type. Hence, it is possible that the preconditioning of the substructure by producing the transformation renders it amenable to smooth spalling by, perhaps, generating new nucleation sites for spalling. The existence of the profuse debris of the $\alpha \rightarrow \epsilon \rightarrow \alpha$ transformation could act as obstacles to the unimpeded propagation of cleavage cracks through the grains; on a sub-microscopic level, the smooth spall appears to be dimpled (and irregular), while the rough spall exhibits flat cleavage facets. Banks[112] conducted a careful metallographic analysis of rough and smooth spalls in a low-carbon steel (0.05% C); he found that the smooth spall was somewhat ductile in character, with regions showing voids. He classified the process of smooth spall formation as ductile.

What one can conclude from the above is that systematic and careful experimentation and metallography (optical and scanning electric) is needed before the process is fully understood.

4.4. *Additional Effects*

In this section a few effects not discussed previously will be treated. The core of the work conducted on spalling centered around the physical characteristics. The metallurgical

aspects have not been investigated as exhaustively as in other fields. To a certain extent, this is exciting because it leaves open the way for metallographic observations that are original in nature. Some of these exploratory observations are reported here.

The statistical studies of crack distribution sizes have neglected the grain size. Indeed, Fig. 52 emphatically shows that the cracks observed in Armco iron have their size determined by the grain size. Figure 52(a) shows the polished section, while Fig. 52(b) shows the same area, at the same magnification, after etching. Fracture occurs by cleavage, which is transcrystalline in nature and stops at the grain boundaries, because of the crystallographic requirements of spalling. Hence, the crack size distribution is defined by the grain-size distribution. If the grain size were five times as large, one would probably find a corresponding increase in the average crack size after the same tensile pulse conditions.

Stevens *et al.*[27] found, in monocrystalline aluminum, that the voids were cuboidal. Based on this observation, they developed a theory for the growth of voids based on dislocation generation and movement along the planes defined by the cube faces. Section 4.5 presents a more detailed analysis of this model. It will be demonstrated below that an alternative explanation for this phenomenon can be presented and justified based on the anisotropy of the plastic properties and/or surface energy of crystalline materials.

Our observations in nickel seem to indicate that, when the voids are small and well-centered within one grain, a number of them have a tendency to form flat faces. Indeed, a number of cuboidal voids were observed; Fig. 53 shows some voids which, although not being spherical, are not exactly cubical. An example of a cuboidal void is seen in the right-hand side of Fig. 42(b). Their faces tend to orient themselves along certain planes. However, as the voids grow in size and occupy a space larger than one grain diameter, they

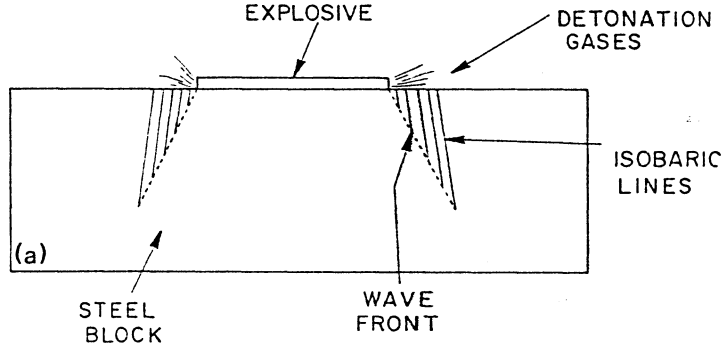

FIG. 51. (continued on next page)

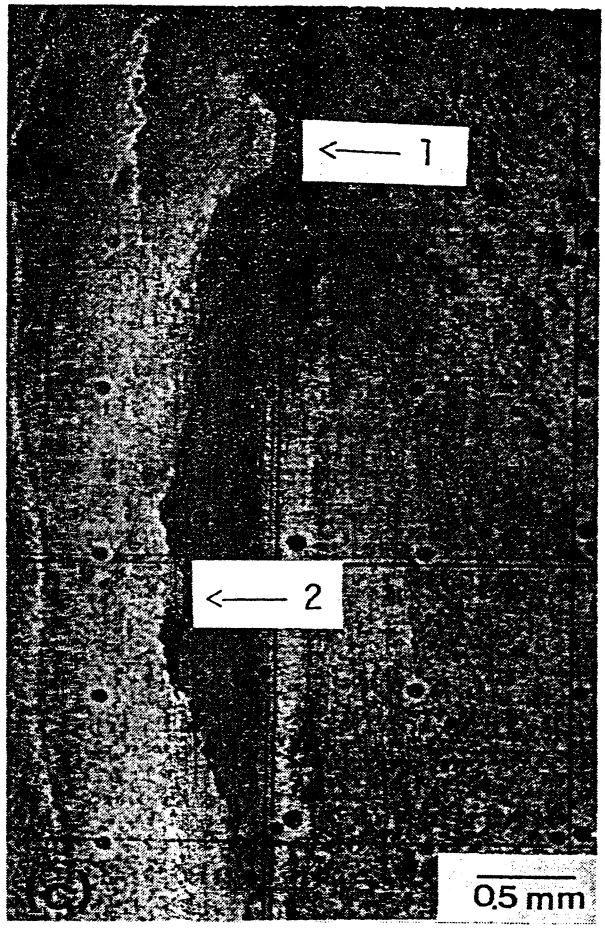

FIG. 51. Fracture produced in steel block by the superposition of shock waves produced by the converging detonation of explosives in direct contact with block. (a) Experimental configuration showing converging wave fronts; (b) appearance superposition region in section after macro-etch; (c) smooth fracture in center of superposition region (marked 1) giving rise to irregular fracture (marked 2). (From M. A. Meyers, C. Sarzeto and C.-Y. Hsu, *Met. Trans.*, **11A** (1980) 1737, Figs 3, 4 and 8.) (Spec. I.)

tend to become spherical. They retain that shape until they become ellipsoidal due to coalescence with other voids. Figures 29(b) and 34(a) show the spheroidal and ellipsoidal voids in nickel. When the spalled nickel specimen was annealed at 1100°C for one hour, the number of plane-faced voids increased substantially. Figure 54 shows five voids which have a somewhat rhombic shape (in the section). One can also see that grain growth occurred and that the grain boundaries were pinned by the voids. The original incidence of voids at grain boundaries was much lower than that after the annealing for grain growth. In the formation of voids which have plane faces, two mechanisms can be operative (an additional mechanism proposed by Stevens *et al.*[27] is discussed in Section 4.5):

(1) Anisotropy of the flow stress which incorporates the cubic crystalline symmetry. Within the core of one individual grain, one has to consider the anisotropy of the yield and flow stress and its effect on the shape of a growing void under an idealized hydrostatic tensile stress. It is well known that both aluminum and nickel have anisotropic tensile (and, as a consequence, compressive) properties. The directions along which the flow stress is minimum should undergo the largest plastic deformation. Figure 55(a) shows the stress–strain curves for aluminum single crystals for [111] and [100] directions of the tensile axis.

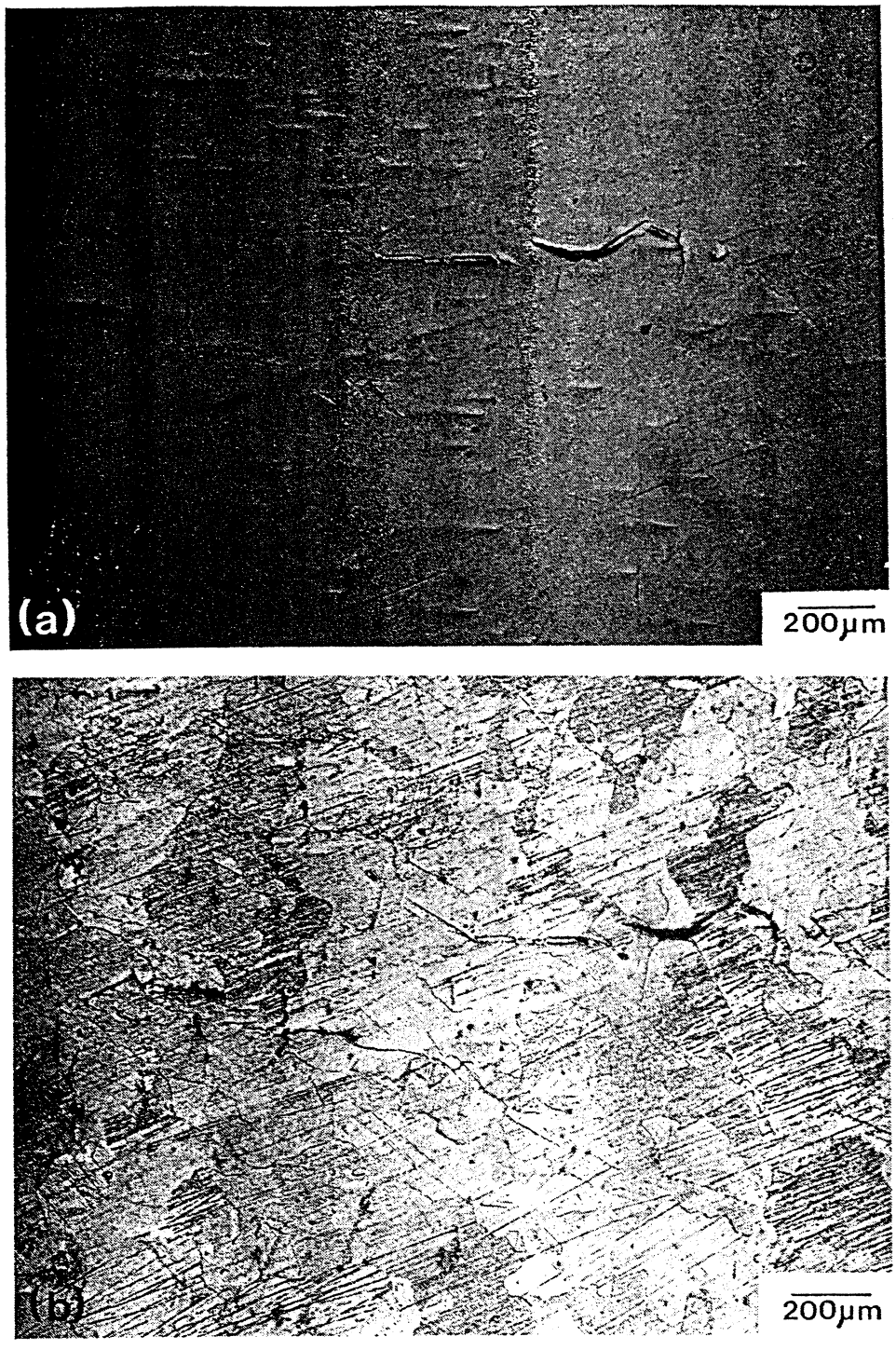

FIG. 52. Incipient spalling in Armco iron. (a) Unetched section showing cracks; (b) etched section of same region showing cracks and grain boundaries. Specimen courtesy of D. A. Shockey, Stanford Research Institute.) (Spec. D.)

The data were generated by Kocks.[118] A stress level of 8 MN m^{-2} produces a strain of 0.04 for ⟨111⟩ and 0.18 for ⟨100⟩. Hence, if one applied a hydrostatic stress to a solid, the ⟨100⟩ would be "softer", and deformation would proceed easier along these axes. The analytical solution of the problem would be of great complexity because it would have to incorporate the work hardening and its effect on the flow stress along the principal crystallographic directions. These anisotropies in plastic response determine the shape of the

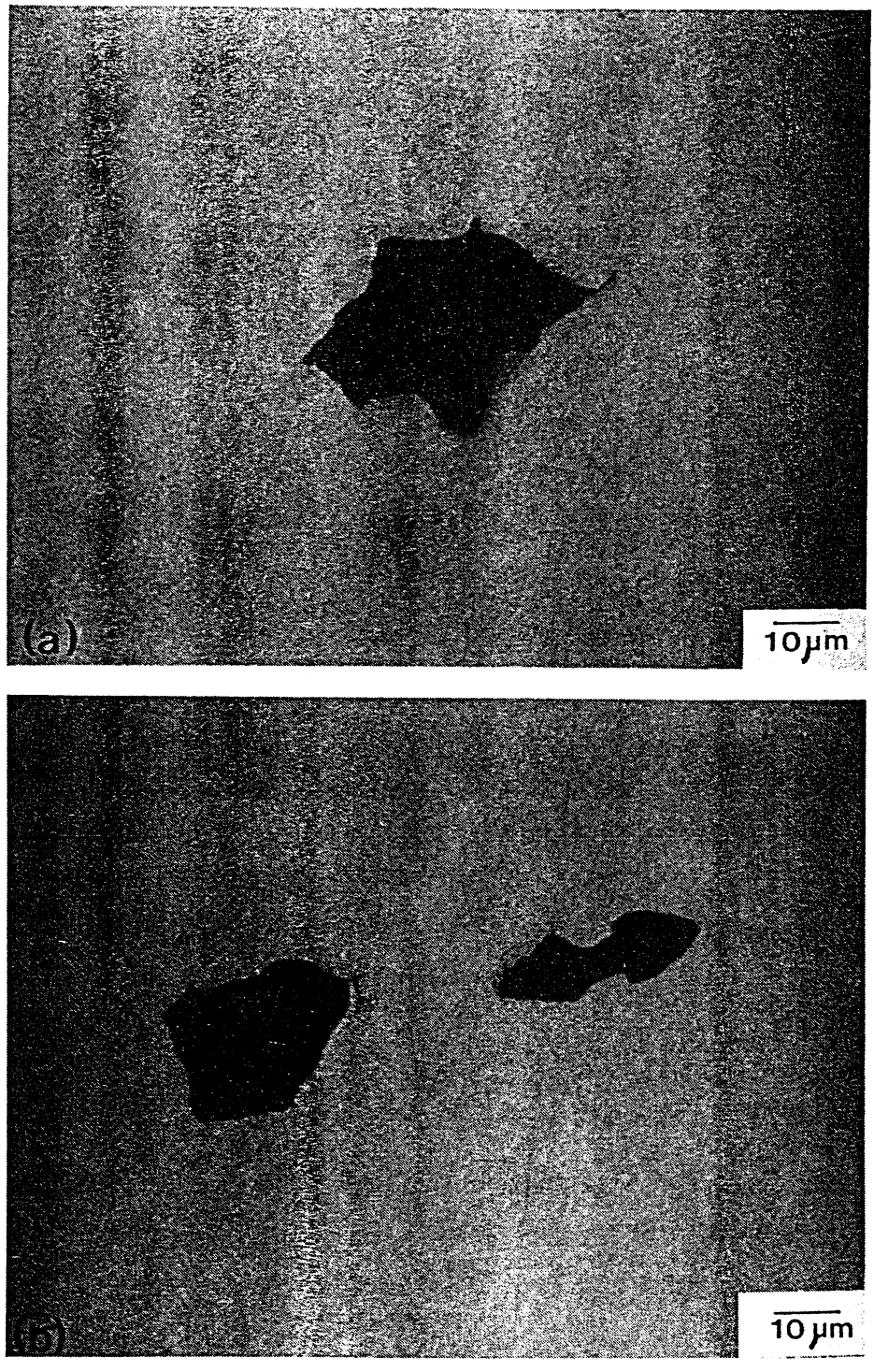

FIG. 53. Geometrically-shaped voids in nickel. (Spec. B.)

growing void. One can clearly see from Fig. 55(b), in which the principal directions are shown, that growth along the axes [100], [010], and [001] is highly favored by the lower yield stress (and flow stress, after a specified amount of plastic deformation).

(2) Anisotropy of the surface energy. If surface energy were isotropic, the favored void shape (which minimizes the surface energy per unit volume) would be the sphere. However, certain planes possess a higher surface energy than others and if one lets the void find its equilibrium shape (neglecting the strength of the matrix or allowing thermally activated

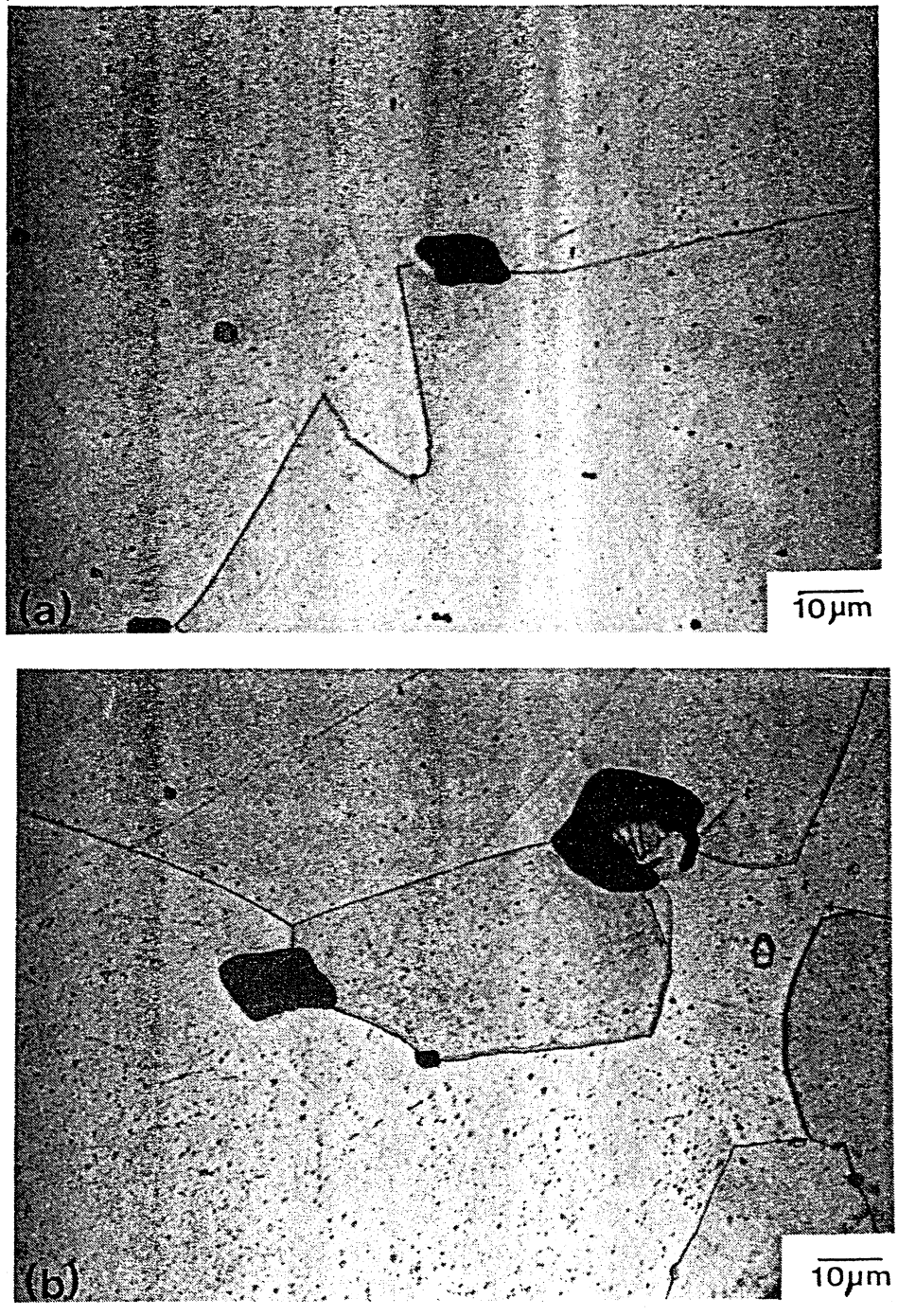

FIG. 54. Voids in nickel after annealing for 1100°C/1 hr. Notice peculiar shape of voids and grain-boundary pinning (during grain growth) by voids. (Spec. B.)

diffusion to take place) it would be a faceted polyhedron, the faces representing planes of minimum energy. Hence, if ⟨111⟩ is the plane with minimum surface energy, one would end up with a cube with ⟨111⟩ faces. One would, of course, have a rounding-off at the edges in order to minimize the overall surface energy.

These two factors above discussed certainly determine the shape of the voids. If plastic deformation generates temperatures at the void surfaces that approach the melting point, a great portion of the strength is lost and the surface energy term plays an important role in

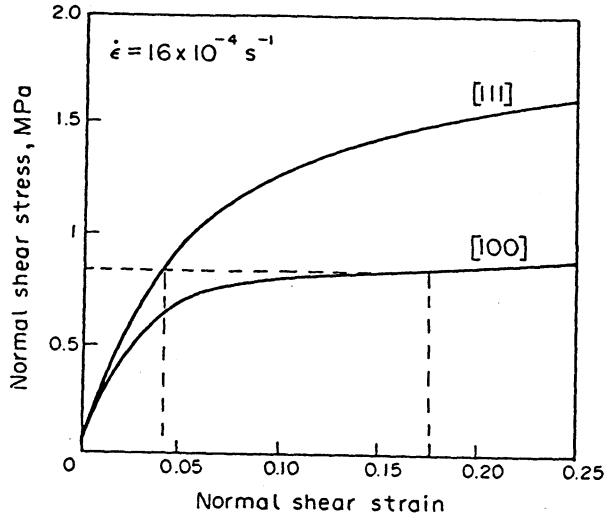

(a)

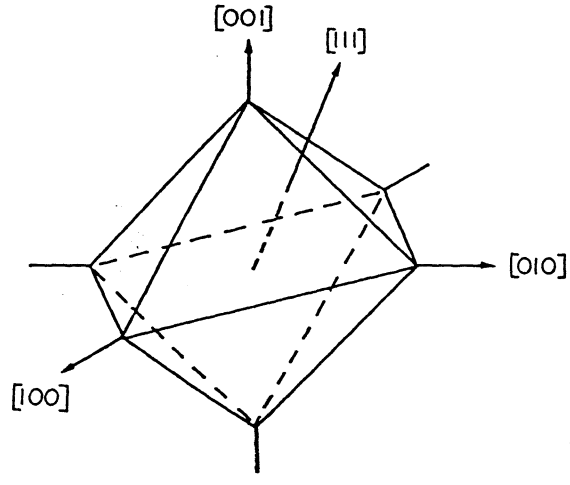

(b)

FIG. 55. (a) Effect of crystalline orientation on stress-strain behavior of aluminum monocrystals. A stress level of 8 MN/m^2 produces a strain of 0.04 along ⟨111⟩ and 0.18 along ⟨100⟩. (Adapted from U.F. Kocks, *Met. Trans.* 1 (1970) 1121, Fig. 16.) (b) Cuboidal void aligned with crystallographic axes.

establishing the equilibrium shape. On the other hand, if the temperature increase is not substantial, the anisotropy of the flow stress dominates and establishes the void size.

Figure 56 shows the appearance of a strip of nickel (taken from the specimen shown in Fig. 8) prior to (left) and after (right) annealing at 1100°C for one hour. The concentration of voids was not changed by the treatment. The dark portion represents the spall region. An effect that was observed was the reduced grain size of the nickel, close to the spall, after annealing (Fig. 57). The reason for this effect is not known, although it is similar to the one observed by Dietrich and Greenhut[54] in copper. They analyzed the structure of shock-loaded copper in regions away and adjoining the maximum tensile pulse region and observed significant changes in the recrystallization pattern (after annealing) and power output in calorimetry. The recrystallized grain size close to the spall was much smaller than away from it. They attributed the reduced grain size to pinning of boundaries due to the voids. In a later study, Greenhut *et al.*[55] looked at the effects of tensile reflected stresses on the

FIG. 56. Photomontages of two strips of shocked (and spalled) nickel. Right-hand side in as-shocked condition; left-hand side after aging at 1100°C/1 hr. (Spec. B.)

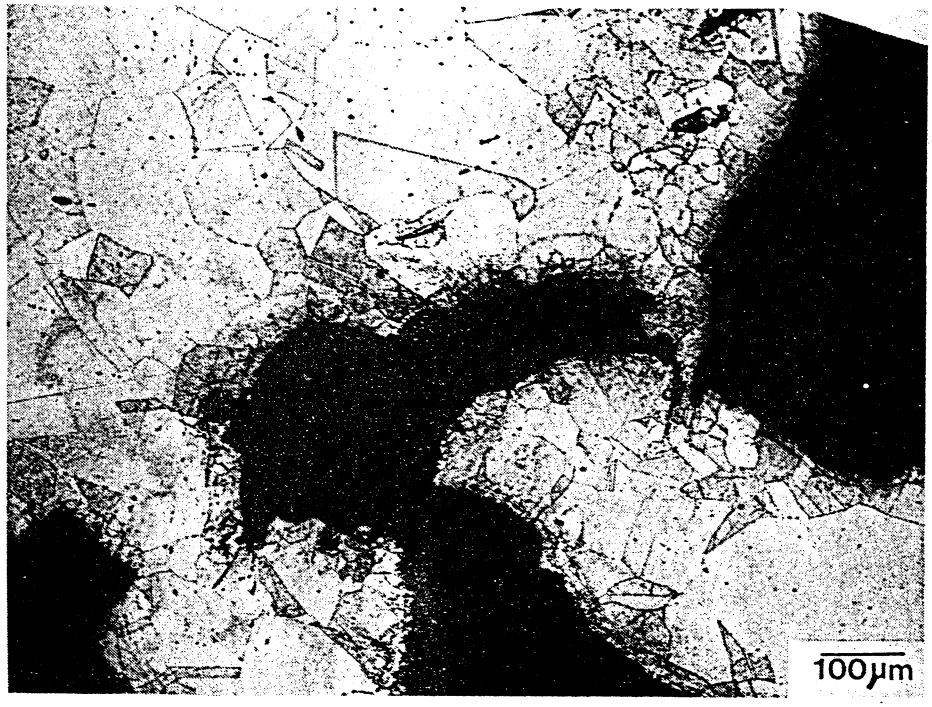

FIG. 57. Grain-size reduction through recrystallization in areas adjoining spall. Nickel annealed at 1100°C for one hour after spalling. (Spec. B.)

post-explosionem aging kinetics of aluminum alloys and found striking differences. The growth of precipitates close to the spall region occurred much faster than away from it; they attributed this effect to an increased vacancy concentration stimulating diffusion.

An attempt has been made by the authors to observe nucleating voids by transmission electron microscopy. Electron-transparent foils were prepared of regions in the high-damage area adjoining the spall, for nickel. However, no voids could be observed. Figure 58 shows transmission electron micrographs of three regions within a spalled specimen. Figure 58(a) represents the region between the spall and the free surface; Fig. 58(b), the region adjoining the spall; Fig. 58(c), the region between the impact surface and the free surface. No distinct differences between the dislocation substructures (ill-defined cells and tangles) are evident, and no voids could be observed, although several foils from close to the spall were observed. These results are in accord with the scanning electron micrographs of Fig. 36, which do not show any signs of large concentrations of voids with very small size. It seems that the voids rapidly grow to observable (by optical techniques) sizes, once formed. However, more systematic investigations are required, correlating the total volume investigated by TEM with the one studied by optical and SEM methods and arriving at quantitative void size distributions extending themselves into the submicronic range. For AISI 1010 steel, the observation of incipient cracks by transmission electron microscopy was also conducted, without success. It is shown in Fig. 59 that cracks are very difficult to observe because of the natural etching tendency of the electrolyte along interfaces, perforating the foil. Similarly, foil fractures could be misconstrued as being spalling microdamage. Hence, it is doubtful whether cracks will eventually be incontrovertibly identified by transmission-electron microscopy. The cracks shown in Fig. 59 are most probably due to etching at energetically favored places. The shock-induced substructure and pearlite colonies can be seen in the same photomicrographs.

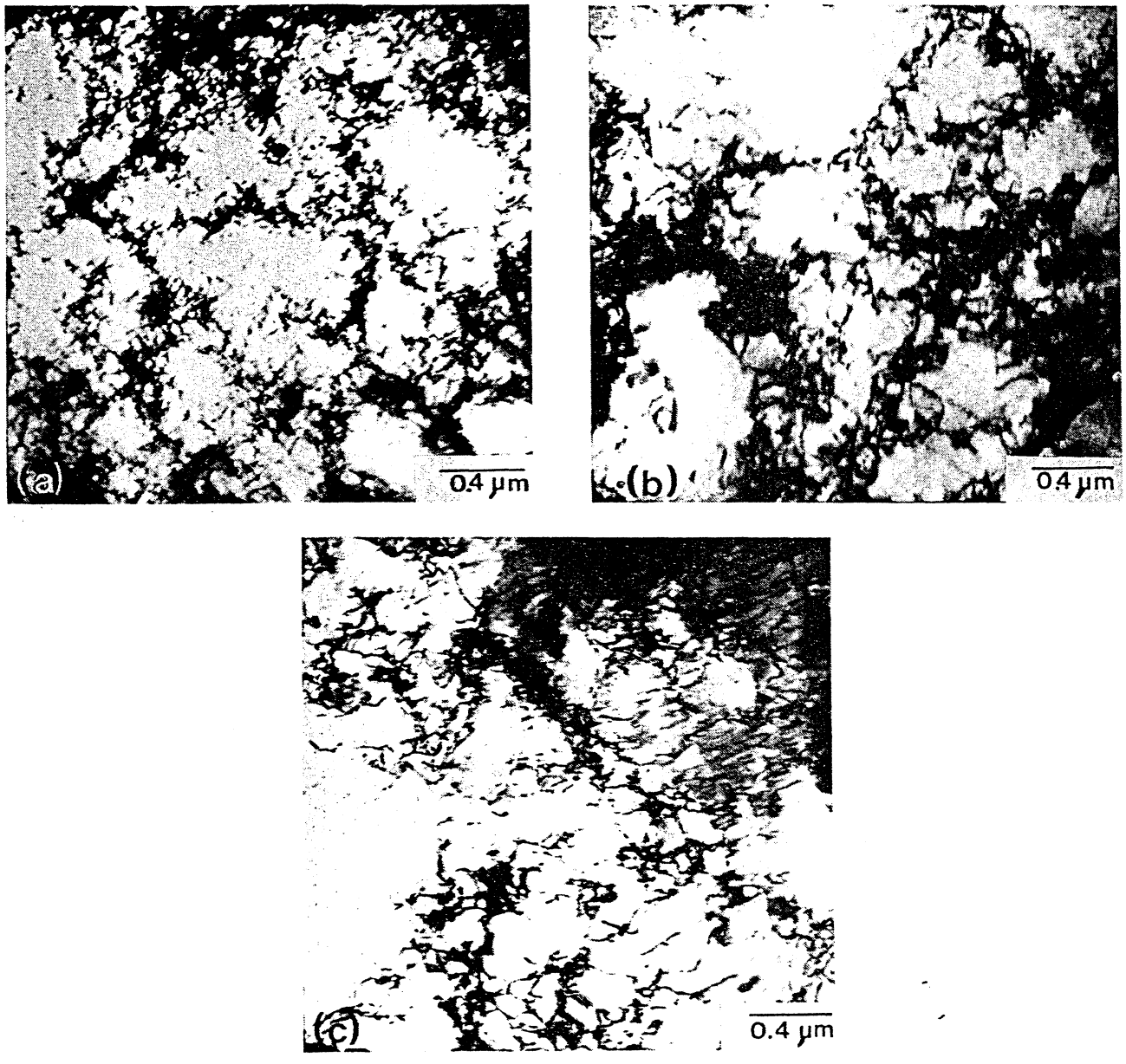

FIG. 58. Transmission electron micrographs of thin foils of nickel; three different positions. (a) Between back surface and spall; (b) close proximity to spall; (c) between spall and impact surface. (Spec. B.)

4.5. *Micromechanical Models*

4.5.1. *The theory of Stevens, Davison and Warren*[27]

There has been only one attempt, to the authors' knowledge, to obtain expressions for the growth of voids from fundamental equations of dislocation theory. Stevens *et al.*[27] proposed, in 1972, a theory for the growth of voids in aluminum monocrystals incorporating dislocation dynamical relations and arriving at a growth law compatible with observed growth rates. The starting point of their theory was the observation that the voids were cuboidal, with the cube diagonal being ⟨100⟩. They attributed the shape of the voids to the glide of dislocations along ⟨111⟩, the planes of the cube faces, away from the void (or towards it, depending upon their sign). Figure 60(a) shows a diametral section of a void

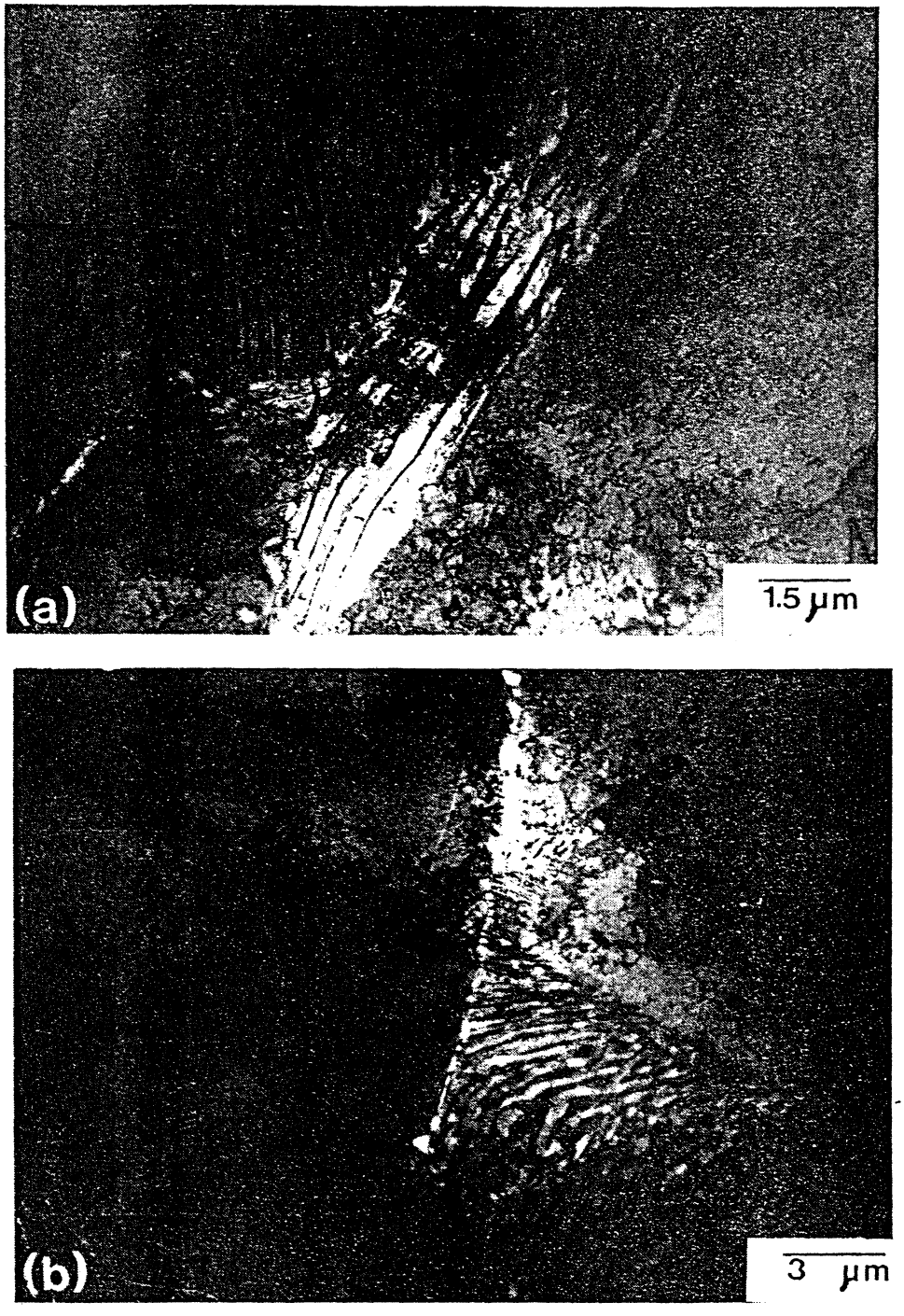

FIG. 59. Transmission electron micrographs thin foils of steel. (a) and (b) are foils taken between back surface and spall (2 mm from back surface). (Spec. A.)

through a (110). Stevens *et al.*[27] say that dislocations can only move into the expanding void in a narrow band near the equatorial edge; i.e. close to M. The detailed view of the edge M, showing the individual positions of the atoms, is seen in Fig. 60(b). The Burgers vector of the edge dislocation shown lies in the plane of the drawing. The arrows show the components of the imposed shear stress that produce the dislocation motion. Since there is already a large density of dislocations in the material, produced by the direct compressive shock wave, Stevens *et al.*[27] propose that the movement of these dislocations towards the

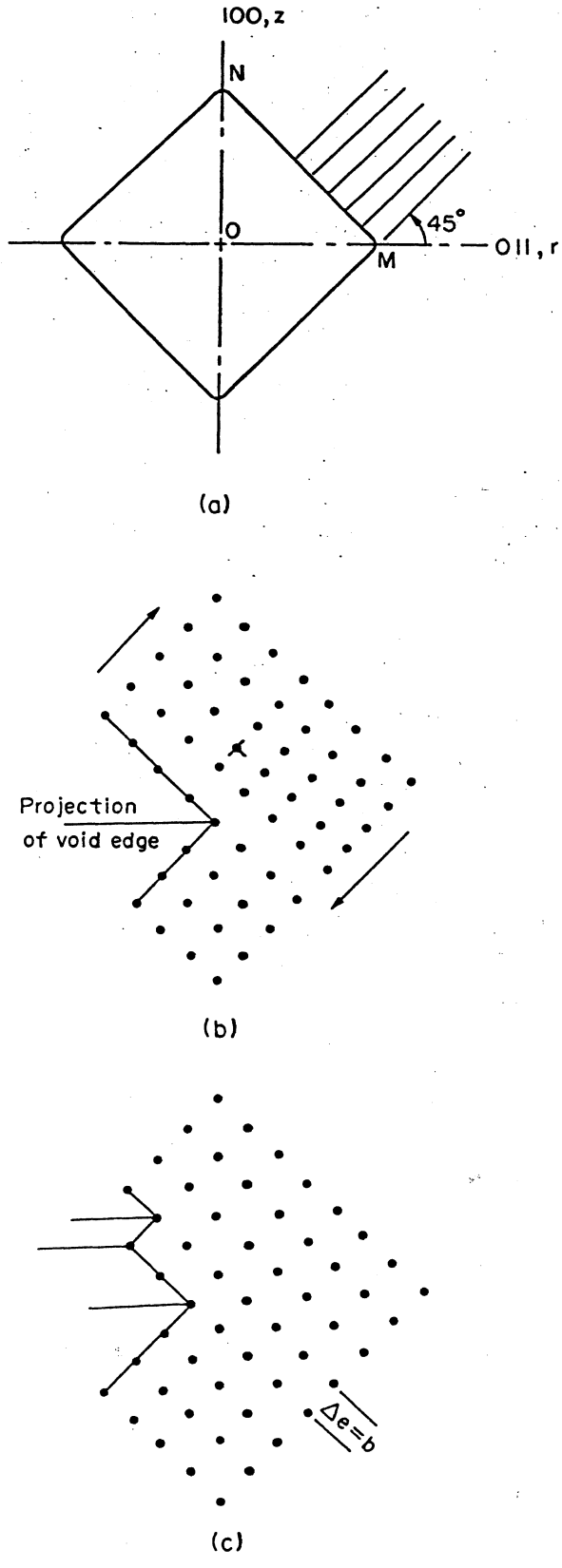

FIG. 60. Stevens, Davison and Warren's mechanism for void growth by dislocation movement. (a) Section of cubical void showing (111) planes making 45° with horizontal planes; (b) dislocation in metal moving under influence of shear stress; (c) after dislocation moves into void step is generated with increase in voids by $e = b$. (From A. L. Stevens, L. Davison and W. E. Warren, *J. Appl. Phys.* 43 (1972) 4922, Figs 3 and 4, respectively.)

void will increase its size. Figure 60(c) shows the change of shape of the void, as the dislocation is incorporated into it. The void wall is moved and the void size is increased, on one side, by $\Delta e = b$. The cuboidal void form is preserved, according to Stevens *et al.*,[27] because dislocations are absorbed onto the void only in a highly localized region near the equatorial edge. This is, in the authors' view, a very unlikely hypothesis, as well as the one saying that dislocations having opposite sign from that shown in Fig. 60(b) and moving away from the void have no influence on its growth, unless they are actually nucleated at the void surface. Stevens *et al.*[27] then equate the volume of an octahedral void to the length of an edge of the void, and the rate of change of the void volume to the rate of change of the length:

$$\dot{V} = 3\left(\frac{\sqrt{2}}{3}\right)^{1/3} V^{2/3}\dot{l} \tag{24}$$

where V and l are the void volume and edge length, respectively. But the rate of increase of the void edge is related to the rate at which dislocations arrive at it. If dislocations intersect the void at a rate N at the neighborhood of each equatorial edge, then each of these edges moves outward at a rate equal to $\frac{1}{2}Nb$, and the rate of change in length of l is:

$$\dot{l} = \dot{N}b \tag{25}$$

Stevens *et al.*[27] applied the equation of dislocation dynamics relating the velocity to the applied stress:

$$v = \frac{b}{B}(\tau - \tau_0) \tag{26}$$

where v is the dislocation velocity, B is a damping constant, τ is the applied shear stress, and τ_0 is the frictional stress. This led to the following expression for the void volume:

$$V = V_0 \exp\left[3A(t - t_0)\right] \tag{27}$$

where V_0 is the void volume at nucleation time, t_0. This equation is similar to the experimental results obtained for 1145 aluminum (polycrystalline) obtained by Barbee *et al.*[119] The authors appreciate the theoretical effort put forward by Stevens *et al.*[27] but disagree from the basic hypothesis. Essentially, the following points contradict Stevens *et al.*[27] theory:

(a) aluminum (and nickel) are high stacking-fault energy materials and the dislocations cross-slip with great ease, blocking each other in the process. It is not possible to have the availability of a great number of edge dislocations at planes that, at the various stages of void growth, intersect the void edges. They would be blocked by cross slip; the dislocation density generated by shock loading is simply not sufficient to feed growing voids if the dislocations have to move reasonably short distances.

(b) The anisotropy of plastic deformation is very marked in aluminum and can easily account for the difference in the rate of deformation along different directions. This is described in greater detail in Section 4.4.

4.5.2. *A proposed model*

A very simplified model for void growth is presented below. It is general in nature and should not be restricted to dynamic growth. Dislocation generation and motion is required

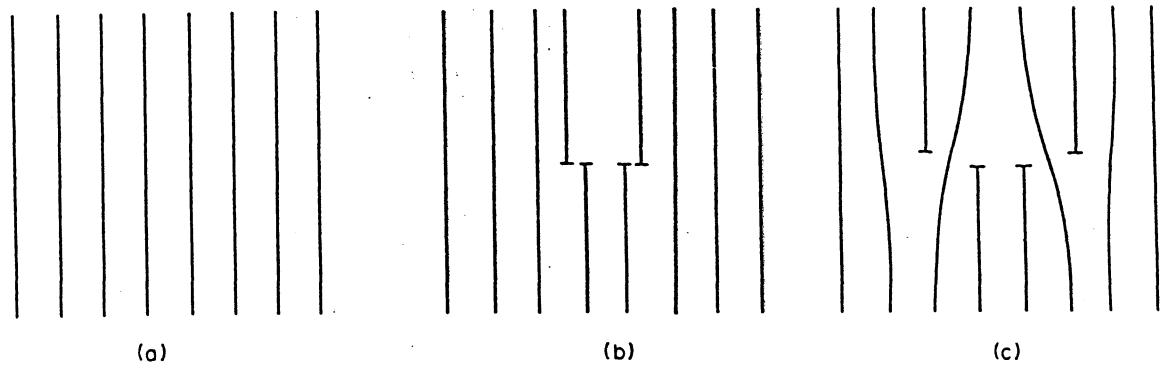

FIG. 61. Production of a row of vacancies by homogeneous nucleation of two edge dislocations and movement in opposite directions.

to effect the production of the void. The basic idea is the same as that used by Ashby[120] in explaining the generation of dislocations in materials containing rigid particles during plastic deformation. Ashby[120] postulated the generation and motion of geometrically-necessary dislocations to explain the strain gradients around rigid particles; the strain at the particle–matrix interface was zero, while in the bulk it was equal to the one imparted to the specimen by the externally-imposed loads. Ashby's dislocation arrays are rather idealized but his approach shows very well in both a qualitative and quantitative fashion how rigid particles contribute to increased work hardening. The same approach will be used here: idealized configurations of dislocations will be assumed for the homogeneous generation of a void. The difference here is that the plastic strain is maximum at the void and zero in the bulk of the crystal; hence, the sense of the plastic strain gradient is inverted. The basic dislocation reaction proposed here is shown in Fig. 61; it consists of the simultaneous separation (homogeneous nucleation) along two adjacent atomic planes. The dislocations move along opposite directions, creating, in the center, the equivalent of a row of vacancies. This reaction starts at a certain point and spreads lengthwise, as shown in the top view of Fig. 62. The spreading sequence is shown in three stages; these correspond to the three stages of Fig. 61. Figure 63 shows the two edge segments formed; they are connected to the original planes by screw segments (***b*** parallel to dislocation line). Obviously one such dislocation doublet is not sufficient for the generation of a void. It produces a region which can be taken as a vacancy line of length L. Figure 64 shows how a void can be produced by this mechanism. Along four slip planes intersecting along a line, doublets are produced and the edge segments are driven outwards.

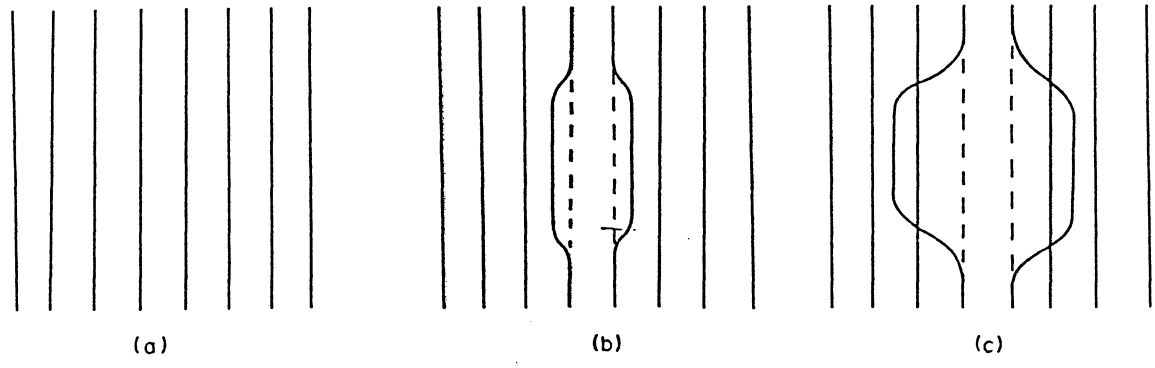

FIG. 62. Same sequence as in Fig. 61, viewed from top.

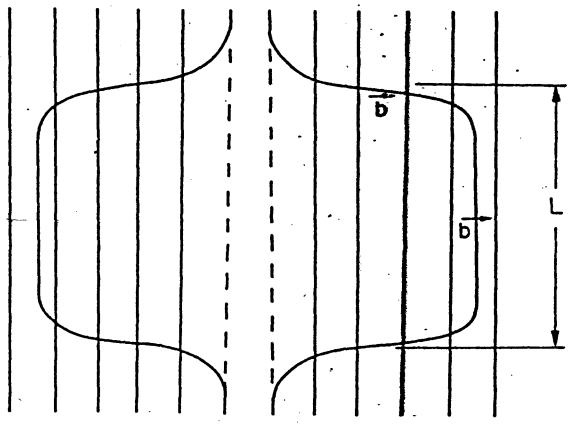

FIG. 63. Formation of vacancy row of length L by movement of dislocation segments of length L in opposite directions.

The vacancy beads formed in the internal part are assumed to agglomerate and form a void, because this is energetically more favorable. Assuming that each vacancy has a volume of b^3, a dislocation line of length L will produce a void volume of b^3L. This equation relates dislocation length to void volume and is important in the development of the model.

FCC metals have four slip planes, with three slip directions in each. Hence, we can assume twelve groups of dislocation doublets per space point. From this we can calculate the volume of void generated in a point. This volume establishes the length L of the edge segment.

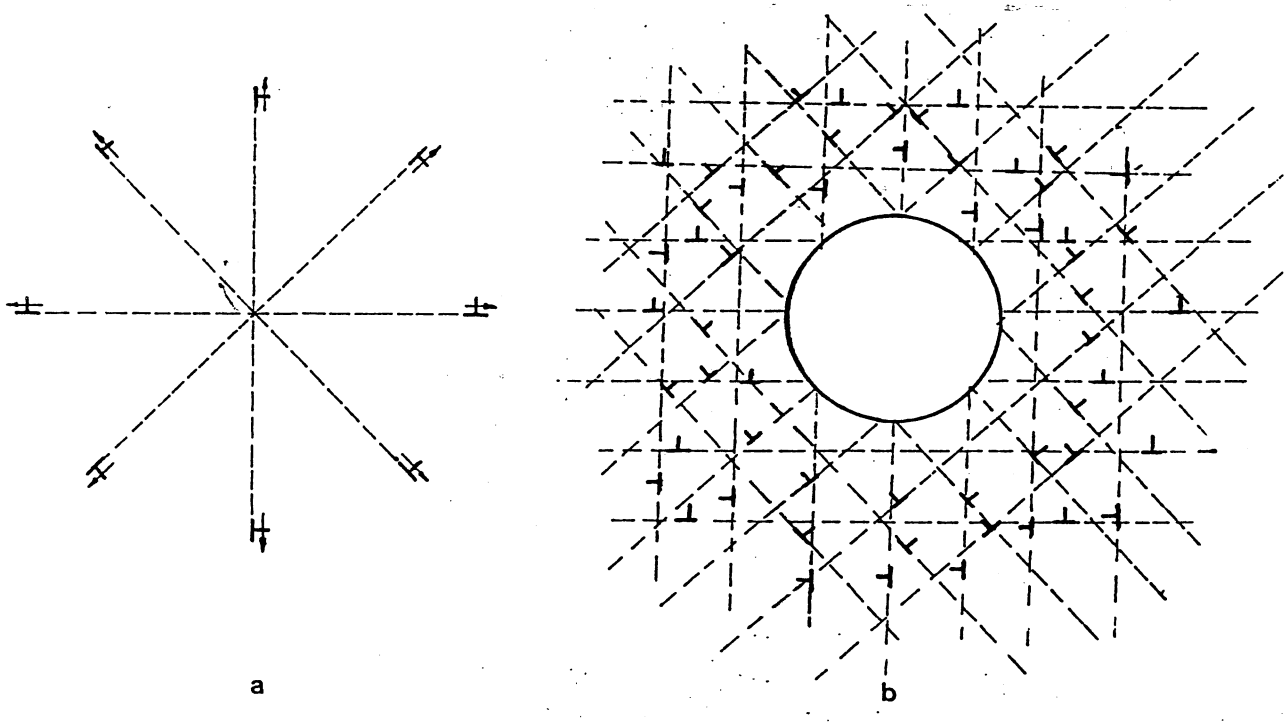

FIG. 64. (a) Mechanism of formation of vacancy rows on four slip planes. (b) Formation of vacancy rows on four sets of parallel slip planes and their agglomeration into a void.

$$12b^3L = \tfrac{4}{3}\pi R^3 = \tfrac{4}{3}\pi\left(\frac{L}{2}\right)^3 \tag{28}$$

Hence,

$$L = 8.3b^{3/2}. \tag{29}$$

Figure 64(b) shows how the operation of dislocations on parallel planes can produce a larger void. The total Burgers vector is equal to zero, as can be seen by making a Burgers circuit around the void; hence no macroscopic strain is involved. A number of sources in four parallel planes, along three directions in each plane, generate the vacancies that will form the central void. The outward driving force for the dislocation motion is given by the stress gradient set up by the void and the hydrostatic stress at infinity. The stresses at the surface of the void are zero and in this way a gradient is established. The criterion for the

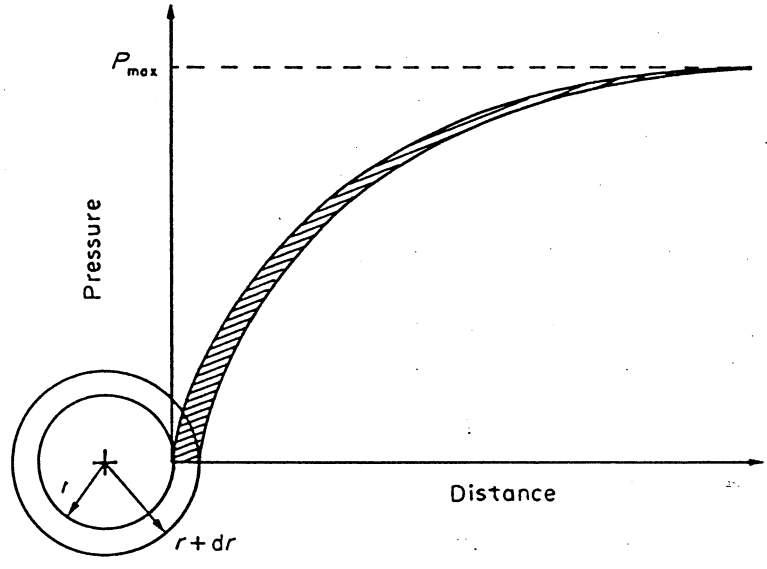

FIG. 65. Stress relaxation in proximity of void and its variation with the increase of size of void; cross-hatched area represents deformation energy gained by increase in void radius from r to $r + dr$.

void growth is similar to the one introduced by Griffith for crack growth. An energy balance equation is set up in order to obtain a criterion for growth. The elastic energy (E_e) stored around the void is released by its growth. Assuming a hydrostatic state of stress, the amount of energy released is shown in Fig. 65. When the void radius increases from r to $r + dr$ the energy released is given by the cross-hatched difference between the two curves shown in Fig. 65. The exact shape of the stress change curve gives the amount of energy released. This released energy is balanced by three energy gains: energy required to form the new surface (E_s), deformation energy due to the dislocations generated (E_d), and thermal energy (E_T) due to the heat generated by the movement of dislocations.

$$E_e = E_d + E_s + E_T \tag{30}$$

By inserting appropriate expressions for these four energy terms, it is possible to arrive at an equation describing the rate of growth. If geometrical similarity of the stress field is maintained, the rate of hydrostatic stored elastic energy released increases with void size.

5. Conclusions and Recommendations

A major portion of the work conducted with the purpose of developing an improved understanding of the mechanisms involved in dynamic fracture produced by the interactions of waves is reviewed. Although the main thrust for research in this field has been its military application, it is also important in areas such as the impact of cosmic particles with space vehicles and the fragmentation of rocks for mineral and oil extraction. The basic wave interactions involved in spalling are presented. A great portion of the research was conducted at Stanford Research Institute, Sandia National Laboratories, and Los Alamos National Laboratories; their work is described. The important conceptual advances are highlighted. They are the concept of a damage function introduced by Davison and Stevens,[26,30] the equations describing the nucleation and growth rates of flaws developed by the S.R.I. group (Curran, Seaman and Shockey, principally) and incorporated into computer codes, as well as Grady's[31] generalized formulation for fragment size determination based on energy blance equations. A discussion on the theoretical aspects of the dynamics of crack and void growth is presented. Computer codes that have been developed to predict the extent of damage and describe a number of dynamic phenomena are briefly discussed. They constitute a powerful research tool and will certainly play a growingly important role in the improved understanding of dynamic fracture. The metallurgical aspects of spalling are then discussed in detail, with ample pictorial illustrations of a number of effects. The nucleation and growth of voids and cracks is illustrated and the effects of metallurgical parameters on them are discussed. The rough and smooth spalls in steel are described, as well as cuboidal void growth; speculative mechanisms for their formation are presented. A micromechanical model for the growth of voids is discussed. Throughout the monograph, critical assessments are made of the areas requiring further research effort. The general conclusion by the authors in this regard are the areas requiring further research:

(i) The effects of the classical metallurgical variables have not been systematically evaluated. These are: grain size, stacking-fault energy, existence and size of second phases (precipitates, inclusions), pre-strain, texture, solid solution atoms.
(ii) Observation of the first stages of void growth by advanced metallographic techniques (mainly, transmission electron microscopy) and development of detailed model for void growth by dislocation generation and movement.
(iii) Verification of the role (if any) played by vacancies in spalling and determination of vacancy concentration along the spall region as well as away from it.
(iv) Systematic investigations including critical experiments to determine the origin of rough-to-smooth spall transition in iron and steel.

This view is corroborated by recommendations made by Davison and Graham[1] and by the committee on Materials Response to Ultra-High Loading Rates established by the National Materials Advisory Board (National Academy of Sciences) and chaired by Dr. W. Herrmann.[9] These recommendations are transcribed here, in order to put in focus the knowledge gaps in the area.

Davison and Graham[1] state:

"The state of knowledge of spall phenomena can be summarized by saying that much practical information is available and pragmatic understanding is well advanced but almost nothing fundamental is known about either the nucleation or late growth stages of the process and much remains to be learned about the early growth phase." They further

recommend that "viscous heating and heating in the growth of voids and cracks in which plastic deformation is involved should be studied in greater detail," and state that the "effect of variations in microstructural parameters is almost unknown".

The committee on Materials Response to Ultra-High Loading Rates recommends "continuation of research into mechanisms of dynamic crack nucleation and growth", but recognizes "the need for and acceleration of research into the mechanisms of dynamic crack interaction and coalescence in order to complete the description of brittle failure under dynamic loading. The theoretical effort to describe the mechanics of crack interaction and coalescence should be accompanied by a continuation of experimental programs in which dynamically loaded specimens are carried through to compete fragmentation in order to extend the data based for comparison with theory". For dynamic void growth, the NMAB committee recommends "continuation of current search in ductile fracture under quasi-static conditions, together with increased effort on dynamic ductile fracture. Such a research program should focus on an identification of the mechanics of void nucleation, growth and coalescence, and the extension of ductile cracks".

ACKNOWLEDGEMENTS

The decision to write this monograph grew from discussions held with the Stanford Research Institute group. In this regard, we are very appreciative of the input provided by Dr D. A. Shockey, Mr P. S. DeCarli and Mr D. C. Erlich.

The help of Mr Drew Courtright in the preparation of the specimens and optical microscopy and of Mrs K. Couch Robino in electron microscopy is gratefully acknowledged. Dr J. F. Figueiró provided valuable help in the later stages of this investigation. The explosive events were conducted with the assistance of the TERA (Terminal Effects Research and Analysis) group of New Mexico Tech. Financial support during the preparation of this manuscript was provided by NSF grant DMR 8115127 and by the Research and Development Division of New Mexico Tech., through the kind assistance of its director, Dr Marx Brook.

REFERENCES

1. L. DAVISON and R. A. GRAHAM, *Phys. Rep.* **55** (1979) 257.
2. G. L. MOSS, In *Shock Waves and High-Strain Rate Phenomenon in Metals: Concepts and Applications*, (eds. M. A. Meyers and L. E. Murr) Plenum Press, New York (1981) p. 299.
3. H. C. ROGERS, *A. Rev. Meter. Sci.*, **9** (1979) 283.
4. M. A. MEYERS and L. E. MURR, eds., *Shock Waves and High-Strain Rate Phenomena in Metals: Concepts and Applications*, Plenum Press, New York (1981).
5. D. GRADY, source cited in ref. 4, p. 181.
6. A. S. ABOU-SAYED, R. J. CLIFTON and L. HERMANN, *Exp. Mech.*, (1976) 127.
7. P. C. CHOU and A. K. HOSKINS, eds., *Dynamic Response of Materials to Impulsive Loading*, Air Force Materials Laboratory, WPAFB (1972).
8. W. HERRMANN and J. W. NUNZIATO, source cited in ref. 7, p. 123.
9. NATIONAL MATERIALS ADVISORY BOARD, *Materials Response to Ultra-High Loading Rates*, NMAB-356 (1980).
10. B. HOPKINSON, *Trans. R. Soc. (Lond.)*, **213A** (1914) 437.
11. B. HOPKINSON, *Brittleness and Ductility*, In *Scientific Papers*, p. 64, Cambridge U. Press, London (1910).
12. J. S. RINEHART, source cited in ref. 4, p. 8.
13. N. F. MOTT, *Proc. R. Soc. (Lond.)*, **300** (1947) 300.
14. J. W. ZANDON, *Proc. R. Soc. (Lond.)*, **103A** (1923) 622.
15. R. M. DAVIES, *Trans. R. Soc. (Lond.)*, **240A** (1948) 375.
16. J. S. RINEHART, *J. Phys.*, **22** (1951) 131.

17. J. S. RINEHART, *J. Phys.*, 23 (1952) 1229.
18. I. C. SKIDMORE, *Appl. Mater. Res.* 4 (1965) 131.
19. B. R. BREED, C. L. MADER and D. VENABLE, *J. Appl. Phys.* 38 (1967) 3271.
20. C. S. SMITH, *Trans TMS-AIME* (1958) 574.
21. R. G. MCQUEEN and S. P. MARSH, *J. Appl. Phys.* 27 (1956) 1484.
22. J. N. JOHNSON, *J. Appl. Phys.* 52 (1981) 2812.
23. B. M. BUTCHER, L. M. BARKER, D. E. MUNSON and C. D. LUNDERGRAN, *AIAA Journal* 2 (1964) 977.
24. F. R. TULER and B. M. DAVIES, *Trans. R. Soc. (Lond.)*, 240A (1948) 375.
25. A. L. STEVENS and F. R. TULER, *J. Appl. Phys.*, 42 (1971) 5665.
26. L. DAVISON and A. L. STEVENS, *J. Appl. Phys.* 43 (1972) 988.
27. A. L. STEVENS, L. DAVISON and W. E. WARREN, *J. Appl. Phys.* 43 (1972) 4922.
28. A. L. STEVENS and L. E. POPE, In *Metallurgical Effects at High Strain Rates*, (eds. R. W. Rohde, B. M. Butcher, J. R. Holland and C. H. Karnes) Plenum Press, New York (1973) p. 459.
29. L. DAVISON, A. L. STEVENS and M. E. KIPP, *J. Mech. Phys. Solids* 25 (1977) 11.
30. L. DAVISON and A. L. STEVENS, *J. Appl. Phys.* 44 (1973) 668.
31. D. GRADY, *J. Appl. Phys.* 53 (1981) 322.
32. D. A. ERLICH, D. C. WOOTEN and R. C. CREWDSON, *J. Appl. Phys*, 42 (1971) 5495.
33. D. R. CURRAN, In *Shock Waves and the Mechanical Properties of Solids*, (eds. J. J. Burke and V. Weiss) Syracuse U. Press, New York, 1971, p. 121.
34. T. W. BARBEE, L. SEAMAN, R. CREWDSON and D. CURRAN, *J. Mater. JMLSA*, 7 (1972) 393.
35. L. SEAMAN, D. A. SHOCKEY and D. R. CURRAN, In *Dynamic Crack Propagation*, (ed. G. C. Sih) Noordhoff, Leyden, (1973) p. 629.
36. D. R. CURRAN, D. A. SHOCKEY and L. SEAMAN, *J. Appl. Phys.* 44 (1973) 4025.
37. D. A. SHOCKEY, L. SEAMAN and D. R. CURRAN, source cited in ref. 28, p. 473.
38. L. SEAMAN, D. R. CURRAN and D. A. SHOCKEY, *J. Appl. Phys.* 47 (1976) 4814.
39. D. R. CURRAN, L. SEAMAN and D. A. SHOCKEY, *Physics Today*, Jan. (1977) 46.
40. D. A. SHOCKEY, K. C. DAO and R. L. JONES, In *Mechanisms of Deformation and Fracture*, (ed. K. E. Easterling) Pergamon Press, Oxford (1977) p. 77.
41. D. A. SHOCKEY, D. R. CURRAN and L. SEAMAN, In: *High Velocity Deformation of Solids*, (eds. K. Kawata and J. Shiori) Springer-Verlag, Berlin (1979), p. 149.
42. L. SEAMAN, D. R. CURRAN and R. C. CREWDSON, *J. Appl. Phys.* 49 (1978) 5221.
43. D. R. CURRAN, L. SEAMAN and D. A. SHOCKEY, source cited in ref. 4, p. 129.
44. G. L. MOSS and L. SEAMAN, *Mechanics of Materials*, to be published, 1982.
45. K. TAKAHASHI, *J. Macromol. Sci.—Phys.* B8 (1973) 673.
46. Y. MARON and A. E. BLAUGRUND, *J. Appl. Phys.* 53 (1982) 356.
47. R. DORMEVAL, J. M. CHEVALLIER and M. STELLY, *Proc. Fifth Intl. Conf. Fracture*, Cannes, 1981.
48. W. S. DE ROSSET, *Coalescence of Cavities during Dynamic Fracture*, BRL Report No. 1631, Aberdeen Proving Ground, MD, 1973.
49. R. L. Warnica, *Spallation Thresholds of S-200 Beryllium, ATJ-S Graphite and Isotropic Boron Nitride at 75°F, 500°F and 1000°F*, Report MSL-68-18, General Motors Corporation, Materials and Structures Laboratory, 1968.
50. L. V. ALTSHULER, S. A. NOVIKOV and I. I. DIVNOV, *Sov. Phys. Dokl.*, 11 (1966) 79.
51. W. B. JONES, *Effects of Solid State Precipitation on Dynamic Fracture*, M.Sc. Thesis, U. of Washington, 1973.
52. W. B. JONES and H. I. DAWSON, source cited in ref. 28, p. 443.
53. S. E. AXTER, W. B. JONES and D. H. POLONIS, *Metallography*, 8 (1975) 425.
54. A. M. DIETRICH and V. A. GREENHUT, source cited in ref. 28, p. 645.
55. V. A. GREENHUT, M. G. CHEN, R. BANKS and S. GOLASKI, *Long-Range Diffusion of Vacancies and Substitutional Atoms During High-Strain-Rate Deformation of Aluminum Alloys*, Proc. ICMII, Boston, Mass, 1975.
56. L. E. MURR, *J. Appl. Phys.* 47 (1976) 1364.
57. W. MOCK, JR and W. H. HOLT, *J. Appl. Phys.* 53 (1982) 5660.
58. J. H. SMITH, In: *Dynamic Behavior of Materials*, ASTM, Philadelphia, PA (1963)p. 264.
59. D. W. BLINCOW and D. V. KELLER, source cited in ref. 58, p.
60. J. BUCHANAN and H. JAMES, *Br. J. Appl. Phys.* 10 (1959) 290.
61. W. J. NELLIS, L. SEAMAN and R. A. GRAHAM, *Shock Waves in Condensed Matter—1981*, Am. Inst. of Phys., New York (982).
62. D. L. WESENBERG and M. J. SAGARTZ, *J. Appl. Mech.* 44 (1977) 643.
63. J. J. GILMAN and F. R. TULER, *Int. J. Fract. Mech.*, 6 (1970) 169.
64. F. R. TULER and B. M. BUTCHER, *Int. J. Fract. Mech.*, 4 (1968) 431.
65. R. T. DEHOFF and R. N. RHINES, eds., *Quantitative Microscopy*, McGraw-Hill, N.Y. 1968.
66. S. N. ZHURKOV, *Int. J. Fract. Mech.* 1 (1965) 311.
67. R. RAJ and M. F. ASHBY, *Acta Met.* 23 (1975) 653.
68. R. W. HERTZBERG, *Deformation and Fracture Mechanics of Engineering Materials*, J. Wiley (1976) pp. 273, 341.

69. F. A. McClintock, In: *Fracture Mechanics of Ceramics*, Vol. 1, (eds. R. C. Bradt, D. P. H. Hasselman and F. F. Lange) Plenum Press (1973) p.
70. M. Wilkins, In: *Methods in Computational Physics*, Vol. 3 (eds., B. Alder, S. Fernbach and M. Rotenberg) Academic, New York (1964) p. 211.
71. M. M. Carrol and A. C. Holt, *J. Appl. Phys.* 43 (1972) 1626.
72. L. S. Costin, J. Duffy and L. B. Freund, *Fracture Initiation in Metals under Stress Wave Loading Conditions*, Brown University Technical Report NSF EnG 75-09612/1.
73. E. Yoffé *Phil. Mag.* 42 (1951) 739.
74. G. C. Sih, Dynamic Aspects of Crack Propagation, In: *Inelastic Behavior of Solids* (eds. M. F. Kanninen, W. F. Adler, A. R. Rosenfield and R. I. Jaffee) McGraw-Hill, New York (1970) p. 607.
75. F. Erdogen, Crack-Ppropagation Theories, In: *Fracture* vol. II (ed. Liebowitz) Academic Press, New York (1968) p. 497.
76. T. L. Paxson and R. A. Lucas, An Experimental Investigation of the Velocity Characteristics of a Fixed Boundary Fracture Model, In: *Dynamic Crack Propagation* (ed. G. S. Sih) Noordhoff Publ. Leyden (1973) p. 415.
77. K. B. Broberg, On Dynamic Crack Propagation in Elastic-Plastic Media, source cited in ref. 76, p. 461.
78. J. Congleton, Practical Applications of Crack-Branching Measurements, source cited in ref. 76, p. 427.
79. S. Winkler, D. A. Shockey and D. R. Curran, *Int. J. Fract. Mech.* 6 (1970) 151.
80. D. R. Curran, D. A. Shockey and S. Winkler, *Int. J. Fract. Mech.* 6 (1970) 271.
81. F. A. McClintock, *J. Appl. Mech.* 35 (1968) 363.
82. F. A. McClintock, *Int. J. Fract. Mech.* 4 (1968) 101.
83. J. R. Rice and D. M. Tracey, *J. Mech. Phys. Solids* 17 (1969) 201.
84. A. Needleman, *J. Appl. Mech.* 39 (1972) 964.
85. J. F. Knott, *Fundamentals of Fracture Mechanics*, Butterworth, London (1973) p. 206.
86. E. B. Glennie, *J. Mech. Phys. Solids*, 20 (1972) 415.
87. R. Karpp and P. C. Chou, In: *Dynamic Response of Materials to Impulsive Loading* (eds, P. C. Chou and A. K. Hoskins) Air Force Materials Laboratory, WPAFB (1972) p. 283.
88. E. Kipp and R. J. Lawrence, WONDY—One-Dimensional Finite Difference Wave Propagation Code, SAND81-0930, Sandia Laboratories, Albuquerque, June 1982.
89. J. W. Swegle, TOODY IV—A Computer Program for Two-Dimension Wave Propagation, SAND-78-0552, Sandia Laboratories, Albuquerque, September 1978.
90. L. Seaman, SRI-PUFF3, Computer Code for Stress Wave Propagation, Technical Report No. AFWL-TR-70-51, Air Force Weapons Lab., Albuquerque, September 1970.
91. M. Wilkins, Calculation of Elastic-Plastic Flow, VCRL-7322, Rev. I, Lawrence Radiation Laboratory, Livermore, 1969.
92. L. M. Barker, SWAP-7, A Stress-Wave Analyzing Program, SC-RR-67-143, Sandia Laboratories, Albuquerque, April 1967.
93. L. M. Barker, SWAP-9; An Improved Stress-Wave Analyzing Program, SC-RR-69-233, Sandia Corporation, Albuguerque, August, 1969.
94. R. Hoffman, STEALTH, A Lagrangian Explicit Finite Difference Code for Solids, Structural and Thermo-hydraulic Analysis, EPRI-NP-176-1, Science Applications, Inc., April 1978.
95. S. L. Thompson, CSQII-A Eulerian Finite Difference Program for Two-Dimensional Material Response, Part I Materials Section, SAND 77-1339, Sandia Laboratories, Alb., May 1981.
96. J. G. Trulio, Theory and Structure of the AFTON Codes, AFWL TR66-19, Air Force Weapons Lab, Albuquerque, June 1966.
97. A. A. Amsden, H. M. Ruppel and C. W. Hirt, SALE: A Simplified ALE Computer Program for Fluid Flow at all Speeds, LA-8095, VC-32, Los Alamos, 1980.
98. J. Von Neuman and R. D. Richtmyer, *J. Appl. Phys.* 21 (1950) 232.
99. J. O. Erkman and A. B. Christensen, *J. Appl. Phys.* 38 (1970) 5395.
100. D. R. Curran, *J. Appl. Phys.* 34 (1963) 2677.
101. D. A. Shockey, D. R. Curran, L. Seaman, J. T. Rosenberg and C. F. Peterson, *Int. J. Rock Mech. Min. Sci. Geomech. Abstr.*, 11 (1974) 303.
102. S. L. McHugh, D. R. Curran and L. Seaman, The NAG-FRAG Computational Fracture Model and Its Use For Simulating Fragmentation and Fracture, Society for Experimental Stress Analysis, Ft. Lauderdale, Fl. 1980.
103. T. F. Adams, J. K. Dienes and A. G. Margolin, The Use of Scalar and Tensor Fracture Models to Calculate Explosive Rock Breakage, Society for Experimental Stress Analysis, Fort Lauderdale, Fla., 1980.
104. J. K. Dienes, *21st Symp. Rock Mech., M.I.T.*, 1981, p. 164.
105. D. E. Maxwell, The CAVS Tensile Failure Model, SATR-79-4, Science Applications Inc., April 1979.
106. T. G. Barbour and K. K. Waki, Prediction of Fragmentation Using CAVS, Society for Experimental Stress Analysis, Fort Lauderdale, Florida, 1980.
107. J. A. Zukas, T. Nicholas, H. F. Swift, L. B. Greszcuk and D. R. Curran, *Impact Dynamics*, J. Wiley, New York (1982).

109. M. E. DE MORTON, R. L. WOODWARD and J. M. YELLUP, *Proc. Fourth Tewksburg Symposium*, Melbourne, February, 1979, p. 11.1.
110. J. O. ERKMAN, *J. Appl. Phys.* **31** (1961) 939.
111. P. S. DE CARLI and M. A. MEYERS, source cited in ref. 4, p. 341.
112. E. E. BANKS, *J.I.S.I.*, **206** (1968) 1022.
113. W. E. DRUMMOND, *J. Appl. Phys.*, **28** (1957) 998.
114. L. M. BARKER and R. E. HOLLENBACH, *J. Appl. Phys.* **45** (1974) 4872.
115. A. G. IVANOV and S. A. NOVIKOV, *J. Exp. Theor. Phys.* (*USSR*) **40** (1961) 1880.
116. A. S. BALCHAN, *J. Appl. Phys.* **34** (1963) 241.
117. M. A. MEYERS, C. SARZETO and C.-Y. HSU, *Met. Trans.* **11A** (1980) 1737.
118. U. F. KOCKS, *Met. Trans.* **1** (1970) 1121.
119. T. BARBEE, L. SEAMAN and R. C. CREWDSON, Air Force Weapons Laboratory, Technical Report No. AFWL-TR-70-99, 1970.
120. M. F. ASHBY, The Deformation of Plastically Non-Homogeneous Alloys, In: *Strengthening Methods in Crystals* (eds A. Kelly and R. B. Nicholson) J. Wiley, New York (1971) p. 137.

ADDENDUM

Whilst this manuscript was being typeset, two additional foci of research (USSR and Lawrence Livermore Laboratory) were identified. Dr. Pierre Lalle (French Atomic Energy Commission) provided valuable help.

a.1 *Soviet Work*

The recent review by Novikov[a-1], although limited in scope and coverage, describes some of the Soviet work on spalling. Twenty references were collected from this and other papers (a-1 through a-20) and they indicate that considerable effort has been devoted by the Soviets to spalling. Novikov has been involved in a significant portion of this work (refs a-1, a-5, a-6, a-8, a-9, a-18). The approach favored by Novikov is the use of explosives. In the review, he recognizes the importance of both time and stress and describes a model for spalling. Using contact explosives detonating at a grazing incidence with a metal and generating saw-tooth shaped pulses in the latter, he observes that the spall damage increases with the decreasing slope of the release part of the wave. The spall threshold is determined by visual examination. The results are shown in Fig. a-1; as the slope of the release portion of the wave decreases the critical stress decreases. This is to be expected, because greater time is allowed at stresses

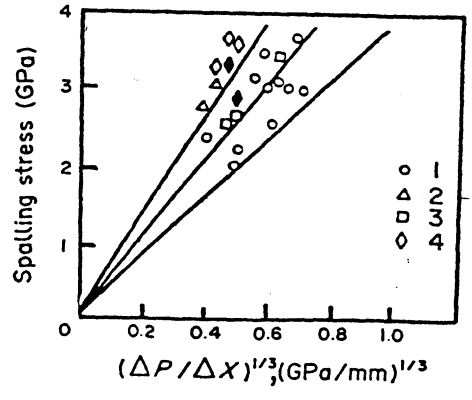

FIG. a-1. Relationship between the slope of the release portion in saw-shaped pulse and the critical stress for spalling for (1) aluminum alloy AMts, (2) aluminum alloy AMg, (3) alloy D16 (annealed), (4) alloy D16 (quenched). (From S. A. Novikov, *J. Appl. Mech. Tech. Phys.*, **22** (1981) 385, Fig. 2.)

below the peak stress for decreased slopes. Novikov[a-1] states that Fadeenko[a-13] presents a detailed survey of existing spall criteria. He describes a criterion based on the energy: the elastic energy in the tensile pulse has to be equal to the work required in separating the material (rupture or spall energy). Hence, a higher stress acting for a shorter time would be equivalent to a lower stress acting for a longer time. He says that Ivanov and Mineev[a-16] present rupture energies for various steels. The energetic spall criterion leads to an equation of the type:

$$\frac{\sigma_{cr}^3}{(\Delta\sigma/\Delta x)} = 6\,\rho_0\,C_0^2\,\gamma$$

where ρ_0 and C_0 are the initial density and longitudinal elastic wave velocity for the material, σ_{cr} the critical spalling stress, and $(\Delta\sigma/\Delta x)$ is the slope of the release portion of the pulse. Novikov[a-1] obtains the rupture energy γ from the slope of Fig. a-1. A similar approach could be used for square pulses.

An example of a more rigorous approach to spalling is the work by Romanchenko and Stepanov[a-19]. They used a compressed air gun (which assured planarity and parallelism of impact), recorded the stresses at the back surface of the targets by dielectric transducers, and applied the method of characteristics in the analysis of the stress pulses through the target, projectile, and back-up plate. The threshold spalling stress was determined by the observation of recovered specimens at a magnification of 100 × . They correlate the critical spalling stress with the tensile strains for aluminium, copper, and steel. In line with this rigorous work, Akhmadeev and Nigmatulin[a-20] describe numerical modeling of spalling incorporating shock-induced phase transformations which split the waves.

Golubev *et al.*[a-18] describe a number of industry experiments directed at establishing the temperature dependence of the spall strength. They used explosively-driven flyer plates

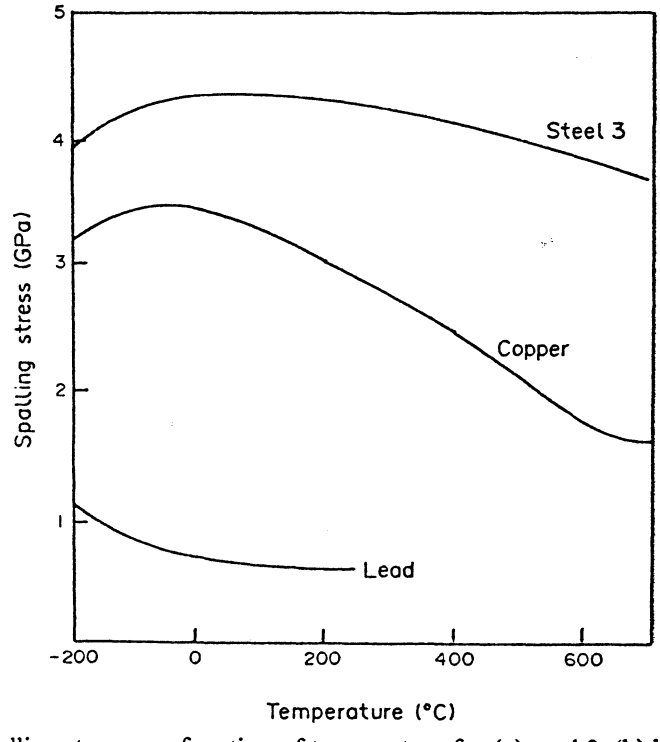

FIG. a-2. Critical spalling stress as a function of temperature for (a) steel 3; (b) lead; (c) copper. (From S. A. Novikov, *J. Appl. Mech. Tech. Phys.* 22 (1981) 385, Fig. 3.)

(aluminum alloy, 4 mm thick) and determined the stress required for observable (under the naked eye) spalling for aluminium alloys, steel, titanium, copper, nickel, and lead. Figure a-2 shows some of their results, as reported by Novikov[a-1]. The experimental techniques are somewhat crude but the results are significant. Substantial differences in spall strength are produced by varying the temperature. For steel there is an increase in spalling strength from −200°C to room temperature; the same trend is observed in copper. One could not predict this response from the quasi-static properties of these metals. The increased spall strength as the temperature is increased for steel, in the −200→0°C interval, can be explained by the change in fracture morphology from brittle to ductile. Novikov[a-1] also reports results for a steel in which the martensite produced by shock compression has a noticeable effect in the spall strength. Hence, he concludes that microstructural parameters are highly important. He points out, correctly, that simple computational models cannot incorporate the complexities and unpredictability of material response.

a.2 *Lawrence Livermore Work*

In 1977, Cochran and Banner[a-21] reported the results of an investigation into uranium. Using a gas gun, they systematically varied the stress and stress duration, keeping constant (at 0.5) the ratio between projectile and target thickness; this assured that the maximum tensile stress occurred in the middle of the target. Their results are shown in Fig. a-3. The flyer plate thicknesses are indicated in the plot. As the flyer plate thickness increases, the amount of damage increases at a constant stress level (determined by the flyer plate velocity). Conversely, at a constant flyer thickness the damage increases, for increasing stresses. These results corroborate other investigations that established that both stress and stress duration are important. The damage parameter given in the ordinate axis was not obtained from direct measurement of void densities, but indirectly, from free-surface velocity measurements. Cochran and Banner[a-21] used, instead, the peak formed in the free surface of the target when

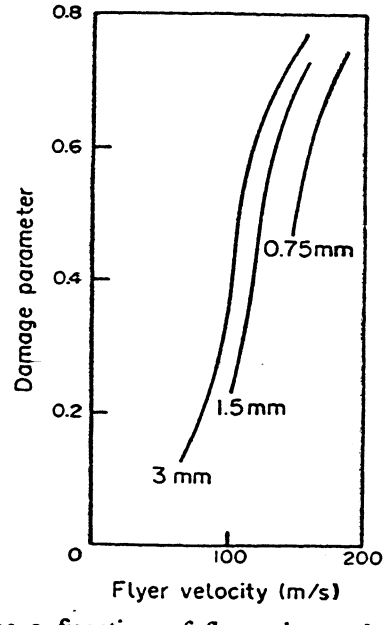

FIG. a-3. Damage parameter as a function of flyer plate velocity for three different flyer plate thicknesses in uranium. (From S. Cochran and D. Banner, *J. Appl. Phys.*, **48** (1977) 2719.)

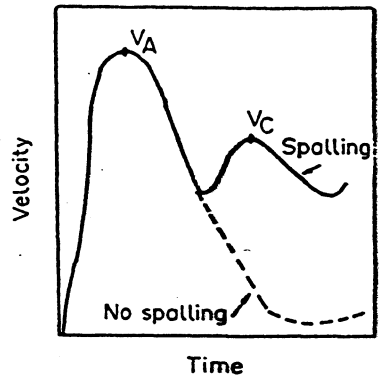

FIG. a-4. Free-surface velocity for spalling and no spalling; v_C/v_A defines the damage parameter.

a spall is formed. This effect is shown in Fig. 13(a). When a spall is formed the velocity at the free surface does not return to zero. Cochran and Banner[a-21] found that the ratio between the free-surface velocities of the spall and compression pulse peaks provided a good correlation with void densities at the spall plane. Figure a-4 shows a schematic diagram of the velocity trace; the damage parameter is v_C/v_A. This technique, if reliable, greatly simplifies the determination of spall damage, because tedious microflaw counting would be eliminated.

Cochran and Banner[a-21] developed a theoretical model and incorporated it into a one-dimensional finite difference hydrodynamic code (KO) developed by Wilkins. They incorporated the Bauschinger effect into the model; the Bauschinger effect is the strength differential that a specimen exhibits when it is stressed plastically in tension and then in compression (or *vice versa*); the strength upon reversal of the stress may be lower. They also considered a threshold stress Σ, below which no spalling occurs. To a certain extent, Σ

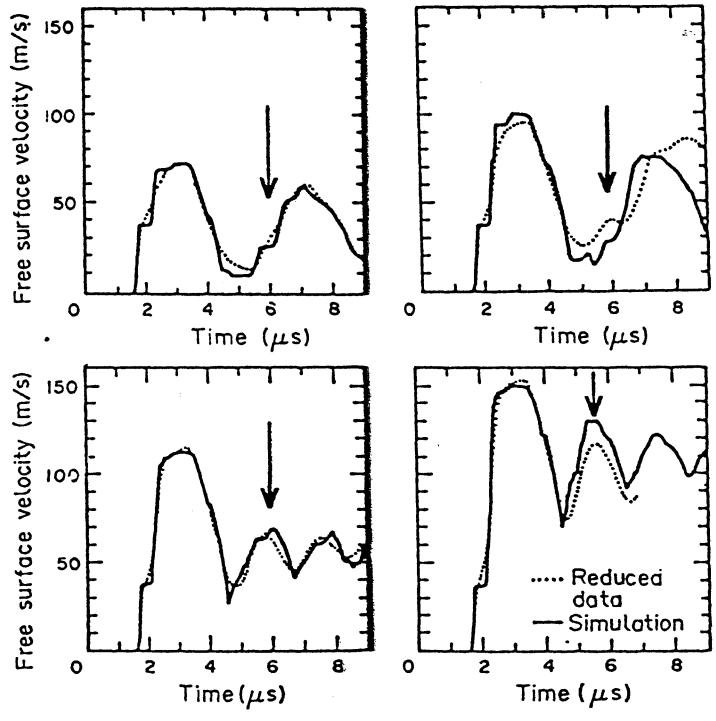

FIG. a-5. Free surface velocity versus time as a function of increasing impact velocity. Arrows indicate position of spall signal, which becomes stronger as impact (and free surface) velocity increases. (From S. Cochran and D. Banner, *J. Appl. Phys.*, 48 (1977) 2729, Fig. 10.)

similar to the stress σ_{go} in the SRI codes. They define a damage parameter $D(x, t)$ which is a function of both position and time. However, it is taken as the volume of microcracks per unit area (and not per unit volume, as in the other theories). Hence the parameter D has units of length. This procedure is justified by Cochran and Banner but is not very clear to us. Total spalling is obtained when D reaches a critical level D_0. By varying D_0 and Σ, Cochran and Banner try to match the experimentally observed free-surface velocity traces to the computed ones. Figure a-5 shows a sequence of observed and calculated traces at increasing impact velocities for uranium (flyer plate thickness: 3 mm; target thickness: 6 mm). As the surface velocity increases, the spall peak becomes more and more evident; it occurs at $\sim 6\,\mu$s and is marked by arrows. This fit was obtained with values of

$$\Sigma = 2.4\ \text{GPa}$$
$$D_0 = 55\ \mu\text{m}$$

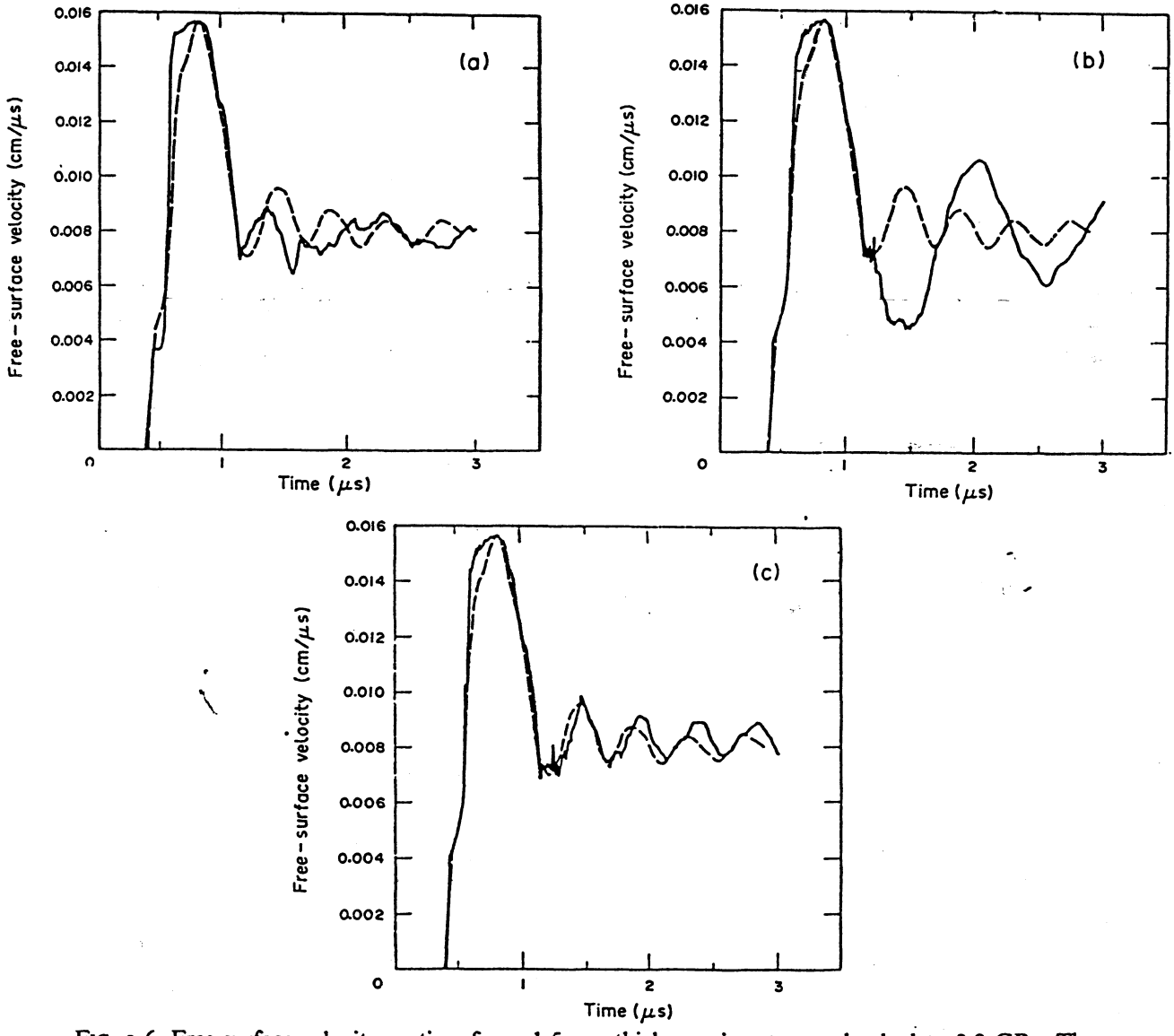

FIG. a-6. Free-surface velocity vs time for a 1.5-mm-thick uranium target shocked to 3.9 GPa. The broken line is the data, and the solid line is the calculation (a) without and (b) with the strain-rate model. The calculation in (c) is with the strain-rate model, but the spall parameters Σ and D_0 have been changed to 2.6 GPa and 4 μm, respectively. (From D. J. Steinberg and R. W. Sharp, Jr., *J. Appl. Phys.*, **52** (1981) 5072, Fig. 13.)

Steinberg and Sharp[a-23] in 1981 extended Cochran and Banner's[a-21] model by incorporating into it a rate dependence. This rate dependence can be simply explained in the following manner. The instantaneous value of the stress deviator is allowed to exceed the equilibrium yield stress. Hence, the instantaneous stress is allowed to exceed the spall strength Σ. As the time is increased, this maximum allowable stress decreases with a time constant τ. In essence, this corresponds to the incorporation of a viscous response of the material. Steinberg, Cochran and Guinan[a-22] described this strain-rate dependency in greater detail elsewhere. Steinberg and Sharp[a-23] incorporated this concept into the model and applied it to a number of situations, obtaining an improved correlation between observed and calculated free-surface velocity traces. Figure a-6 shows the traces for a 1.5 mm uranium target (flyer plate thickness half the target thickness). The incorporation of the strain-rate effect improves the correlation but requires the change in the adjustable parameters Σ and D_0. They were changed from 2.4 to 2.66 Pa, and 55 to 4 μm, respectively.

The work of Cochran and Banner[a-21] and Steinberg and Sharp[a-23] bypasses the necessity to look at spalling as a process of nucleation, growth, and coalescence of microflaws. However, implicit in the model are equivalent concepts, not very well physically justified. The nucleation is not considered, because large numbers of flaws are assumed to pre-exist. The growth is not incorporated, but is implicit in the visco-platic behavior during distention. The coalescence is established by the arbitrary parameter D_0, which sets the microflaw size which corresponds to the loss of the tensile stress-bearing ability of the material. The threshold stress for the growth of microflaws (which pre-exist) is Σ.

Addendum References

a-1 S. A. NOVIKOV, *J. Appl. Mech. Tech. Phys.* (translated from Russian), **22**, (1981) 385.
a-2 V. V. ADUSHKIN and A. P. SUKHOTIN, *Prikl. Mekh. Tekh. Fiz.*, No. 4 (1961).
a-3 F. F. VITMAN, M. I. IVANOV and B. S. IOFFE, *Fiz. Met. Metalloved.*, **18**, No. 5 (1964).
a-4 Y. U. TARASOV, *Dokl. Akad. Nauk. SSSR*, **165**, No. 2 (1965).
a-5 L. V. ALTSHULER, S. A. NOVIKOV and I. I. DIVNOV, *Dokl. Akad. Nauk. SSSR*, **166**, No. 1 (1966).
a-6 S. A. NOVIKOV, I. I. DIVNOV and A. G. IVANOV, *Fiz. Met. Metalloved.*, **21**, No. 4 (1966).
a-7 Y. M. PRIVALOV, V. R. SOLONENKO and B. E. TARASOV, *Fiz. Goreniya Vzryva*, No. 2 (1967).
a-8 S. A. NOVIKOV and L. M. SINITSYANA, *Fiz. Met. Metalloved.*, **28**, No. 6 (1969).
a-9 N. A. ZLATIN, S. M. MOCHALOV, G. S. PUGACHEV and A. M. BRAGOV, *Fiz. Tverd. Tela*, **16**, No. 6 (1974).
a-10 N. A. ZLATIN, and B. S. IOFFE, *Zh. Tekh. Fiz.* **42**, No. 8, (1972).
a-11 B. A. TARASOV, *Zh. Prikl. Mekh. Tekh. Fiz.*, No. 6 (1973).
a-12 N. A. ZLATIN, G. S. PUGACHEV, S. M. MOCHALOV, and A. M. BRAGOV, *Fiz. Tverd. Tela*, **17**, No. 9 (1975).
a-13 Y. I. FADEENKO, "*Time Rupture Criteria in Solid State Dynamics*", Institute of Hydrodynamics, Siberian Branch of the USSR Academy of Sciences, Novosibirsk (1977).
a-14 A. P. RYBAKOV, *Zh. Prikl. Mekh. Tekh. Fiz.*, No. 1 (1977).
a-15 V. I. ROMANCHENKO and G. V. STEPANOV, *Probl. Prochn.* No. 3 (1978).
a-16 A. G. IVANOV and V. N. MINEEV, *Fiz. Goreniya Vzryva*, No. 5 (1979).
a-17 Y. V. BATKOV, S. A. NOVIKOV, *et al.*, *Zh. Prikl. Mekh. Tekh. Fiz.*, No. 3, (1979).
a-18 V. K. GOLUBEV, S. A. NOVIKOV, V. A. SINITSYN and Y. S. SOBOLEV, *J. Appl. Mech. Tech. Phys.*, (translated from Russian), **21** (1981) 551.
a-19 V. I. ROMANCHENKO and V. G. STEPANOV, *J. Appl. Mech. Tech. Phys.* (translated from Russian), **21** (1981) 551.
a-20 N. K. AKHMADEEV and R. I. NIGMATULIN, *J. Appl. Mech. Tech. Phys.* (translated from Russian) **22** (1981) 394.
a-21 S. COCHRAN and D. BANNER, *J. Appl. Phys.* **48** (1977) 2729.
a-22 D. J. STEINBERG, S. G. COCHRAN and M. W. GUINAN, *J. Appl. Phys.*, **51** (1982) 1498.
a-22 D. J. STEINBERG and R. W. SHARP, JR., *J. Appl. Phys.*, **52**, (1981) 5072.